Title
NMR Spectroscopy of Membrane Proteins in Phospholipid Bilayers

Author
Long, Zheng

Publication Date
2019

UNIVERSITY OF CALIFORNIA SAN DIEGO

NMR Spectroscopy of Membrane Proteins in Phospholipid Bilayers

A dissertation submitted in partial satisfaction of the requirements for the degree
Doctor of Philosophy

in

Chemistry

by

Zheng Long

Committee in charge:

Professor Stanley Opella, Chair
Professor Joshua Figueroa
Professor Patricia Jennings
Professor Judy Kim
Professor Roger Sunahara

2019

The Dissertation of Zheng Long is approved, and it is acceptable in quality and form for publication on microfilm and electronically:

Chair

University of California San Diego

2019

DEDICATION

This dissertation is dedicated to my family and friends who have always been supportive for my career. Especially to my mother, father, and my wife who have provided me with unconditional support. It is also dedicated to my grandparents who have always been my fans.

TABLE OF CONTENTS

LIST OF ABBREVIATIONS

BSA	Bovine Serum Albumin
CCDC	Cambridge Crystallographic Data Centre
CP	Cross Polarization
CSA	Chemical Shift Anisotropy
CW	Continuous Wave
CXCL5	CXC Chemokine 5
CXCR1	CXC Chemokine Receptor 1
CXCR2	CXC Chemokine Receptor 2
DHPC	1,2-dihexanoy-sn-glycero-3-phosphocholine
DMPC	1,2-dimyristoyl-sn-glycero-3-phosphocholine
DMPG	1,2-dimyristoyl-sn-glycero-3-phosphorylglycerol
DMSO-D6	deuterated dimethyl sulfoxide
DPC	Dodecyl Phosphocholine
EDTA	Ethylenediamine tetraacetic acid
FPLC	Fast Protein Liquid Chromatography
FID	Free Induction Decay
GPCR	G Protein-Coupled Receptor
GST	Glutathione S-transferase
HEPES	4-(2-hydroxyethyl)-1-piperazineethanesulfonic acid
HETCOR	Heteronuclear Correlation
HPLC	High Pressure Liquid Chromatography

HPC	Hexadecyl Phosphocholine
HSQC	Heteronuclear Single Quantum Coherence
IL-8	Interleukin-8
INEPT	Insensitive Nuclei Enhanced by Polarization Transfer
IPTG	Isopropyl β-thiogalactoside
kD	Kilo Dalton
LB	Luria-Bertani
MAS	Magic Angle Spinning
MMHH	Mismatched Hartmann-Hahn
MOIST	Mismatch Optimized IS Transfer
MSP	Membrane Scaffold Protein
NI-NTA	Nickel Nitrilotriacetic Acid
NMR	Nuclear Magnetic Resonance
NTER	N-terminal Domain
PAGE	Polyacrylaminde Gel Electrophoresis
PBS	Phosphate Buffered Saline
PDSD	Proton Driven Spin Diffusion
PISEMA	Polarization Inversion Spin Exchange at the Magic Angle
PISEMO	Polarization Inversion Spin Exchange Modulated Observation
PMSF	Phenylmethanesulfonylfluoride
RP-HPLC	Reverse phase HPLC
SAMMY	Sandwich-Based Separated Local Field Spectroscopy
SDS	Sodium Dodecyl Sulfate

SLF	Separated Local Field
SMA	Styrene-Maleic Acid
SMALP	Styrene Maleic Acid Lipid Particle
SPINAL	Small Phase Incremental Alternation
TCEP	Tris(2-carboxyethyl)phosphine
TFA	Trifluoroacetic acid
TFE	2,2,2-Trifluoroethanol
TRIS-HCL	Tris(hydroxymethyl)aminomethane hydrochloride

LIST OF FIGURES

LIST OF TABLES

ACKNOWLEDGEMENTS

I want to thank my dissertation advisor Professor Stanley Opella for giving me the opportunity to participate in exciting research. This dissertation is founded on his tremendous support and guidance. He also entrusted me with projects of great challenges, and provided me with great patience when things do not work out immediately. I would also like to thank my committee members Professor Patricia Jennings, Professor Roger Sunahara, Professor Judy Kim, and Professor Joshua Figueroa for their support and guidance. I would also like to acknowledge former committee Professor Roy Wollman for his support as well.

I would like to thank my current lab members Dr. Sang ho Park and Dr. Anna de Angelis, for their suggestions, guidance, and help over the years. I would like to thank Emily Wu for her help in the Mer project. I would like to thank past Opella members for being an important part of my research life during my time here. I have learned a lot from all of them. To my past lab members, especially Dr. Albert Wu, Dr. Ratan Rai, Dr. Jasmina Radoicic, and Dr. Sabrina Berkamp, I am thankful for their endless efforts to help and train me over the years. I am also thankful for being able to have worked with Dr. Chris Grant, Dr. Bibhuti Das, Professor Eugene Lin, Dr. Hua Zhang, Dr. Lindsay Dawson, Dr. Ana Pavlova, Dr. Andreea Balaceanu, Megan Chu, and Vivian Wang, Dr. Luis Basso, Dr. Cody Can, and Youjeong Na. I am thankful for them for sharing their research, passions, and aspirations with me. I am thankful for my undergraduate trainees Jay and Iris for their assistance in the wet lab.

Also many thanks to Dr. Xuemei Huang and Dr. Anthony Mrse, for their help and guidance. I would also like to thank Dr. Collin Lipper and Dr. Samit Dutta for helpful discussions, and Dr. Jingfa Ying from NIH for his help and guidance. I would like to thank Professor Lalit Deshmukh for his support and guidance. I would also like to thank Dr. Chen Zhang from the Gerwick lab for discussions of NMR topics over the years. I would also like to thank Dr. Sergey Maltsev for many discussions of solid-state NMR during my time in Texas.

I want to thank Professor Francesca Marassi and her lab for the great discussions we had. I also want to thank the Jennings lab and the Deshmukh lab for being great lab-neighbors, and the Debelouchina lab for being our great solid-state NMR neighbor. I want to thank Professor Allen T Phillips (ATP) from the Pennsylvania State University, who initiated me into the world of scientific research, for his continued support and help since my undergraduate times. I also want to thank Professor Andreas Holzenburg of University of Texas and Professor Tatyana Igumenova of Texas A&M University for their help and guidance for my time at Texas A&M University. I want to thank Professor Hai Rao of University of Texas Health Science Center San Antonio, and Dr. Xiaochuan Feng of Tufts Cumming School of Veterinary Medicine for their scientific training when I was an undergraduate student.

Chapter 2, in full, is a reprint of the material as it appears in Long, Z, Park, SH, Opella SJ, (2019), Effects of deuteration on solid-state NMR spectra of single peptide crystals and oriented protein samples, *J. Magn. Res. 309:106613*. The dissertation author is the primary researcher and author on the paper.

Chapter 3, in full, is a reprint of the material as it appears Long, Z, Opella SJ, (to be submitted), ^{1}H detection with water suppression of ^{1}H-^{15}N heteronuclear dipolar oscillations in single crystal peptide and oriented protein samples, (2019). The dissertation author is the primary researcher and author on the manuscript.

Chapter 5, in full, is a reprint of the material as it appears Long, Z, Opella SJ, (to be submitted), Studies of Full Length and Truncated Chemokine Receptors Reveal mechanism of Chemokine Signaling Bias for CXCR1 and CXCR2, (2019). The dissertation author is the primary researcher and author on the manuscript.

VITA

2011 Bachelors of Science, Biochemistry and Molecular Biology, the Pennsylvania State University, University Park

2011 Bachelors of Science, Chemistry, the Pennsylvania State University, University Park

2013 Masters of Science, Biochemistry and Biophysics, Texas A&M University

2019 Doctor of Philosophy, Chemistry, University of California San Diego

PUBLICATIONS

Long, Z, Opella SJ, (to be submitted), Studies of Full Length and Truncated Chemokine Receptors Reveal mechanism of Chemokine Signaling Bias for CXCR1 and CXCR2, (2019).

Long, Z, Opella SJ, (to be submitted), ^{1}H detection with water suppression of ^{1}H-^{15}N heteronuclear dipolar oscillations in single crystal peptide and oriented protein samples, (2019).

Long, Z, Park, SH, Opella SJ, (2019), Effects of deuteration on solid-state NMR spectra of single peptide crystals and oriented protein samples, *J. Magn. Res. 309:106613*.

Morales, KA, Yang, Y, Long, Z, Li, P, Taylor, AB, Hart, PJ, Igumenova, TI (2013) Cd^{2+} as a Ca^{2+} surrogate in protein-membrane interactions: isostructural but not isofunctional. *J. Am. Chem. Soc.* 135:12980-3.

Johnson, CB, Long, Z, Luo, Z, Shaik, RS, Sung, MW, Vitha, S, Holzenburg, A., (2015) In situ structure of FtsZ mini-rings in Arabidopsis chloroplasts. *Adv. Struct. Chem. Imag.* 1:12.

ABSTRACT OF THE DISSERTATION

NMR Spectroscopy of Membrane Proteins in Phospholipid Bilayers

By

Zheng Long

Doctor of Philosophy in Chemistry

University of California San Diego, 2019
Professor Stanley Opella, Chair

Solid-state nuclear magnetic resonance (NMR) spectroscopy is a powerful method for the study of membrane proteins under native environments. G protein-coupled receptors (GPCRs) are highly challenging integral membrane proteins that are often hard to study using the available biophysical techniques. Limited information about their structures and dynamics has been elucidated with x-ray crystallography as well as various biochemical techniques, such as Föster resonance energy transfer (FRET), and mutation studies. Obtaining site resolved NMR spectra for GPCRs can help to better understand their structures and behaviors. Here CXC-chemokine receptor 2 (CXCR2) is studied with various NMR tools, and the functional relevance of the obtained protein is verified with ligand binding assays as well as NMR. A comparison of CXCR2 interaction with two of its ligands: interleukin 8 and CXCL5 is also presented. At the same time, methods such as protein perdeuteration, and ^{1}H detection were developed for the study of complex membrane proteins using the oriented-sample solid-state NMR technique. NMR developments are also made on the MerFTC chimeric protein, to help experiments for the more complex CXCR2. Combining various NMR techniques, optimized NMR spectra are presented, providing insights into the structure and function of the CXCR2 protein.

Chapter 1: Introduction to protein NMR

1.1 NMR spectroscopy

Nuclear magnetic resonance spectroscopy or NMR is a widely used technique for the study of atoms and molecules. The method can be used to elucidate structure and dynamics of materials ranging from molecular gas to large biomolecular assemblies. NMR takes advantage of the magnetic properties of the atomic nuclei and uses on resonance radiofrequency pulses to effect changes in their nuclear spin-states. Under the influence of an external magnetic field, spin-states become energetically un-equivalent. Because of their unique gyromagnetic ratios, each nuclear species has its unique energy difference and thus has a unique transition frequency. The powerful spectroscopy can also be used to distinguish different nuclei within the same atom species, because nuclei found in molecules often situate in very different atomic surroundings. Differences in electronic environments produce different magnetic shielding effects on the nuclei, resulting in small changes in their spin-state energy levels. These shifts or shielding effects due to surrounding electrons are thus named chemical shift interactions or chemical shielding interactions. Chemical shielding interactions in rigid solids are anisotropic and can be expressed mathematically as second rank tensors in Cartesian coordinates:

$$\sigma = \begin{bmatrix} \sigma_{XX} & \sigma_{XY} & \sigma_{XZ} \\ \sigma_{YX} & \sigma_{YY} & \sigma_{YZ} \\ \sigma_{ZX} & \sigma_{ZY} & \sigma_{ZZ} \end{bmatrix}$$

The tensor matrix can be diagonalized to have only three principle components occupying the diagonal positions. The three principle components are named δ_{11}, δ_{22}, and δ_{33}. When molecules rapidly rotate, the three principle components averages to their average value producing what is called the isotropic chemical shift or δ_{iso}. Resonances in NMR spectra of a powder pattern would have easily identifiable principle components as shown in Figure 1.1.

$$\delta_{iso} = 1/3\ (\delta_{11} + \delta_{22} + \delta_{33})$$

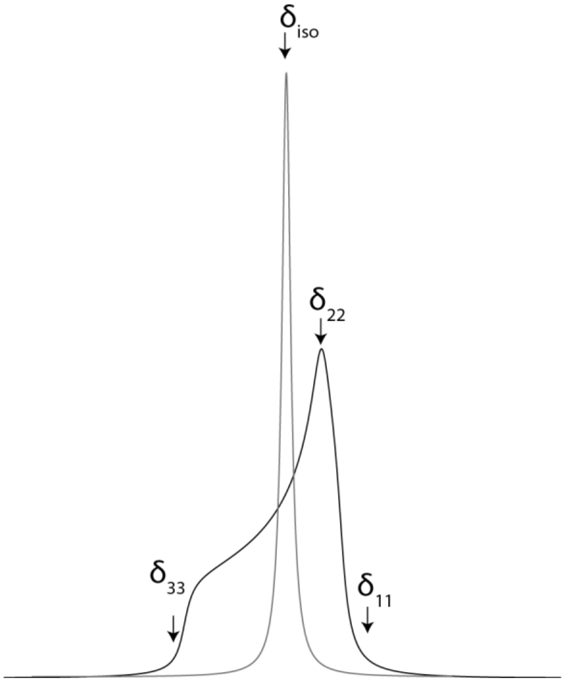

Figure 1.1 Illustration of a single resonance powder pattern showing the three principle components of the CSA tensor δ_{11} , δ_{22} , δ_{33} in the powder pattern (black line), and the isotropic value δ_{iso} in the isotropic averaged pattern (grey line). The assignments of the three principle axes follow a convention of $\delta_{33} > \delta_{22} > \delta_{11}$ consistent with previous publications in the Opella group.

Besides chemical shift interactions, an atomic nucleus experiences additional spin interactions with other nuclei directly (dipolar coupling), with other nuclei through chemical bond (J-coupling), or/and with electric field gradient (quadrupole coupling). Dipolar coupling or dipole-dipole interaction is the direct interactions between atomic nuclei, J-coupling is the indirect coupling of atomic nuclei through chemical bonds, and quadrupole coupling originates from the nuclear spin interaction with the electric field generated by the non-symmetrical electron distributions from spin>1/2 nuclei. These interactions splits and/or broadens the NMR spectra but each could also be dealt with using different types of spectroscopic methods.

When NMR signal is acquired, a free induction decay (FID) is recorded. In a single pulse NMR experiment, an FID can be collected following a "90 degree" excitation pulse. The 90 degree pulse resonates at the frequency of the measured nucleus which induces maximum transitions between nuclear spin states. The induced non-equilibrium states then relax producing the FID until equilibrium is again achieved. In Figure 1.2, spectroscopic techniques such as the insensitive nucleus enhanced by polarization transfer (INEPT) and cross-polarization (CP) experiments are shown. These experiments represent the two major classes of experiments that are used in later chapters. The use of the two experiments depends on sample properties: CP experiments takes advantage of the heteronuclear dipolar interactions to transfer magnetization through Hartmann Hahn match. The Hartmann Hahn match uses radiofrequency irradiation that induces matching energy differences between spin states across two difference species of nuclei, causing polarization transfer from one type of nucleus to another. The INEPT experiment on the other hand relies on the J-coupled nuclear spin pairs for polarization transfer by the 180 degree inversion pulses indicated in Figure 1.2 B.

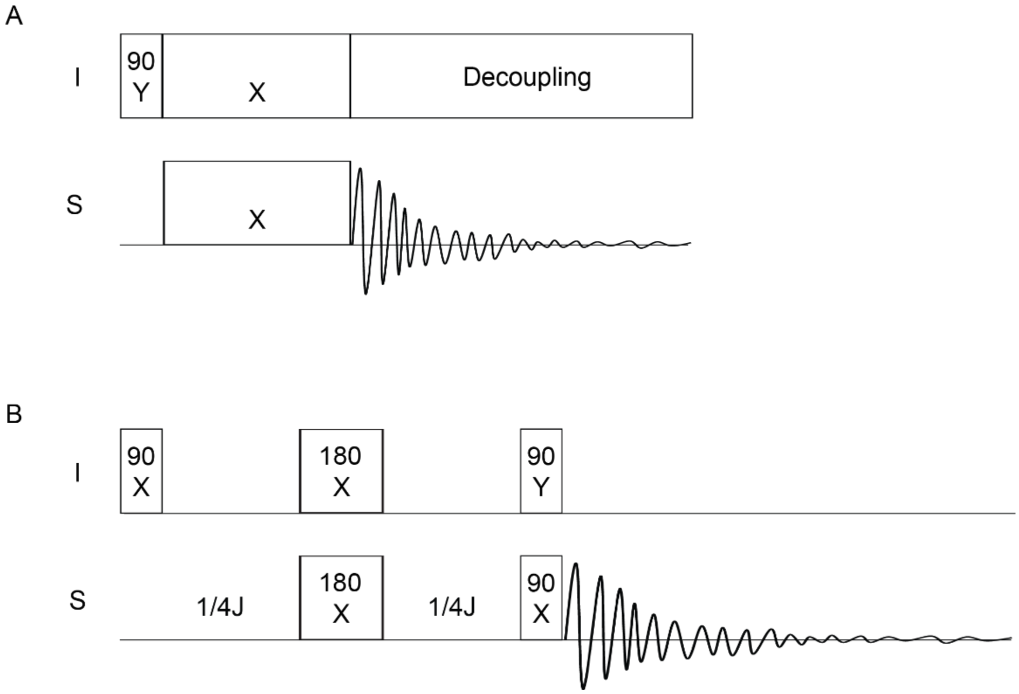

Figure 1.2 Basic experiments for solid-state and solution NMR. (A) Cross polarization (CP) experiment from abundant spin I to spin S. (B) Insensitive nucleus enhanced by polarization transfer (INEPT) experiment.

1.2 NMR of mobile and rigid molecules

In solution state NMR samples, molecular motions are unrestricted, molecules are free to rotate, and strong nuclear dipole-dipole interactions are averaged allowing the measurements of chemical shifts. Also due to these fast motions, the anisotropic chemical shift interactions are averaged to the isotropic chemical shift. The isotropic chemical shift often just referred to as the 'chemical shift' in solution NMR studies.

When molecular motions are slow or restricted due to the size or shape of the molecules. Their movements cannot completely average the effects of nuclear spin interactions in all directions, resulting in a spin relaxation that couples with other nuclei in the surroundings. These couplings reduce the relaxation time and in turns result in broader resonance line-widths in the Fourier transformed NMR spectra. The restricted slow motions also reduce the spread of the angular dependence of the anisotropic chemical shifts creating residual chemical shift anisotropy.

When there is a lack of motion for the observed nuclei. Strong spin coupling networks can often result in extremely short relaxation times. With rigid orientations, chemical shift anisotropy (CSA) is then in its full spread. In a sample which contains multiple observable atomic nuclei, CSA often causes overlaps between different acquired signals making spectra interpretation difficult. To deal with the resolution problem, different methods has been devised, they will be discussed in section 1.6.

1.3 NMR signals and sensitivity

Only selected nuclei are regularly used for NMR studies, and different nuclei have different signal sensitivities. This is because of different nuclear compositions and magnetic properties, commonly used nuclei for biological NMR are ^{1}H, ^{2}H, ^{13}C, ^{15}N, and ^{31}P. ^{1}H nucleus is abundant in nature as well as sensitive, it is frequently chosen for detection. ^{31}P is also a sensitive and abundant nucleus in biological samples. For example, ^{31}P can be found in phospholipids, DNA and phosphorylated proteins. Compared to ^{1}H and ^{31}P, ^{13}C and ^{15}N nuclei are found only in low natural abundance levels. But nitrogen and carbon atoms are abundant in proteins, as a result, protein NMR samples often require isotope enrichments to replace the more abundant ^{14}N and ^{12}C with rarer ^{15}N and ^{13}C isotopes, so that signals from these crucial positions in the protein structure can be recorded and distance information can be extract for structure elucidation[13].

The sensitivity of a specific atomic nucleus in NMR experiment is related to their gyromagnetic ratio (γ). The γ values of commonly observed atomic nucleus in biological sample NMR sepctroscopy are listed in Table 1.1. Comparing absolute values of the gyromagnetic ratios, it can be seen that the sensitivity of the ^{1}H nuclei is much higher. This is the rationale behind experiments developed in chapter 3 for solid-state NMR.

Table 1.1 Gyromagnetic ratio of nuclei common to biological NMR [1].

Nucleus	Gyromagnetic ratio (MHz/T)
^{1}H	42.58
^{13}C	10.71
^{15}N	-4.32
^{31}P	17.24

1.4 NMR of single crystals, micro-crystals and liquid crystals

Single crystals contain orderly packed molecules that are found as uniform repeats across a single crystal lattice, depending on the crystal symmetry group, one or multiple sets or molecular orientations can be found across the crystal lattice. Compared to amorphous powder which has molecules randomly oriented in all directions, using a single crystal sample allows one to avoid the orientation spread in the sample allowing measurements of single sets of chemical shifts whose values are orientation dependent. In chapter 2 and 3, the use of N-acetyl leucine single crystal serves as a rudimentary model system for proteins. However, single crystals of proteins can rarely grow to enough size for conventional NMR spectroscopy. So often times, microcrystalline samples are instead pursued. Microcrystalline samples contain many crystal lattices at random orientations. The crystal lattice constrains the conformation of proteins allowing the observation of a single conformation, however, the random orientations of these samples require the use of the magic angle spinning (MAS) technique (explained in section 1.6) to obtain simplified spectra for structural analysis. Compared to soluble proteins that can be studied in their microcrystalline states, membrane proteins are often studied in proteoliposomes for MAS solid-state NMR which is completely amorphous in protein arrangements. Microcrystalline and amorphous samples represents another class of samples for NMR experiments. The MAS technique was used to evaluate the folding state of a membrane protein in chapter 5.

Another type of sample for NMR belongs to a class of materials called liquid crystals. Certain liquid crystal samples has magnetic properties allowing them to align under the influence of the external magnetic field. The method of oriented sample NMR takes advantage of the alignment of liquid crystalline materials, where the external magnetic field can induce order in the liquid and produce sharp resonance lines similar to the case for the single crystal samples. But unlike single crystal samples, a liquid crystal sample is a dynamic system which has phase transitions due to changes in temperature or concentration. The alignment of molecules in the magnetic field collapses the CSA into a single chemical shift value and the chemical shift value as a result is orientation dependent. The examples for liquid crystal that are used in later chapters are the filamentous phage Pf1, DMPC/DHPC bicelles, macrodiscs. NMR spectra for these samples are found throughout all later chapters.

1.5 NMR in structural biology

Protein NMR has been an important branch of structural biology, in particular solution state NMR, has been used widely to elucidate protein structures [2]. As of the time when this dissertation is written, 12670 solution structures have been deposited in protein data bank (rcsb.org/pdb). Compared to the solution NMR technique, only 105 structures were found obtained with the solid-state NMR method. Structural elucidation with the two NMR methods are governed by very different sets of principles. In solid state NMR, the measurements of dipolar couplings provides inter-nuclear distance and angle information, while in solution NMR the measurement of nuclear Overhauser effect (NOE) provides distance restraints, and the measurement of residual dipolar coupling (RDC) can provide angle restraints.

1.6 Solid-state NMR, magic angle, and magic angle spinning

Solid-state NMR is an emerging NMR method in structural biology, with only 105 structures deposited in the protein data bank, it has not gained the same level of popularity compared to solution NMR. Aforementioned, the reason is that in solid-state, samples have restricted motional freedoms, which creates two problems: first of all, the presence of strong dipolar interactions among the abundant ^{1}H atomic nuclei split and broadens the resonances of interest. Secondly, chemical shift anisotropy causes overlaps in resonances. These two factors contribute to poor spectral resolution and sensitivity, making the solid-state NMR technique rather difficult to apply. Chemical shift anisotropy has been introduced in section 1.1 and it can be averaged to isotropic value under MAS, and it can also be simplified when sample can be aligned as mentioned in previous sections. Here a close examination of the dipole-dipole interactions between nuclei is given. The classical mechanics expression of nuclear dipolar interactions can be written as:

$$\omega = (\frac{-\mu_0}{4\pi})(\hbar\frac{\gamma_1 \cdot \gamma_2}{r^3}) \cdot \frac{1}{2}(3\cos^2\theta - 1)$$

Where ω is the magnitude of the dipolar coupling; μ_0 is the vacuum permeability constant, γ_1 and γ_2 are the gyromagnetic ratios of the two atomic nuclei; r is the distance between the two nuclei, and θ is the angle between the external magnetic field and their dipolar interaction axis. The definition of the "magic angle" comes from the term $3(\cos^2\theta -1)$, when it equals 0, θ is 54.7^o. As a result, at the exact magic angle, dipolar coupling terms are 0, which can be achieved by physical means, leading to the magic angle spinning methods. Spectroscopic methods has also been developed to decouple the nuclei that are dipolar coupled. Heteronuclear decoupling is a technique that deals with the decoupling of different spin species, reducing the effects of target spin species on the spin of interest. The heteronuclear decoupling is often achieved with a high power radiofrequency irradiation at the target nuclear frequency which induces frequent transitions between its spin states. This renders the nucleus of interest free of the effects of the target heteronuclear spin species.

Two classes of methods exists to deal with the homonuclear dipolar couplings: average Hamiltonian method [3] and Lee-Goldberg irradiation [4]. The two methods deal with dipolar coupling differently. The average Hamiltonian methods averages the spin Hamiltonian terms resulting in the attenuation of the homonuclear dipolar couplings. The Lee-Goldberg irradiation on the other hand induces the magic angle condition in spin space, using high power off-resonance radio frequency pulses. Developments of these techniques has enabled high resolution NMR spectra in the solid-state. Detailed discussions of topics related to decoupling can be found in Chapter 2, and 3.

1.7 NMR of integral membrane proteins

Early NMR studies of biological membrane was carried out in detergent extracts of cell membranes [5], or vesicles prepared with native cellular membranes [6]. However, due to the limitation of the NMR techniques at the time, low resolution spectra could only provide evidence for the presence of membrane proteins. To obtain valuable structural information of the membrane proteins, especially integral membrane proteins, highly purified and isotope enriched proteins are required. Decades after the initial endeavors, NMR experiments on membrane bound proteins started to gain importance in structural biology. In recent years, due to the progress in new membrane technologies, the study of integral membrane proteins using NMR has seen rapid advancement. It was shown that with the help of the technique of selective labeling, it was possible to obtain structure and dynamic information for large membrane proteins such as bacteriorhodopsins and G protein-coupled receptors (GPCRs) [7-12]. These techniques are highly complex and are selective in terms of sample conditions and protein stability. Thus to continue to develop and implement novel NMR methods remains highly important. Unrestrained by the requirements of fast molecular tumbling, solid-state NMR techniques can be applied to study large membrane proteins. Larger and more complex proteins such as the GPCRs made them difficult for many biophysical techniques. For example, the study of CXCR1 a human GPCR expressed in *E.coli* and reconstituted into detergent free liposomes was demonstrated using solid-state NMR methods [8]. Another example of NMR study of GPCR using detergent free membrane system is the neurotensin receptor type 1 (NTR1) reconstituted into detergent free nanodiscs [13]. This study however, did not go as far as obtaining a structure of the receptor protein. Overall, examples of NMR structural studies of these large GPCR proteins in native lipid bilayer environments are scarce. Besides their size, GPCRs are difficult to study because they are highly dynamic, a more detailed discussion can be found in chapter 5. Also in chapter 5, NMR studies of a GPCR protein CXCR2 is presented.

The major obstacles in these membrane protein experiments are sample stability, experimental sensitivity, and spectral resolution. Membrane proteins can also be highly dynamic and can be prone to aggregation over time; and the larger a membrane protein is, the more of the same type of amino acids it contains. Although protein NMR experiments using the solid states spectroscopic techniques were shown to be unaffected by the size of the protein of interest, it was limited by the practical aspects of spectral analysis, i.e. the structural information obtained by NMR can only be used if the measured resonances can be assigned to the correct atoms.

1.8 NMR samples

Depending on the type of NMR spectroscopy used, NMR samples have different physical and magnetic properties. Since biological samples need to be studied in hydrated environments, water is the main component of the protein NMR samples. This has important consequences in how experiments are carried out. Compared to cryoEM and x-ray crystallography, NMR allows studying of protein structures at physiological temperatures. However, NMR is an inherently insensitive technique because of the small population differences between different spin-states and it requires milligrams of isotope enriched proteins to obtain enough signal to noise levels. With recent progress in techniques such as the hyperpolarization methods [14], requirements for sample quantities will no longer be the paradigm. The use of NMR spectroscopy for the studies of large membrane proteins has tremendous potentials, further developments of the technique carries great significance when new tools and techniques become available for future researchers.

1.9 Overview of later chapters

While NMR spectroscopy of membrane proteins is often complicated by many factors intrinsic to proteins or sample conditions in oriented sample solid-state NMR, many potential methods to improve the technique remain unexplored. Chapter 2 investigates the use of deuteration to improve the resolution of proteins, and chapter 3 explores the application of ^{1}H detection of aligned proteins. In chapter 4, the feasibilities of the study of a three-transmembrane helix protein is evaluated. And in chapter 5 visits the sample and NMR of a GPCR protein CXCR2. More developments are still needed to be made for structural studies of proteins like CXCR2 using the oriented solid-state NMR technique.

1.10 References

[1] M.A. Bernstein, K.F. King, X.J. Zhou, Handbook of MRI pulse sequences, in, Academic Press,, Amsterdam ; Boston, 2004.

[2] K. Wuthrich, NMR studies of structure and function of biological macromolecules (Nobel Lecture), Journal of Biomolecular Nmr, 27 (2003) 13-39.

[3] J.S. Waugh, L.M. Huber, U. Haeberlen, Approach to High-Resolution Nmr in Solids, Phys Rev Lett, 20 (1968) 180-+.

[4] W.I. Goldburg, M. Lee, Nuclear Magnetic Resonance Line Narrowing by a Rotating Rf Field, Phys Rev Lett, 11 (1963) 255-&.

[5] D. Chapman, V.P. Kamat, J. Degier, S.A. Penkett, Nuclear Magnetic Resonance Studies of Erythrocyte Membranes, J Mol Biol, 31 (1968) 101-&.

[6] D.G. Davis, G. Inesi, Proton Nuclear Magnetic Resonance Studies of Sarcoplasmic Reticulum Membranes - Correlation of Temperature-Dependent Ca2+ Efflux with a Reversible Structural Transition, Biochim Biophys Acta, 241 (1971) 1-&.

[7] M. Kamihira, T. Vosegaard, A.J. Mason, S.K. Straus, N.C. Nielsen, A. Watts, Structural and orientational constraints of bacteriorhodopsin in purple membranes determined by oriented-sample solid-state NMR spectroscopy, J Struct Biol, 149 (2005) 7-16.

[8] S.H. Park, B.B. Das, F. Casagrande, Y. Tian, H.J. Nothnagel, M. Chu, H. Kiefer, K. Maier, A.A. De Angelis, F.M. Marassi, S.J. Opella, Structure of the chemokine receptor CXCR1 in phospholipid bilayers, Nature, 491 (2012) 779-783.

[9] V. Ladizhansky, Applications of solid-state NMR to membrane proteins, Biochim Biophys Acta Proteins Proteom, 1865 (2017) 1577-1586.

[10] L. Susac, M.T. Eddy, T. Didenko, R.C. Stevens, K. Wuthrich, A2A adenosine receptor functional states characterized by (19)F-NMR, Proc Natl Acad Sci U S A, 115 (2018) 12733-12738.

[11] M.T. Eddy, M.Y. Lee, Z.G. Gao, K.L. White, T. Didenko, R. Horst, M. Audet, P. Stanczak, K.M. McClary, G.W. Han, K.A. Jacobson, R.C. Stevens, K. Wuthrich, Allosteric Coupling of Drug Binding and Intracellular Signaling in the A2A Adenosine Receptor, Cell, 172 (2018) 68-80 e12.

[12] T. Ueda, Y. Kofuku, J. Okude, S. Imai, Y. Shiraishi, I. Shimada, Function-related conformational dynamics of G protein-coupled receptors revealed by NMR, Biophys Rev, 11 (2019) 409-418.

[13] P. Egloff, M. Hillenbrand, C. Klenk, A. Batyuk, P. Heine, S. Balada, K.M. Schlinkmann, D.J. Scott, M. Schutz, A. Pluckthun, Structure of signaling-competent neurotensin receptor 1 obtained by directed evolution in Escherichia coli, Proc Natl Acad Sci U S A, 111 (2014) E655-662.

[14] L.T. Kuhn, Hyperpolarization methods in NMR spectroscopy, in: Topics in current chemistry,, Springer,, Berlin, 2013, pp. 1 online resource (vii, 304 pages).

Chapter 2 : Deuteration improves the resolution of solid-state NMR spectra of oriented protein samples

2.1 Introduction

Dilution of ^{1}H nuclei through perdeuteration of nearby carbon sites with retention of a limited number of ^{1}H nuclei on specific carbon or nitrogen sites is a frequently used technique in protein NMR spectroscopy. In samples for solution-state NMR [1, 2] and magic angle spinning solid-state NMR [3-5], substantial line narrowing results. Originally implemented to assist with resonance assignments and improve resolution, it is now most widely employed to narrow resonances through attenuation of strong ^{1}H-^{1}H homonuclear dipole-dipole interactions that affect relaxation in solution and line shapes in solid-state samples where local or global molecular motions are absent or insufficient to average out dipolar interactions.

In solid-state NMR, dilution of ^{1}H nuclei by deuteration of surrounding sites was first examined in nematic liquid crystals [6, 7] and ice [8]; in both cases, ^{2}H decoupling was required in order to obtain high resolution ^{1}H NMR spectra. In addition to chemical dilution by replacement of the bulk of ^{1}H by ^{2}H, homonuclear ^{1}H-^{1}H dipolar interactions can be attenuated through the application of spectroscopic techniques, such as Lee-Goldburg (LG) continuous “magic-angle” irradiation [9], frequency-switched Lee-Goldburg (FSLG) [10], multiple pulse sequences, such as WAHUHA [11] and “magic sandwiches” [12]. Importantly, suppression of homonuclear dipolar interaction terms in the Hamiltonian through isotopic dilution or radiofrequency irradiations allows other interactions, such as chemical shifts and heteronuclear dipolar couplings, to be measured. Heteronuclear dipolar couplings provide information about chemical structures through measurements of internuclear distances and the angles between internuclear vectors and the magnetic field in stationary single crystal and uniaxially oriented samples. The heteronuclear dipolar couplings can be measured with separated local field (SLF) experiments [13, 14]. Narrower line-widths and higher resolution are available through the implementation of FSLG [15] and magic-sandwich pulses [16, 17] that suppress homonuclear ^{1}H-^{1}H couplings.

Here we examine the role of perdeuteration in improving the measurement of heteronuclear dipolar couplings in peptides and proteins by utilizing the well-established model systems of single crystals of N-acetylated leucine (NAL) and the membrane-bound form of Pf1 coat protein in magnetically aligned phospholipid bilayers. The single amide site in each of the four NAL molecules in the crystal unit cell results in four signals with distinct ^{15}N chemical shift frequencies and ^{1}H-^{15}N heteronuclear dipolar coupling frequencies. Protein-containing bicelles align with their bilayer normals perpendicular to the direction of the magnetic field [18, 19]. Since the protein molecules undergo rapid rotational diffusion about the bilayer normal, each ^{15}N backbone amide site yields a single-line resonance and a ^{1}H -^{15}N dipolar coupling doublet that can be resolved in two-dimensional experiments.

Spin-exchange experiments rely on the presence of homonuclear dipole-dipole interaction between proximate nuclei to provide cross-peaks correlating pairs of nearby nuclei: a well-known example is the proton-driven spin diffusion (PDSD) experiment [20-22]. Perdeuteration of NAL with back-exchange of the amide ^{1}H drastically reduces the number of ^{1}H available for spin-exchange. There are two ^{1}H and one ^{15}N in each NAL molecule following synthesis with deuterated reagents and subsequent ^{1}H back-exchange; by contrast, without perdeuteration there are a total of fifteen ^{1}H and one ^{15}N in each NAL molecule. Direct comparisons of the results obtained from single crystals of these two samples demonstrate the effects of spin-dilution on the PDSD experiment. Similar comparisons can be made for the mismatched Hartmann-Hahn (MMHH) experiment [23] where irradiation at both ^{1}H and ^{15}N resonance frequencies effect ^{15}N-^{15}N spin-exchange through relays among ^{1}H nuclei [24]. This mechanism, which depends on intermediate ^{1}H spins between a pair of lower gamma spins undergoing exchange, is in contrast to the PDSD experiment where direct mixing occurs. The dilution of ^{1}H nuclei through replacement of many ^{1}H by ^{2}H and the implementation of homonuclear ^{1}H-^{1}H decoupling schemes have profound effects on the results of commonly used solid-state NMR experiments, such as resonance line-widths and intensities of spin-exchange cross-peaks.

2.2 Experimental

Sample preparation

Single crystals of NAL were prepared as described previously [25]. 100 mg of ^{15}N labeled L-leucine powder obtained from Cambridge Isotope Laboratories (www.isotope.com) was dissolved in 4 mL of warm glacial acetic acid and reacted with 0.8 mL of acetic anhydride. After solvent removal with a stream of nitrogen gas, the product was dissolved in 10 mL of warm high-performance liquid chromatography (HPLC) grade water and then lyophilized. 5 mL of a water-acetone mixture (1:1, v/v) was subsequently used to dissolve the synthesized N-Acetyl-L-Leucine (NAL). The solution was then passed through a 0.22 μm polyvinylidene fluoride syringe filter (www.emdmillipore.com). It was incubated for 4-10 days at room temperature until multiple 2 mg - 20 mg crystals could be harvested. Perdeuterated crystals were prepared following the same procedure except for the substitution of deuterated L-leucine and deuterated acetic anhydride, also obtained from Cambridge Isotope Laboratories, in the synthesis. The final crystallization step was carried out in a water-acetone solution at least four times in order to achieve complete ^{1}H back-exchange. Crystals with the "best" appearance were selected from the solution. An 8 mg ^{15}N labeled NAL single crystal and a 6 mg perdeuterated ^{15}N labeled NAL single crystal were used for the NMR experiments; they are referred to as the "protiated NAL" single crystal and the "perdeuterated NAL" single crystal, respectively.

Pf1 bacteriophage was prepared and purified as described previously [26]. Highly deuterated (>90%) and uniformly ^{15}N-labeled Pf1 bacteriophage were obtained by infecting *Pseudomonas aeruginosa* in Bioexpress cell growth media (U-^{2}H, 98%; U-^{15}N, 98%) and deuterium oxide (^{2}H, 99.9%) (www.isotope.com) [27]. The amide nitrogen sites were fully back-exchanged with ^{1}H by incubating the bacteriophage particles in ^1H_2O solution at 60^{o}C and pH 8 for 30 minutes, and then slowly cooling the solution to room temperature [28]. Pf1 coat protein-containing bicelles were prepared as described previously [19]. Here 2 mg of Pf1 coat protein was reconstituted in 25 mg of 1, 2-dimyristoyl-sn-glycero-3-phosphocholine (DMPC, www.anatrace.com) and mixed with a solution containing the detergent Triton X-100 (www.sigmaaldrich.com). The molar ratio (*q*) of DMPC to Triton X-100 was 5; and the DMPC concentration was 25% (w/v) in a total volume of 100 µL of 20 mM HEPES buffer at pH 6.7. For oriented sample solid-state NMR experiments, a flat-bottomed 15 mm long NMR tube with 4 mm OD (newera-spectro.com) was filled with approximately 90 µL of the protein-containing bicelle solution.

HDN triple resonance probe

Two HDN triple-resonance probes were built for the solid-state NMR experiments. The probe circuit diagrams are shown in Figure 2.1; the X channel represents the ^{2}H resonance frequency and the Y channel represents the ^{15}N resonance frequency. The probe associated with the circuit shown in Figure 2.1A has a single solenoid coil (L1) triple-tuned to the ^{1}H, ^{2}H, and ^{15}N resonance frequencies corresponding to a ^{1}H resonance frequency of 700 MHz; the 8-turn solenoid coil has a 3.2 mm inner diameter and an 8 mm length. C2, C3, C9, C10, C12, and C13 are variable capacitors (NMNT10-6ENL from Voltronics Corp., www.dovermpg.com). C5 is a fixed chip capacitor (700C from ATC Corp., www.atceramics.com) and its value is selected to isolate the ^{2}H and ^{15}N channels. L3 and C7 constitute a band-stop filter at the ^{2}H resonance frequency. C6 and L2 provide a band-stop filter for the ^{1}H channel.

The circuit shown in Figure 2.1B uses a cross-coil configuration: an outside loop-gap resonator (L1) is tuned for a ^{1}H resonance frequency of 900 MHz, and an inner solenoid coil (L3) is double-tuned for ^{2}H and ^{15}N resonance frequencies [29]. The loop-gap resonator (L1) has an inner dimension of 8.2 mm (width) by 7.75 mm (height) by 11.0 mm (length). The solenoid coil is an 8-turn 4 mm inner diameter coil with 0.25 mm thick Teflon coating. C3, C7, C13, C14, C17, and C18 are Voltronics variable capacitors (NMNT10-6ENL). C9, L2, and C11, L4 are two pairs of band-stop filters tuned to the ^{1}H channel: they are required to minimize the residual coupling between the loop-gap resonator and the solenoid coil. C8 is a fixed capacitor chosen to isolate the ^{15}N channel from the ^{2}H channel. L5 and C15 constitute a band-stop filter that isolates the ^{2}H channel from the ^{15}N channel. The fixed capacitor values and the probe performance measurements are in Table 2.1.

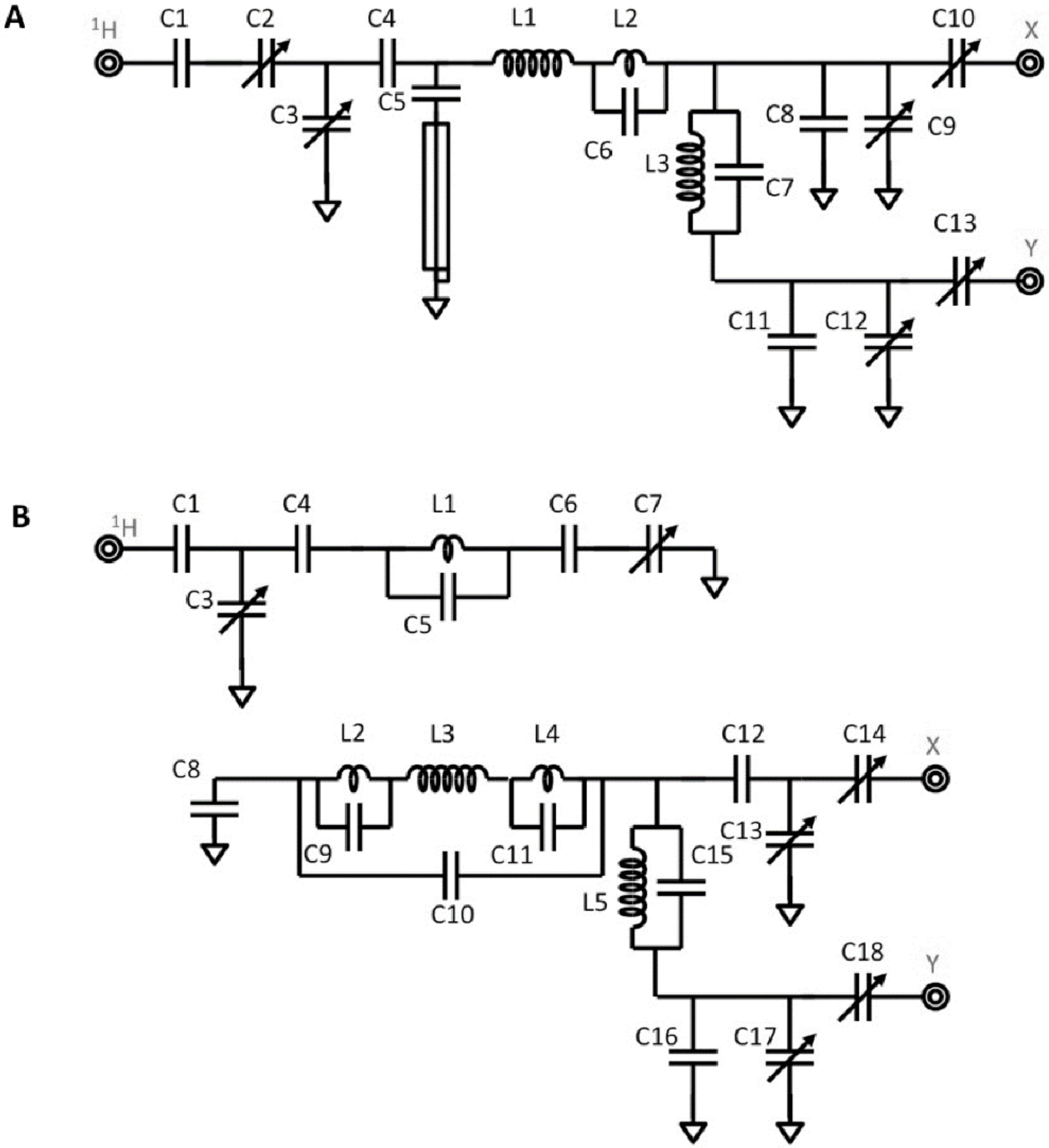

Figure 2.1. Circuit diagrams for triple-resonance HDN probes using (A) a single solenoid coil (L1) and (B) a cross-coil assembly with a loop-gap resonator (L1) and a solenoid coil (L3).

Table 2.1. Capacitance values used in the (A) 700 MHz and (C) 900 MHz probes. The circuit diagrams are depicted in Figure 2.1. The performance data for (B) 700 MHz and (D) 900 MHz using typical power levels.

A

700 MHz triple resonance HDN probe

Label	C1	C4	C5	C6	C7	C8	C11
Value(pf)	10	0.75	33	3.3	68	5.6	48

B

700 MHz triple resonance HDN probe

Nucleus	Power (W)	B_1 (kHz)
^{1}H	50	115
^{2}H	250	52.6
^{15}N	300	56.8

C

900 MHz triple resonance HDN probe

Label	C1	C4	C5	C6	C8	C9	C10	C11	C12	C15	C16
Value(pf)	5.6	1.1	2.2	1.1	15	3.9	1.5	3.9	18	39	27

D

900 MHz triple resonance HDN probe

Nucleus	Power (W)	B_1 (kHz)
^{1}H	200	51.5
^{2}H	80	20
^{15}N	400	46.3

NMR Experiments

Timing diagrams of the pulse sequences used to obtain the experimental data are shown in Figure 2.2. ^{2}H decoupling was used for the deuterated samples; the timing of the ^{2}H decoupling pulse can be found on the last block of each individual pulse sequence.

Separated local field (SLF) (Figure 2.2A) spectra for the NAL single crystal samples were acquired at a ^{1}H resonance frequency of 700 MHz with a 3 msec cross-polarization (CP) interval, 55 kHz ^{1}H B_1, 8 scans per t_1 value, and 10 msec acquisition times. Recycle delays of 4 sec and 20 sec were used for the protiated and perdeuterated NAL crystals, respectively. The dwell time for the indirect dimension was 20 µsec with 48 t_1 and 80 t_1 increments for the protiated and perdeuterated crystals, respectively. SPINAL-16 [30] decoupling was applied on the ^{1}H and ^{2}H channels following dipolar evolution with 70 kHz and 20 kHz power levels, respectively. SLF spectra for the magnetically oriented Pf1 coat protein bicelle samples were acquired at a 900 MHz ^{1}H frequency, using a 1 msec CP interval, 40 kHz ^{1}H B_1, 64 scans per t_1 and 10 msec acquisition time at 40°C, with the exception of the experiment shown in Figure 2.3, which had a 20 msec acquisition time. A recycle delay of 6 sec was used for both samples. Spectra for the Pf1 coat protein samples were acquired with a 40 kHz ^{1}H B_1. The dwell time for the indirect dimension was 20 µsec with 64 t_1 and 128 t_1 increments for the protiated and perdeuterated samples, respectively. SPINAL-16 decoupling was applied during signal acquisition, with 40 kHz and 10 kHz power levels on the ^{1}H and ^{2}H channels, respectively.

CP buildup experiments (Figure 2.2B) included a dwell time of 10 µsec for the NAL crystal during t_1, and 20 µsec for the Pf1 coat protein samples. Spectra from SAMPI4 experiments (Figure 2.2C) were acquired with a 70 kHz power level for both ^{1}H and ^{15}N B_1 for the NAL crystal samples and 35 kHz for the Pf1 coat protein samples. SPINAL-16 deuterium decoupling was applied during signal acquisition using 20 kHz B_1 power level for the perdeuterated NAL, and 10 kHz B_1 for perdeuterated Pf1. The ^{2}H quadrupole echo experiments were performed with 55 kHz SPINAL-16 ^{1}H decoupling. The recycle delay of 16 sec maximized the intensity of the signals between ± 20 kHz and ± 60 kHz.

The heteronuclear correlation (HETCOR, Figure 2.2D) experiments utilized SAMPI4 selective polarization transfer [31]. SPINAL-16 decoupling for the perdeuterated sample was applied during t_1 and t_2 acquisition on the ^2H channel. Spectra for both protiated and perdeuterated NAL single crystals were acquired with 4 scans and 256 t_1 increments at 70 kHz ^1H B_1 for SAMPI4 CP transfer, and decoupling during t_1 and t_2 acquisition. The HETCOR spectrum for the protiated NAL crystal was acquired with 4 SAMPI4 dwells for selective polarization transfer. The HETCOR spectrum for the perdeuterated NAL was acquired with 3 SAMPI4 dwells, and a ^2H decoupling power of 35 kHz. Spectra for the Pf1 coat protein samples were acquired with 35 kHz ^1H B_1 for SAMPI4 CP transfer, and decoupling t_2 acquisition, and 43 kHz during t_1 acquisition. Spectra for both protiated and perdeuterated Pf1 coat protein samples were acquired with 16 scans, 8 SAMPI4 dwells for selective polarization transfer, 6 sec recycle delay, 128 t_1 increments, and 5 msec acquisition time. 25 kHz and 10 kHz SPINAL-16 for ^1H and ^2H decoupling were used, respectively.

Spectra for PDSD experiments (Figure 2.2E) were acquired with 55 kHz ^1H B_1 and ^{15}N B_1 fields, for 32 scans, 128 t_1 points and 100 μsec dwell times in the indirect dimension. For the perdeuterated NAL sample, ^2H decoupling with SPINAL-16 at 20 kHz was applied during t_1 and signal acquisition. For both crystals, a spin-exchange mixing time of 10 sec was used. Spectra from MMHH experiments (Figure 2.2F) were acquired at 55 kHz, with SPINAL-16 ^1H decoupling at 55 kHz, and SPINAL-16 ^2H decoupling at 20 kHz during t_1 and t_2 acquisition. In these experiments, 32 scans were acquired, along with 64 t_1 points and 100 μsec dwell in the indirect dimension. The experiments utilized 4 sec z-filter and 10 msec mismatched Hartmann-Hahn irradiations. The level of Hartmann-

Hahn mismatch during the spin lock was 15% for the protiated NAL crystal and 5% for the perdeuterated NAL crystal.

Data processing was performed using the software programs NMRPipe [32] and Topspin 3.1 (www.bruker.com).

Figure 2.2. Timing diagrams of pulse sequences utilized to obtain the experimental data presented in the Figures. (A) Two-dimensional separated local field (SLF) experiment with no decoupling during t_1 and both ^1H and ^2H decoupling applied during data acquisition t_2. The 180° pulse refocuses the ^{15}N chemical shift. (B) One-dimensional cross-polarization (CP) experiment where the interval for magnetization transfer is varied. ^1H and ^2H decoupling are applied during data acquisition. The intensities of individual signals are monitored as a function of time, as illustrated in Figure 2.8. (C) SAMPI4 experiment with ^1H and ^2H decoupling applied during data acquisition t_2. (D) Heteronuclear correlation (HETCOR) experiment with ^1H and ^2H decoupling applied during the incremented t_1 period and data acquisition t_2. (E) Proton-driven spin diffusion (PDSD) experiment with ^1H and ^2H decoupling applied during the incremented t_1 period and data acquisition t_2. (F) Mismatched Hartmann-Hahn (MMHH) experiment with ^1H and ^2H decoupling applied during the incremented t_1 period and data acquisition t_2.

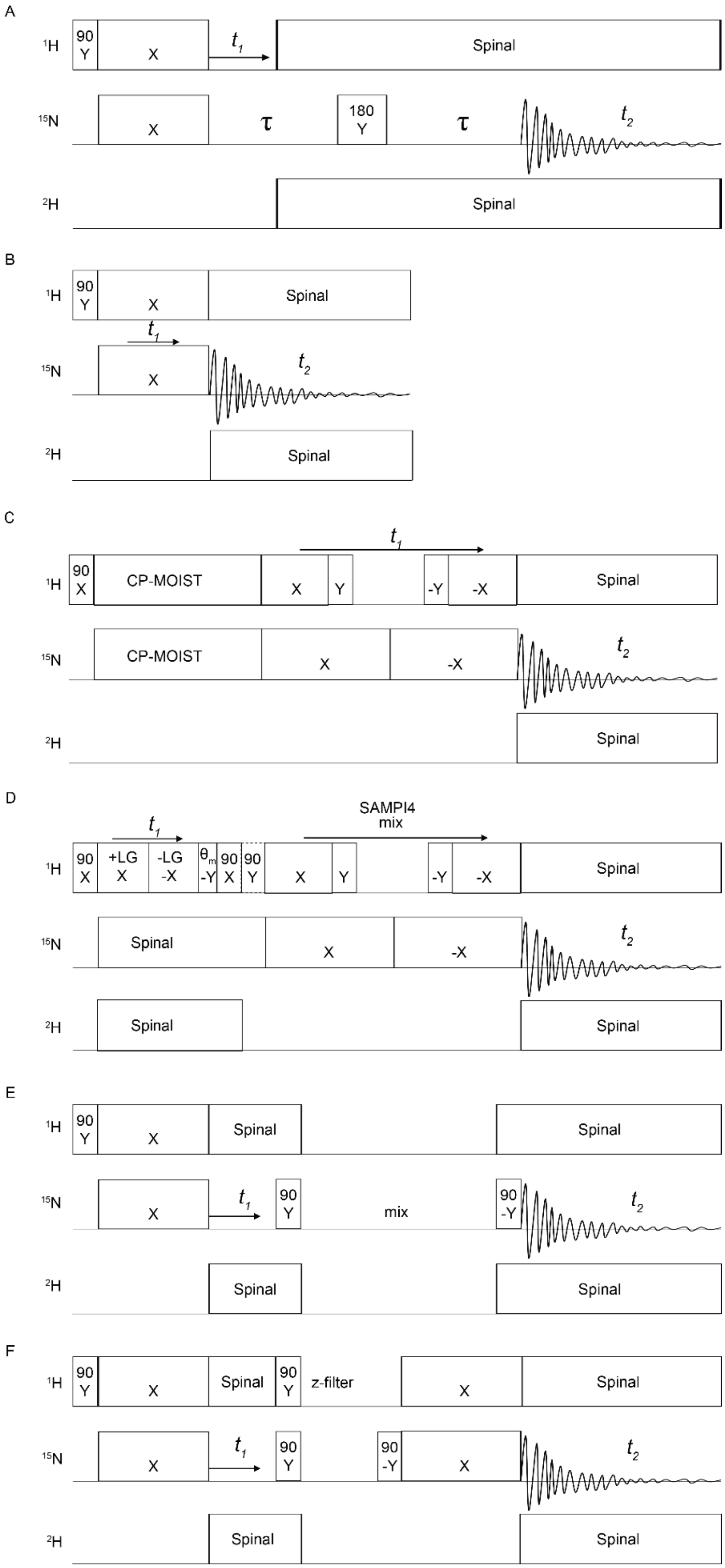
A
¹H
90
Y
X
t1
Spinal
¹⁵N
X
τ
180
Y
τ
t2
²H
Spinal
B
¹H
90
Y
X
Spinal
¹⁵N
t1
X
t2
²H
Spinal
C
t1
¹H
90
X
CP-MOIST
X
Y
-Y
-X
Spinal
¹⁵N
CP-MOIST
X
-X
t2
²H
Spinal
D
t1
SAMPI4
mix
¹H
90
X
+LG
X
-LG
-X
θm
-Y
90
X
90
Y
X
Y
-Y
-X
Spinal
¹⁵N
Spinal
X
-X
t2
²H
Spinal
Spinal
E
¹H
90
Y
X
Spinal
Spinal
¹⁵N
X
t1
90
Y
mix
90
-Y
t2
²H
Spinal
Spinal
F
¹H
90
Y
X
Spinal
90
Y
z-filter
X
Spinal
¹⁵N
X
t1
90
Y
90
-Y
X
t2
²H
Spinal
Spinal

2.3 Results

^{2}H decoupling

The spectra in Figure 2.3 demonstrate the broadening effect of nearby deuterons on ^{15}N resonances. In the NAL crystal, the ^{1}H nuclei on carbon sites contribute approximately 200 Hz - 250 Hz to the ^{15}N resonance line-widths (Figure 2.3C). The effects of perdeuteration on the spectra are different in Pf1 protein, where the broadening is reduced by the rapid rotational diffusion of the membrane-bound form of the protein in the bilayer environment (Figure 2.3F). Application of ^{2}H decoupling attenuates the broadening effects of the deuterons on the ^{15}N sites, resulting in narrow lines in the perdeuterated samples (Figure 2.3B and 2.3E). In Figure 2.3A the frequencies of the 4 resonances are different compared to those in Figure 2.3B and 3C, due to slight differences in the crystal orientation. The frequencies of the deuterium sites are measured with the quadruple-echo experiment (Figure 2.4B), the furthest resonance from the center of the spectrum resides at ±59 kHz. The orientation of the crystal used to obtain the data in Figure 2.4A is slightly different from that used in Figure 2.3A and C. The large quadrupole splittings shown in Figure 2.4B illustrate the challenges in decoupling ^{2}H from ^{15}N if the conventional single quantum decoupling process is considered.

The power requirements for ^{2}H decoupling were determined using the data shown in Figure 2.5. The ^{1}H decoupling power is fixed and the power of the irradiation at the ^{2}H resonance frequency is varied between 0 kHz and 30 kHz for the single crystal sample (Figure 2.5A), and between 0 kHz and 20 kHz for the aligned membrane protein sample

(Figure 2.5B). Complete ^{2}H decoupling of the stationary NAL single crystal sample requires 20 kHz of power while the oriented Pf1 coat protein sample undergoing rotational diffusion requires only 10 kHz of power. Significantly, perdeuterated NAL with adequate ^{1}H and ^{2}H decoupling (Figure 2.3B) and protiated NAL with ^{1}H decoupling (Figure 2.3A) have similar ^{15}N resonance line-widths. Perdeuteration also did not affect the ^{15}N resonance line-widths of a ^{1}H back-exchanged sample of uniformly ^{2}H and ^{15}N labeled Pf1 coat protein in bicelles (Figure 2.3E) compared to those of the protiated sample (Figure 2.3D).

The fully decoupled spectra of NAL and of membrane-bound Pf1 coat protein have ^{15}N resonance line-widths of ~140 Hz and ~90 Hz, respectively. The representation of the unit cell for the perdeuterated NAL single crystal shown in Figure 2.4D is based on the crystal structure (CCDC 624793 [34]). At the particular crystal orientation that gives the ^{15}N NMR spectrum shown Figure 2.4A; the corresponding ^{2}H NMR spectrum was obtained with the quadrupole-echo experiment (Figure 2.4B). For comparison, a simulated rigid lattice ^{2}H NMR powder pattern for a C-D bond is shown with the solid line and the corresponding spectrum for a CD_3 group undergoing rapid three-fold reorientation is shown with the dashed line in Figure 2.4C.

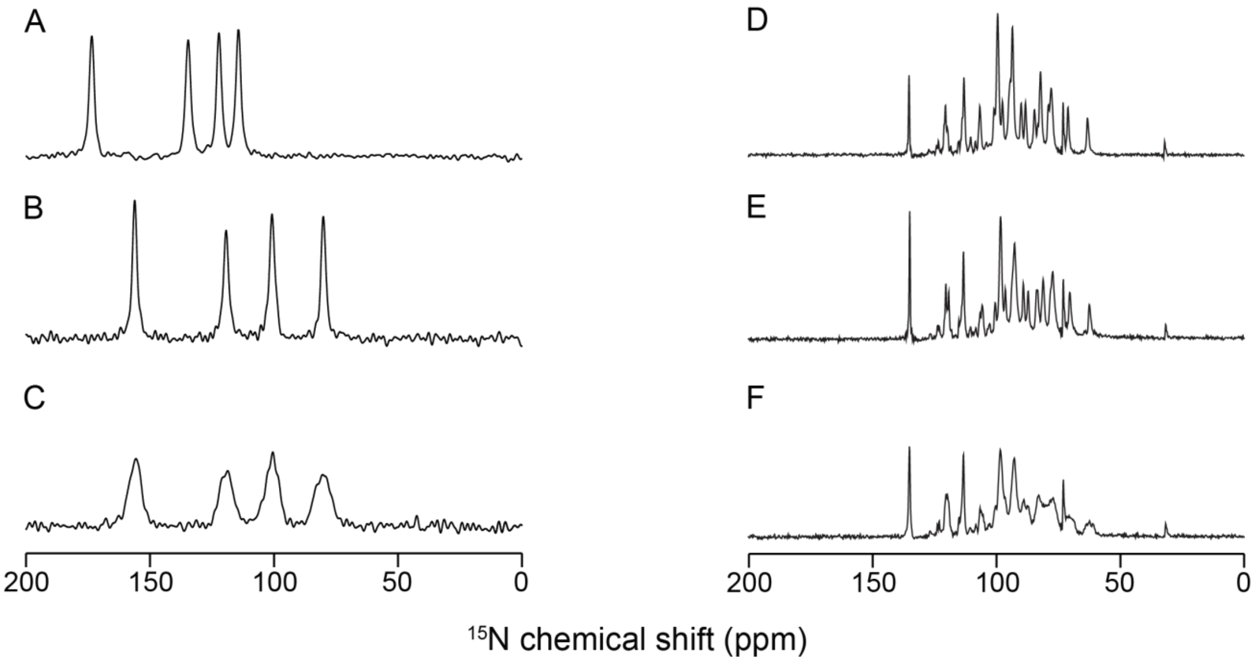

Figure 2.3. Experimental ^{15}N NMR spectra showing the effects of ^{2}H decoupling on ^{1}H decoupled ^{15}N resonances. The ^{1}H resonance frequency was 700 MHz for spectra (A-C) and 900 MHz for spectra (D-F). (A) Protiated ^{15}N labeled NAL single crystal. (B and C) Perdeuterated ^{15}N labeled NAL single crystal. (D) Uniformly ^{15}N labeled Pf1 coat protein. (E and F) Perdeuterated and uniformly ^{15}N labeled Pf1 coat protein. The protein samples in (D-F) were oriented in DMPC: Triton X-100 *q*=5 bicelles with their bilayer normals perpendicular to the direction of the magnetic field. Spectra (B) and (E) were acquired with the application of 20 kHz and 10 kHz SPINAL-16 ^{2}H decoupling, respectively. Spectra (C and F) were acquired without ^{2}H decoupling during data acquisition. Spectra (A-C) were acquired with the application of 50 kHz SPINAL-16 ^{1}H decoupling during the 10 msec acquisition time. Spectra (D-F) were acquired with the application of 45 kHz SPINAL-16 ^{1}H decoupling during the 20 msec acquisition time.

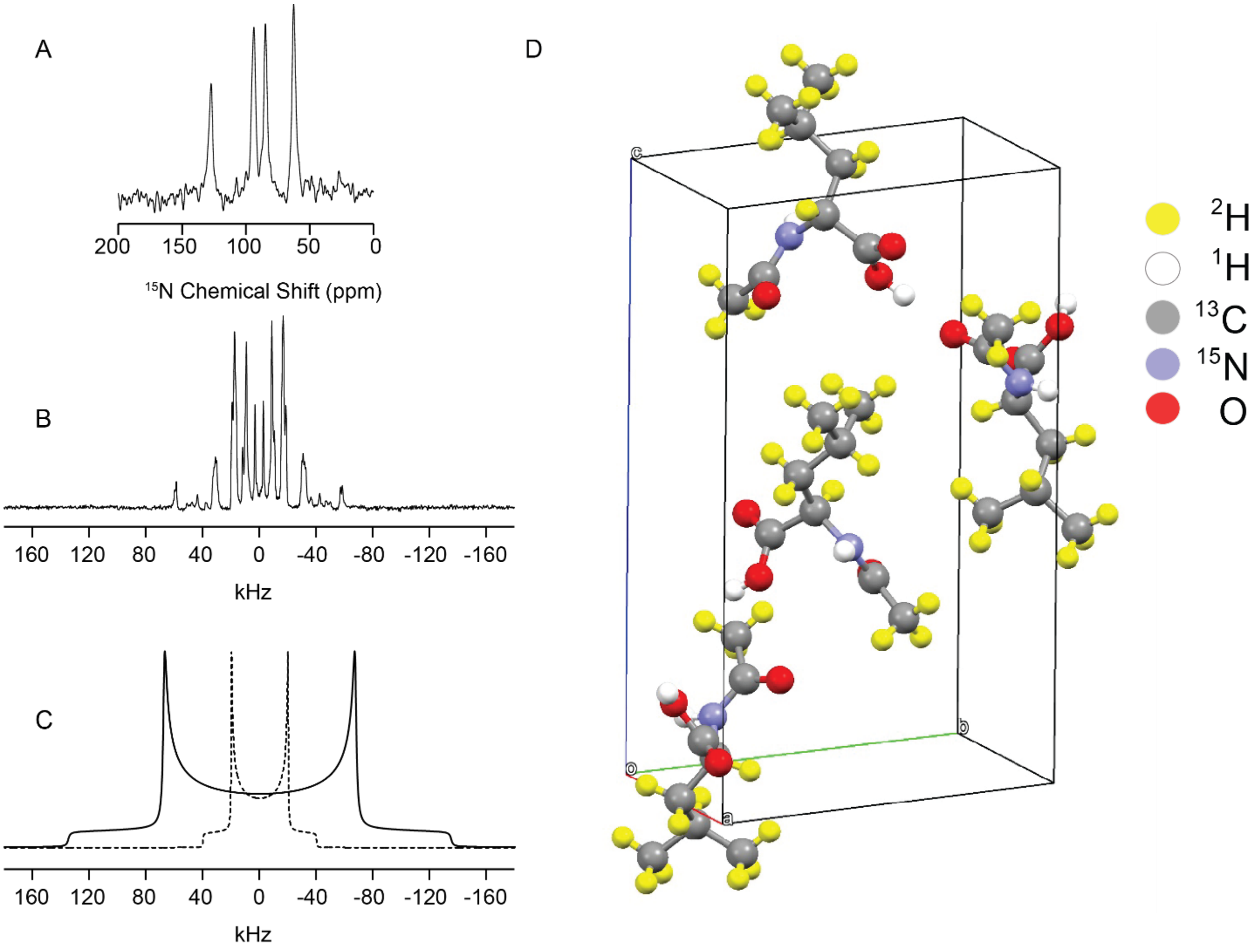

Figure 2.4. (A) ^{15}N NMR spectrum of the perdeuterated ^{15}N labeled NAL crystal used in Figure 2.3 with 50 kHz ^{1}H SPINAL-16 and 40 kHz ^{2}H SPINAL-16 decoupling applied during data acquisition. (B) ^{2}H NMR spectrum obtained with ^{2}H 55 kHz pulses during the quadrupole-echo experiment at the same crystal orientation as Figure 2.4A. 55 kHz ^{1}H SPINAL-16 decoupling was applied during signal acquisition. (C) Calculated powder patterns for the CD (solid line) and CD_3 sites (dashed line) on perdeuterated NAL [33]. (D) An illustration of the unit cell of the NAL single crystal. The ^{2}H atoms shown in yellow are placed in the positions predicted for the ^{1}H atoms based on the NAL crystal structure [34].

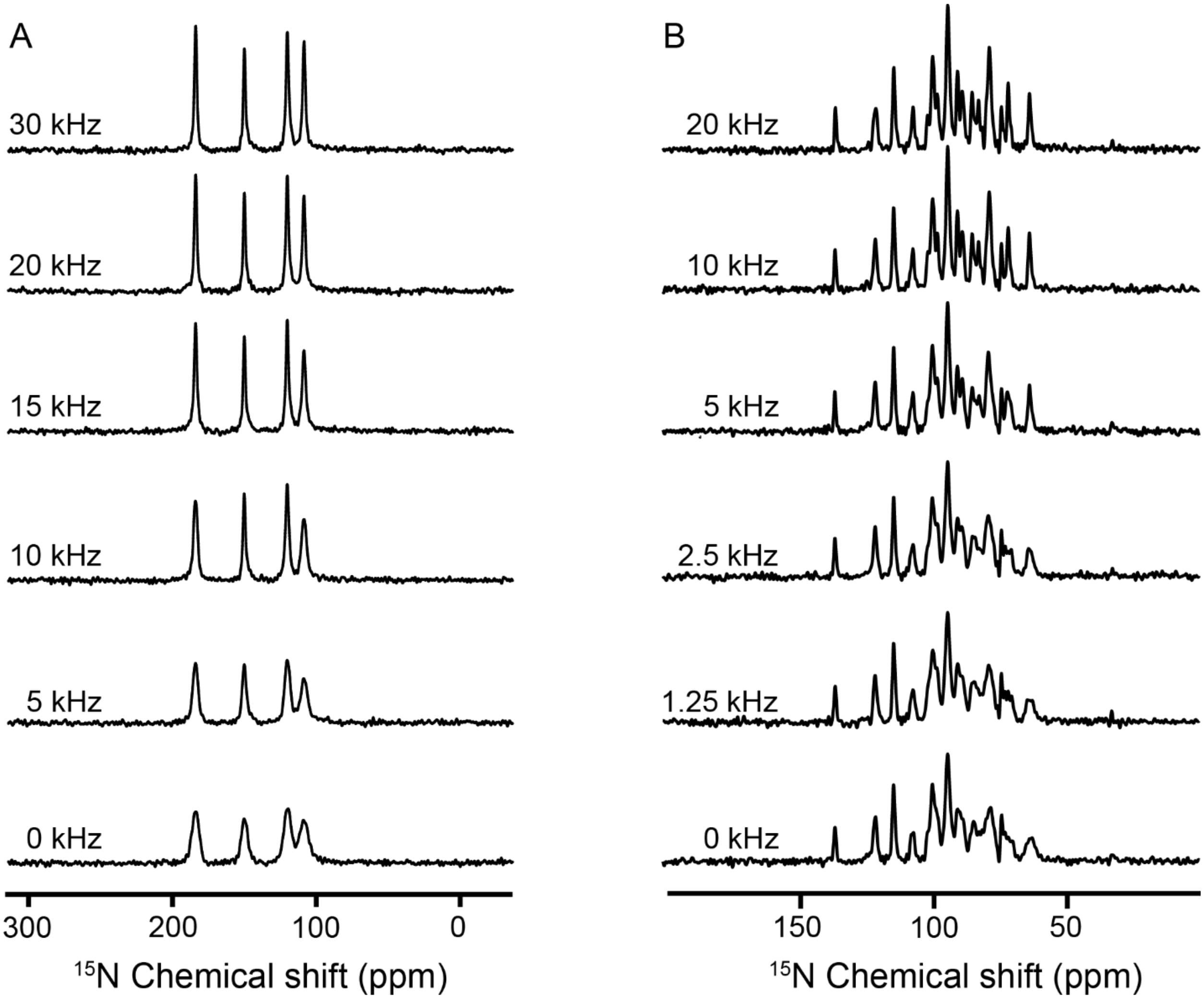

Figure 2.5. Effects of ^{2}H decoupling on ^{1}H decoupled ^{15}N resonances. The ^{1}H resonance frequency was 700 MHz for (A) and 900 MHz for (B). (A) Perdeuterated ^{15}N labeled NAL single crystal. (B) Uniformly ^{15}N and ^{2}H labeled Pf1 coat protein (^{1}H back-exchanged) in DMPC: Triton X-100 *q*=5 bicelles oriented with their bilayer normals perpendicular to the direction of the magnetic field. Spectra in (A) and (B) were acquired with 50 kHz ^{1}H SPINAL-16 decoupling. As marked in the figures, the spectra were acquired with SPINAL-16 modulated ^{2}H irradiation during data acquisition with radiofrequency powers ranging from 0 kHz to 30 kHz (A), and 0 kHz to 20 kHz (B).

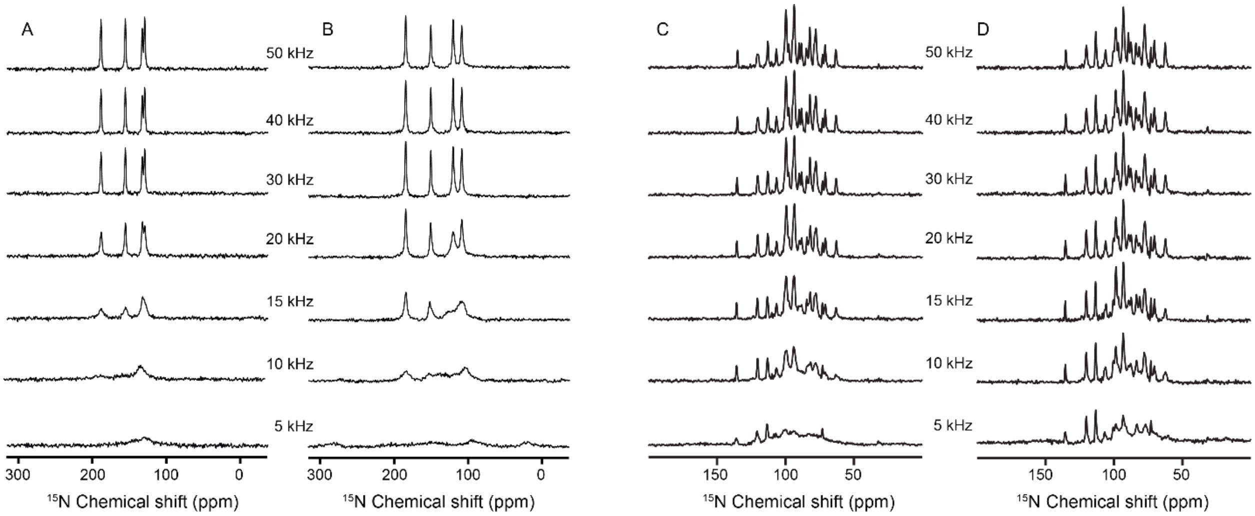

Figure 2.6. Effects of ^{1}H decoupling on ^{2}H decoupled ^{15}N resonances. The ^{1}H resonance frequency was 700 MHz for the spectra in (A) and (B) and 900 MHz for the spectra in (C) and (D). (A) Protiated ^{15}N labeled NAL single crystal at an arbitrary orientation. (B) Perdeuterated ^{15}N labeled NAL single crystal at a similar orientation. (C) Uniformly ^{15}N labeled Pf1 coat protein in DMPC: Triton X-100 q=5 bicelles. (D) Uniformly ^{2}H and ^{15}N labeled Pf1 coat protein (^{1}H back-exchanged) in DMPC: Triton X-100 q=5 bicelles. (C) and (D) were oriented with the bilayer normals perpendicular to the direction of the magnetic field. All spectra in (B) were acquired with 20 kHz ^{2}H SPINAL-16 decoupling, and all spectra in (D) were acquired with 10 kHz ^{2}H SPINAL-16 decoupling. As marked in the figure, the spectra were acquired with ^{1}H SPINAL-16 irradiation at radiofrequency powers ranging between 5 kHz and 50 kHz.

^{1}H decoupling

The one-dimensional ^{15}N NMR spectra in Figure 2.6 were acquired with adequate ^{2}H decoupling and variable levels of ^{1}H decoupling. The goal was to determine whether deuteration of the carbon sites affects the radiofrequency power required to decouple the ^{1}H from the ^{15}N at the labeled amide sites in the NAL crystal and in the oriented membrane protein sample. Narrow ^{15}N resonance line-widths were obtained only when the ^{1}H power was greater than 30 kHz; notably, the power required for complete ^{1}H decoupling did not differ between NAL samples with ^{1}H or ^{2}H bonded to the carbon sites. Similarly, the protein samples required ^{1}H power greater than 20 kHz for decoupling, regardless of whether the carbon sites were deuterated or not. The data in Figure 2.6 show that perdeuteration does not reduce the magnitude of the ^{1}H irradiation required to effect heteronuclear decoupling in stationary samples of crystals or oriented proteins in hydrated phospholipid bilayers.

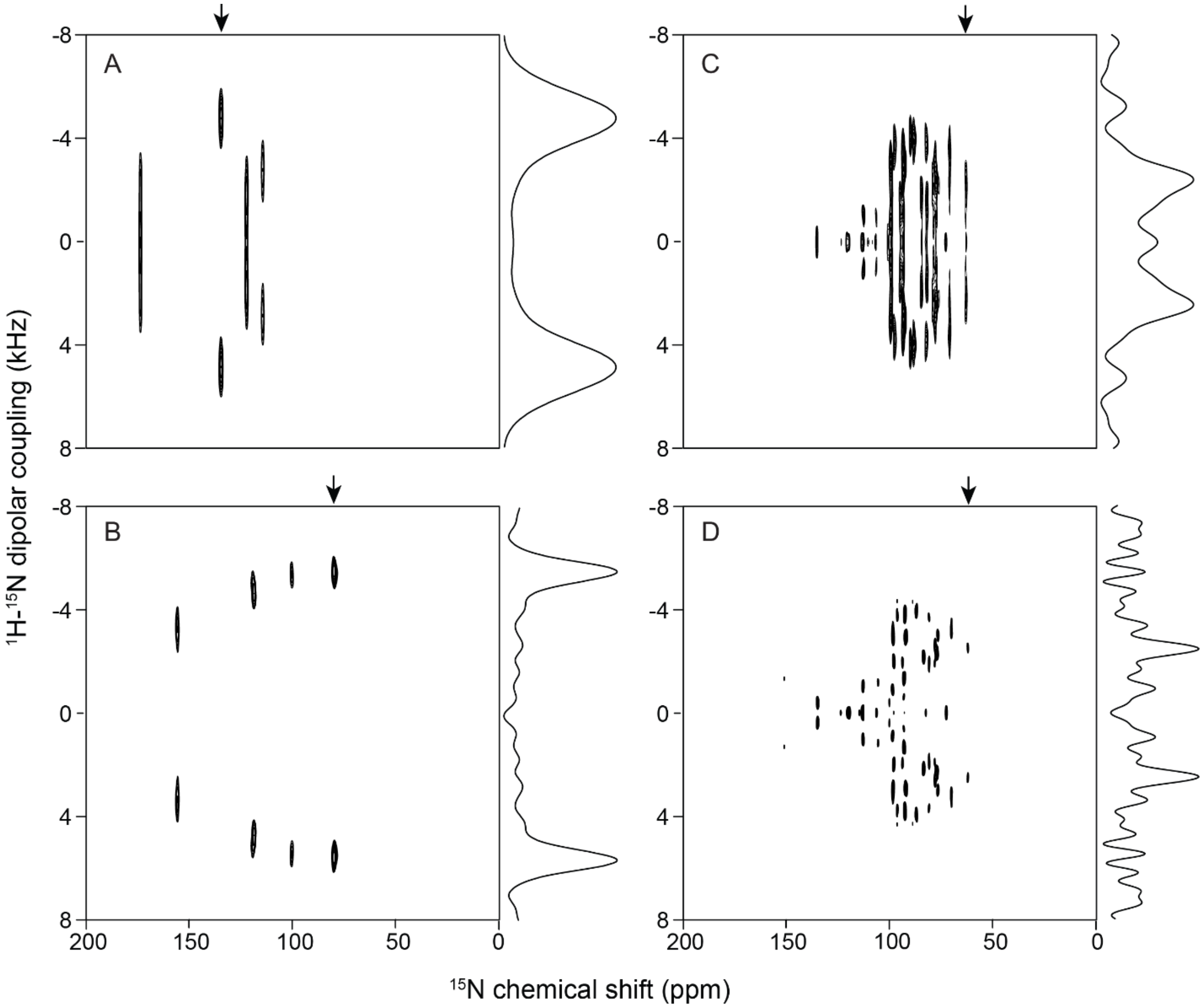

Figure 2.7. Effects of perdeuteration on two-dimensional ^{1}H-^{15}N SLF spectra. The ^{1}H resonance frequency was 700 MHz for spectra (A) and (B) and 900 MHz for spectra (C) and (D). (A) Protiated ^{15}N labeled NAL single crystal at an arbitrary orientation. (B) Perdeuterated ^{15}N labeled NAL single crystal at an arbitrary orientation. (C) Uniformly ^{15}N labeled Pf1 coat protein in DMPC: Triton X-100 *q*=5 bicelles. (D) Uniformly ^{2}H and ^{15}N labeled Pf1 coat protein (^{1}H back-exchanged) in DMPC: Triton X-100 *q*=5 bicelles. (C) and (D) were oriented with their bilayer normals perpendicular to the direction of the magnetic field. Spectrum (B) was acquired with 20 kHz ^{2}H SPINAL-16 decoupling and spectrum (D) was acquired with 10 kHz ^{2}H SPINAL-16 decoupling. Spectral slices through the marked resonances are shown on the right side of the two-dimensional spectra. The line-widths in the ^{1}H-^{15}N heteronuclear dipolar coupling frequency dimension are 2.2 kHz for (A) and 0.85 kHz for (B).

^{1}H-^{15}N Dipolar Coupling

Perdeuteration has a significant effect on line-widths in the heteronuclear dipolar coupling frequency dimension of separated local field (SLF) spectra (Figure 2.7B and D). The resonance line-widths of the perdeuterated samples are significantly narrower in Figure 2.7B and D than those in Figure 2.7A and C. The narrowest line-width observed in the protiated NAL crystal is 2.2 kHz (marked with an arrow in Figure 2.7A), in contrast the narrowest linewidth is 0.85 kHz for the perdeuterated sample (marked with an arrow in Figure 2.7B). Similar levels of line-width reduction are observed in samples of the membrane protein with perdeuteration (Figure 2.7C and D). In CP buildup curves, the perdeuterated samples have their dipolar oscillations extend longer than 1 msec (Figure 2.8B and D), which is consistent with the deuterons isolating the ^{1}H nuclei. Notably, improvements in the line-widths of the heteronuclear dipolar couplings in the perdeuterated samples were not observed in SAMPI4 experiments (Figure 2.9).

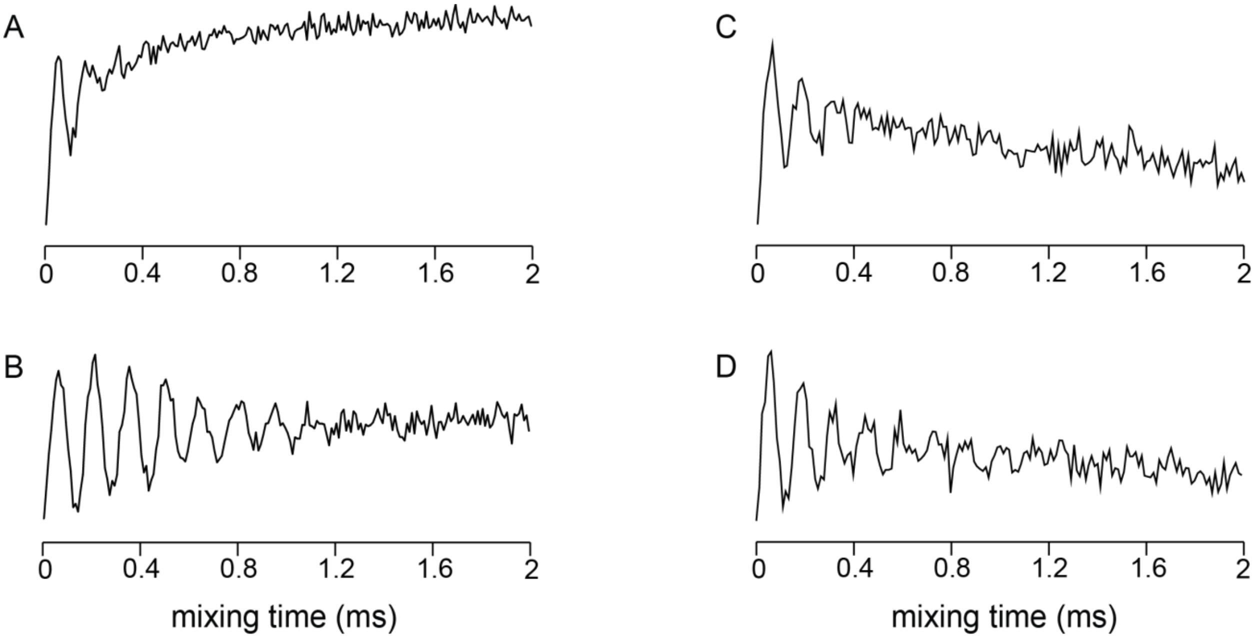

Figure 2.8. Effects of perdeuteration on selected ^{1}H-^{15}N cross-polarization buildup curves. The ^{1}H resonance frequency was 700 MHz for spectra (A) and (B) and 900 MHz for spectra (C) and (D). (A) Protiated ^{15}N labeled NAL single crystal. (B) Perdeuterated ^{15}N labeled NAL single crystal. (C) Uniformly ^{15}N labeled Pf1 coat protein in DMPC: Triton X-100 *q*=5 bicelles. (D) Uniformly ^{2}H and ^{15}N labeled Pf1 coat protein (^{1}H back-exchanged) in DMPC: Triton X-100 *q*=5 bicelles. (C) and (D) were oriented with their bilayer normals perpendicular to the direction of the magnetic field. (A) and (B) were acquired with 20 kHz ^{2}H SPINAL-16 decoupling and (C) and (D) were acquired with 10 kHz ^{2}H SPINAL-16 decoupling.

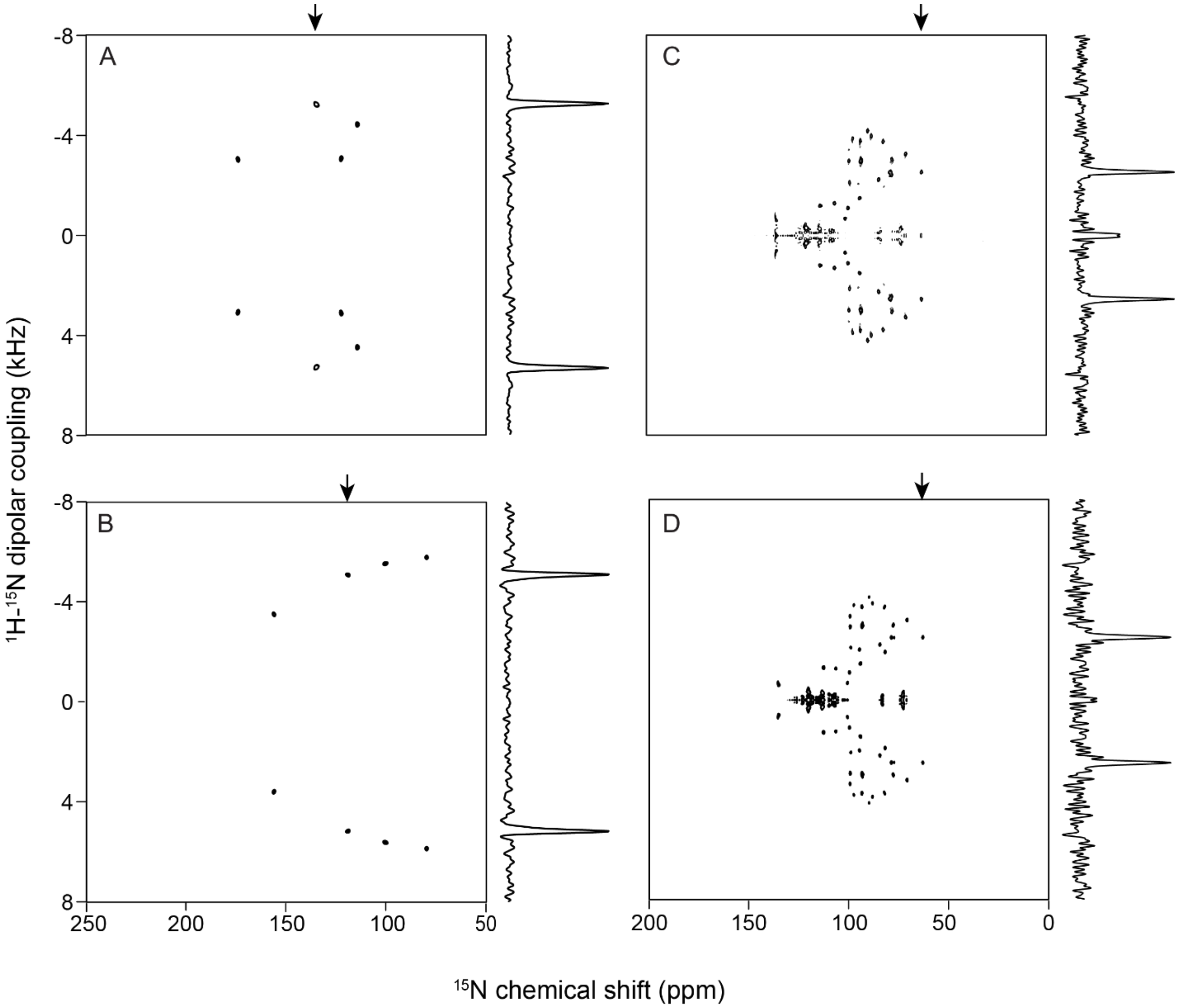

Figure 2.9. Effects of perdeuteration on two-dimensional SAMPI4 spectra. The ^{1}H resonance frequency was 700 MHz for spectra (A) and (B) and 900 MHz for spectra (C) and (D). (A) Protiated ^{15}N labeled NAL single crystal. (B) Perdeuterated ^{15}N labeled NAL single crystal. (C) Uniformly ^{15}N labeled Pf1 coat protein in DMPC: Triton X-100 *q*=5 bicelles. (D) Uniformly ^{2}H and ^{15}N labeled Pf1 coat protein (^{1}H back-exchanged) in DMPC: Triton X-100 *q*=5 bicelles. The samples in (C) and (D) were oriented with their bilayer normals perpendicular to the direction of the magnetic field. Spectrum (B) was acquired with 20 kHz ^{2}H SPINAL-16 decoupling and spectrum (D) was acquired with 10 kHz ^{2}H SPINAL-16 decoupling. Representative spectral slices at the marked ^{1}H-^{15}N heteronuclear dipolar coupling frequencies are shown on the right side of the spectra.

^{1}H-^{15}N HETCOR

The results of two-dimensional ^{1}H-^{15}N heteronuclear correlation (HETCOR) experiments, where the ^{1}H chemical shift evolves under FSLG magic angle ^{1}H-^{1}H homonuclear decoupling during the t_1 interval are shown in Figure 2.10. The arrows point to the signals selected for analysis in the ^{1}H chemical shift frequency dimension; the corresponding spectral slices are plotted along the vertical-axis. The vertical-axis is the ^{1}H chemical shift dimension obtained in the presence of both ^{1}H-^{1}H homonuclear and ^{1}H-^{15}N heteronuclear decoupling applied during the t_1 interval. The ^{1}H line-width observed in the perdeuterated NAL crystal spectrum (560 Hz, Figure 2.10B) and that from the protiated crystal (670 Hz, Figure 2.10A) are similar. Comparable results were obtained for the oriented Pf1 coat protein under the same conditions (Figure 2.10C and D).

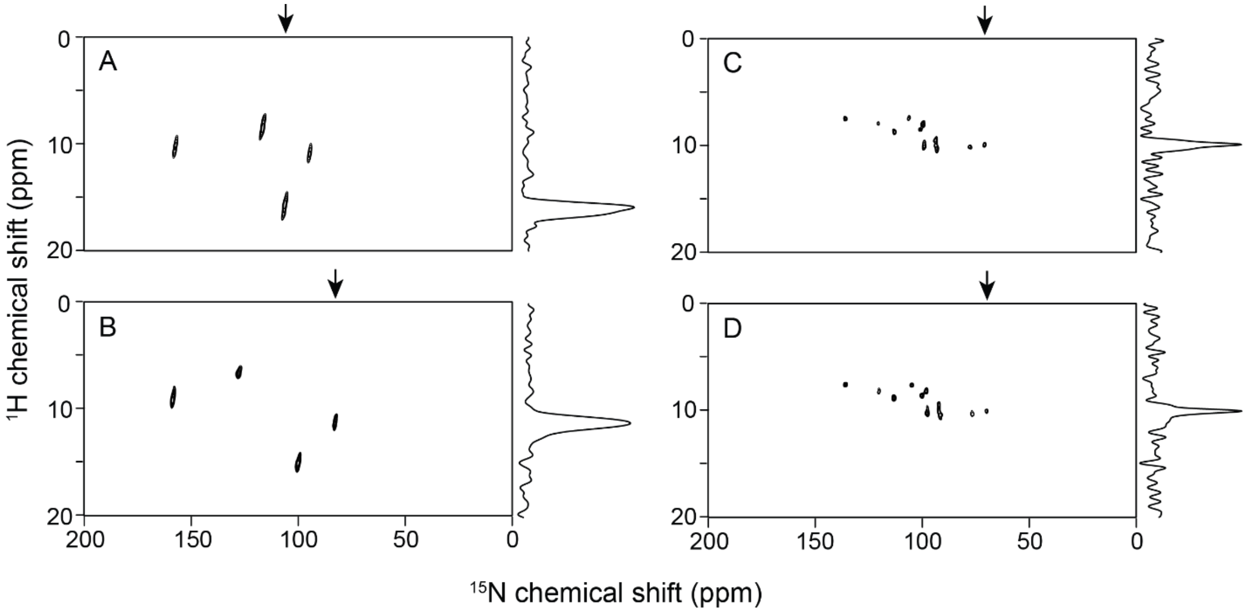

Figure 2.10. Effects of perdeuteration on two-dimensional ^{1}H-^{15}N heteronuclear correlation (HETCOR) experiments. The ^{1}H resonance frequency was 700 MHz for (A) and (B) and 900 MHz for (C) and (D). (A) Protiated ^{15}N labeled NAL single crystal. (B) Perdeuterated ^{15}N labeled NAL crystal. (C) Uniformly ^{15}N labeled Pf1 coat protein in DMPC: Triton X-100 *q*=5 bicelles. (D) Uniformly ^{2}H and ^{15}N labeled Pf1 coat protein (^{1}H back-exchanged) in DMPC: Triton X-100 *q*=5 bicelles. Samples used in (C) and (D) were oriented with the bilayer normals perpendicular to the direction of the magnetic field. The spectrum in (B) was acquired with 20 kHz ^{2}H SPINAL-16 decoupling and the spectrum in (D) was acquired with 10 kHz of ^{2}H SPINAL-16 decoupling. Spectra in (A) and (B) were acquired with 70 kHz ^{1}H power during t_1 while spectra (C) and (D) were acquired with 43 kHz ^{1}H power. Selected spectral slices in the ^{1}H chemical shift dimension are shown on the right side of the two-dimensional spectra.

Spin-exchange experiments

PDSD spin-exchange experiments were performed on both protiated (Figure 2.11A - C) and perdeuterated (Figure 2.11D - F) NAL crystals. Similar cross-peak intensities were observed for both samples (Figure 2.11C vs. F). Because the two crystals have slightly different orientations in the magnetic field, cross-peak intensities are more clearly compared in the slices (Figure 2.11B and E) rather than the contour plots (Figure 2.11C and F). In the MMHH experiment (Figure 2.12), however, stronger diagonal and cross-peak intensities are observed in the spectra of the perdeuterated NAL crystal (Figure 2.12E and F) than of the protiated NAL crystal (Figure 2.12B and C). To facilitate the presentation of the results in Figure 2.12, the spectra are further analyzed in Figure 2.13. First of all, horizontal slices through each diagonal resonances are shown in Figure 2.13A and B. The diagonal resonances are distinguished from the off-diagonal resonances by asterisks. It can be easily seen from the one-dimensional slices that all off-diagonal resonances are present; this is in contrast to the two-dimensional spectra shown in Figure 2.12 where one of the weakest off-diagonal resonances in each spectrum cannot be seen because it is too close to the noise levels. To demonstrate the levels of sensitivity enhancement in the MMHH experiment due to perdeuteration, the intensities of the resonances in the two-dimensional spectra shown in Figure 2.12 are quantified, normalized, and ranked in Figure 2.13C. Because the two crystals are not at the same orientation, comparisons cannot be made by examining the resonances with the same chemical shifts. To demonstrate the variable intensities of the resonances in the two-dimensional spectra, we chose the method of ranking the resonances based on their measured intensities. Comparisons of the intensity distribution ranked from high-to-low for the two crystals demonstrate that with perdeuteration, significant sensitivity enhancements can be obtained for the diagonal resonances, while lower levels of enhancements can be obtained with the off-diagonal resonances. The intensities shown in Figure 2.13C are raw S/N values measured from data in Figure 2.13A and B, and not subject to adjustments based on the crystal sizes.

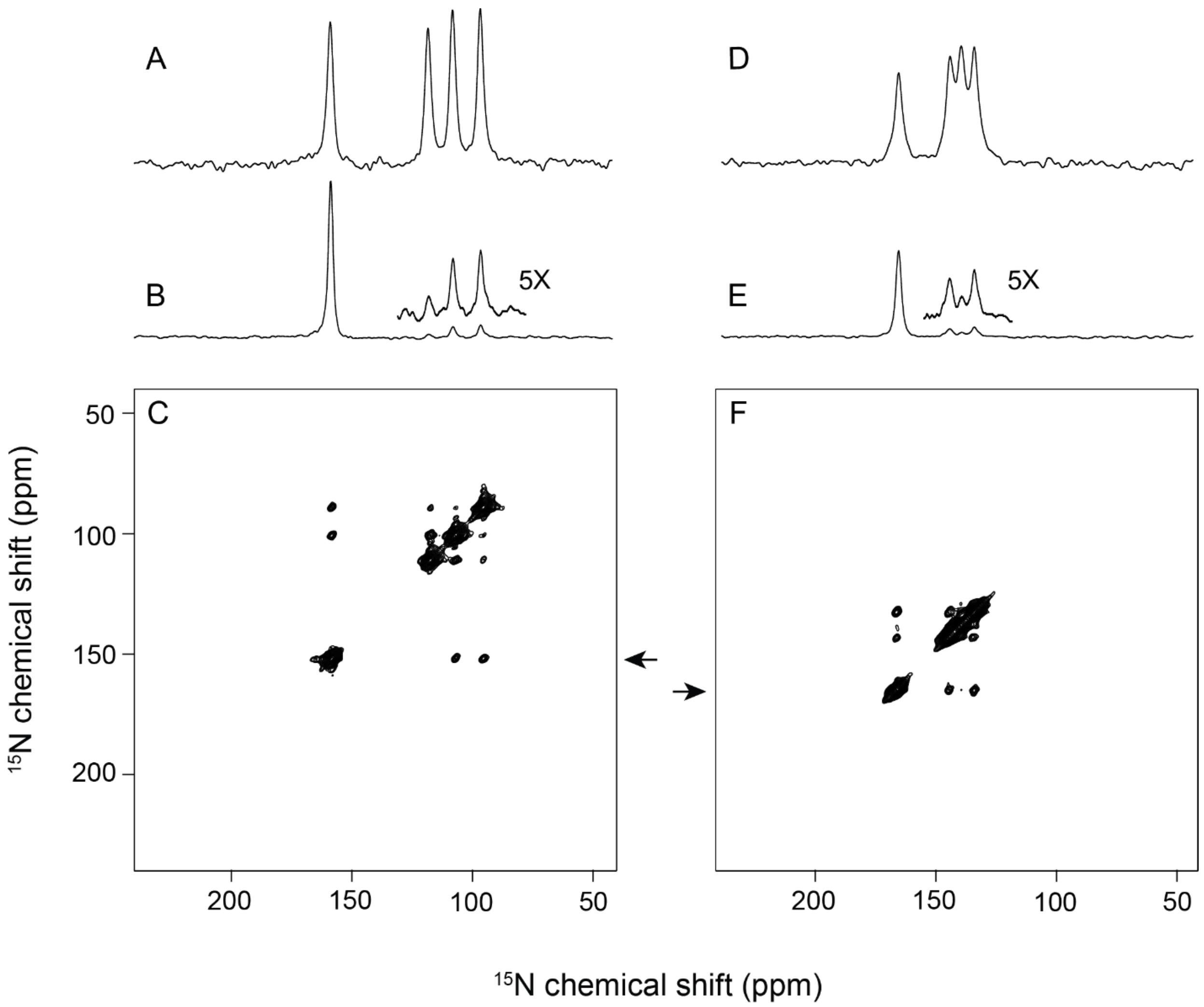

Figure 2.11. Effects of perdeuteration on two-dimensional PDSD spectra. The ^{1}H resonance frequency was 700 MHz. (A) - (C) Spectra of protiated ^{15}N labeled NAL single crystal. (D) - (F) Spectra of the perdeuterated ^{15}N labeled NAL single crystal. (A) and (D) are one-dimensional CP spectra of single crystals in which four distinct signals demonstrate that there are four unique molecules in each unit cell of the crystal. Spectrum in (B) is a slice through the spectrum in (C) taken at the marked frequency. 5X vertically expanded cross-peaks are shown above the slice. (C) is the PDSD spectrum of the protiated ^{15}N labeled NAL single crystal obtained with a 10 sec mix time. (E) is a slice through the spectrum in (F) at the marked frequency. The vertically expanded cross-peaks are shown above the slice. (F) is the PDSD spectrum of the perdeuterated labeled single crystal with a 10 sec mix time. Spectra in (C) and (F) are processed with 100 Hz of exponential line broadening in the F1 and F2 frequency dimensions. Both the one- and two- dimensional spectra resulted from signal averaging 32 scans.

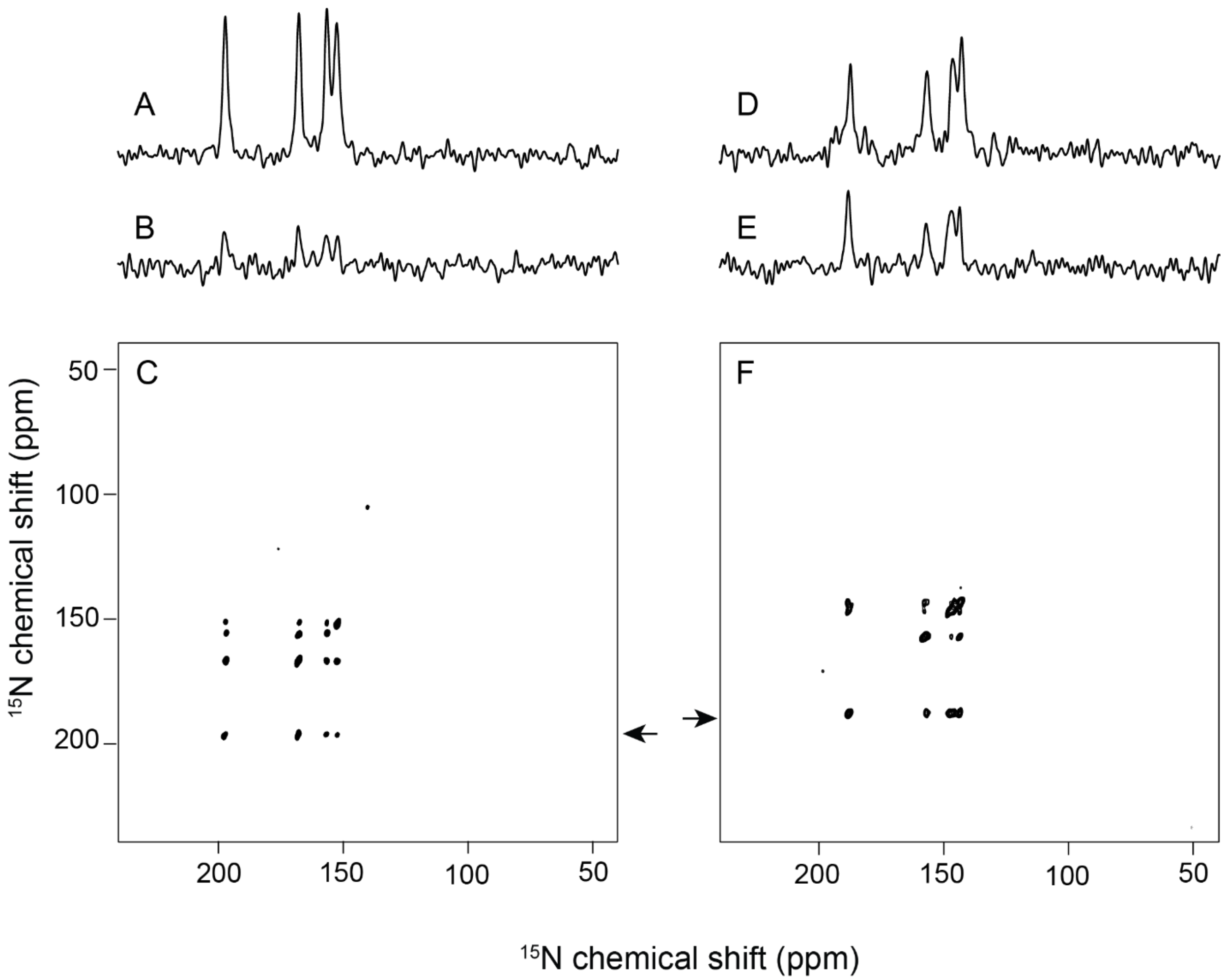

Figure 2.12. Effects of perdeuteration on two-dimensional MMHH spectra. The ^{1}H resonance frequency was 700 MHz. (A) is a one-dimensional CP spectrum of a protiatated ^{15}N labeled NAL single crystal. (D) is a one-dimensional CP spectrum of a perdeuterated ^{15}N labeled NAL single crystal. (C) is an MMHH spectrum from a protiated ^{15}N labeled NAL single crystal. (F) is an MMHH spectrum from a perdeuterated ^{15}N labeled NAL single crystal. (B) is a one-dimensional slice through spectrum (C) taken at the marked position. The spectrum (C) was acquired with 10 msec MMHH pulse at a 15% mis-match level. (E) is a one-dimensional slice taken at the marked position through spectrum (F). The MMHH experiment on a perdeuterated ^{15}N labeled NAL single crystal was performed with a 10 msec MMHH pulse at a 5% mis-match level. Spectra (C) and (F) were both processed with 40 Hz line broadening in the F2 dimension (horizontal) and 100 Hz line broadening in the F1 dimension (vertical). The one-dimensional spectra were obtained with 4 scans and the two-dimensional ^{15}N labeled NAL single crystal spectra were obtained with 32 scans.

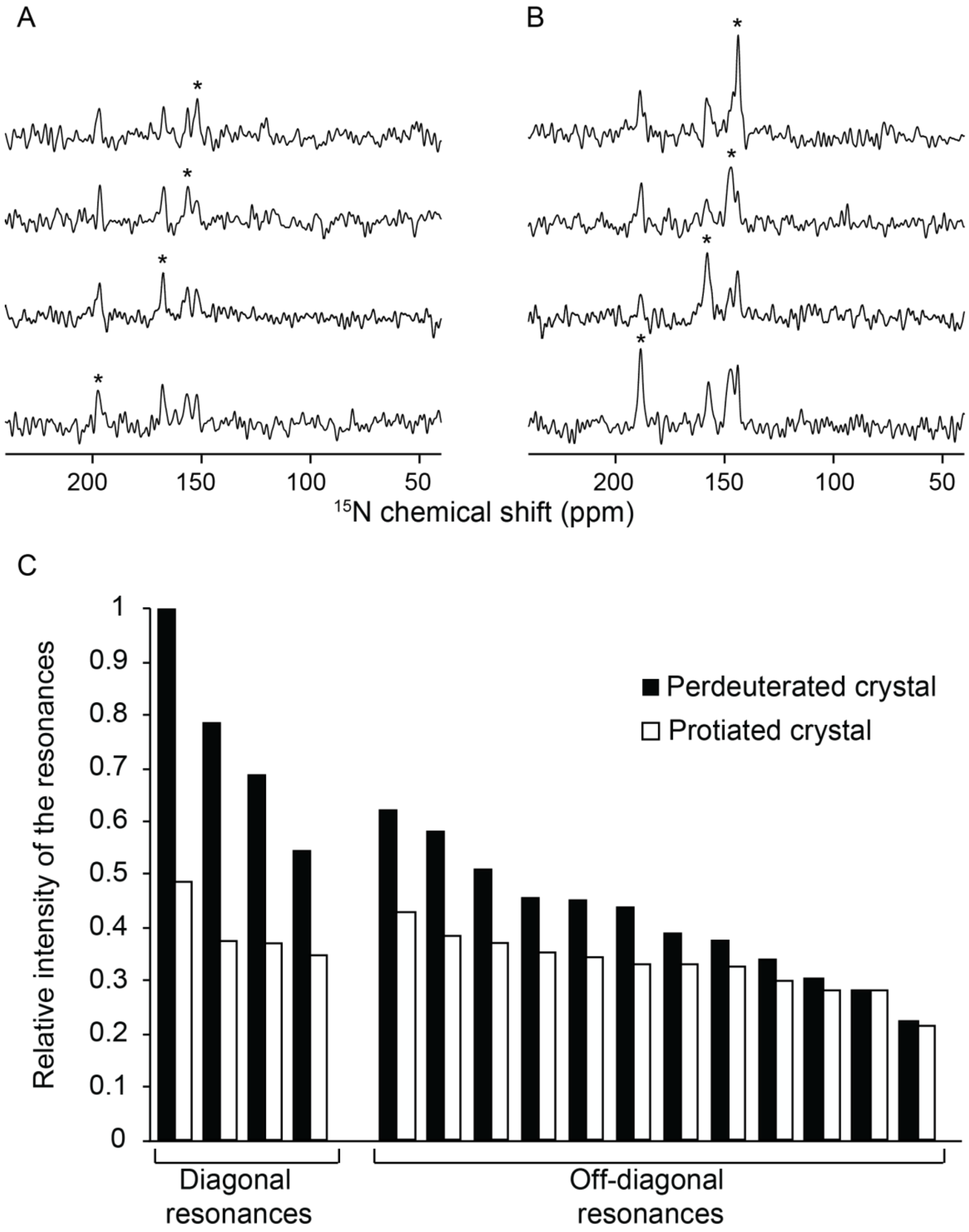

Figure 2.13. One-dimensional slices through each diagonal peak from the two-dimensional Mismatched Hartmann-Hahn (MMHH) experiments (Figure12) for the protiated (A) and perdeuterated (B) NAL crystals. Asterisks indicate the position of the diagonal peaks. (C) Relative experimental intensity of the on- and off-diagonal resonances ranked in high to low order are shown from left to right. Black columns represents the values in the perdeuterated crystal, and white columns represents the values for the protiated crystal. Normalization was performed based on the largest intensity value across the two spectra.

2.4 Discussion

Deuteration affects the spectroscopic properties of nearby signals, although there is minimal chemical perturbation from the additional neutron in deuterons compared to protons. The specific goal of these experimental studies is to explore the use of deuteration to selectively improve the resolution and sensitivity of multidimensional solid-state NMR experiments on stationary samples, such as single crystals and uniaxially aligned proteins. To understand the effects of deuteration, comparisons were made between similarly prepared protiated and perdeuterated samples. In the spectra for the protiated NAL single crystal, acquired with ^{1}H decoupling, ~140 Hz ^{15}N resonance line-widths were observed. In the spectra for the perdeuterated NAL single crystal, ~140 Hz ^{15}N resonance line-widths were only observed when both ^{1}H and ^{2}H decoupling was applied. Because ^{2}H has a different NMR frequency than ^{1}H, their presence on proximate carbon sites requires a separate RF channel for decoupling. This is why two ^{1}H, ^{2}H, ^{15}N triple-resonance NMR probes were built for the experiments of the perdeuterated NMR samples.

Irradiation at the ^{2}H resonance frequency causes rapid transitions between the ^{2}H nuclear spin states. When the irradiation power is strong enough, spins are decoupled from one another. Due to the large ^{2}H quadrupole splittings, very high-power irradiation would be required for single-quantum decoupling. Importantly, it has been shown that spin S=1 ^{2}H nuclei at magnetic field strengths less than the amplitudes of the quadrupole couplings can be decoupled through a double quantum process [8, 35].

When the ^{2}H quadrupole splitting for the C$_\alpha$ deuterons is on the order of 180 kHz and the ^{2}H-^{15}N dipolar splitting is on the order of 250 Hz, the decoupling field strength required for double quantum decoupling is only on the order of $(QD)^{1/2}$ compared to Q for single quantum decoupling [8], where Q is the quadrupole coupling constant and D is the dipolar coupling constant. Given the orders of magnitude differences between Q and D, the required field strength is then lowered from orders of hundreds of kHz to orders of tens of kHz. This is in agreement with experimental findings when SPINAL-16 is used to minimize the effects of frequency offsets due to chemical shielding where the decoupling power required is less than 50 kHz for the rigid crystal sample and much less for motional averaged protein samples.

Signals from different crystals of the same compound can have different line-widths due to a variety of factors such as crystal packing. Small differences in line-widths could be attributed to such effects. [36] In addition, anisotropic chemical shifts measured in experiments depend on the crystal orientation, which can be adjusted by rotating the crystal within the sample coil. This is why frequencies of the resonances are different in many of the spectra of the single crystal samples. Magnetically oriented Pf1 coat proteins in lipid bilayers, by comparison, can self-orient to the same orientations [37]. Comparisons among different protein samples are simpler, because their spectra have matching resonance frequencies.

Whether the ^{15}N resonance line-widths or the power requirements for decoupling the protiated and perdeuterated samples are compared, the results are similar. This is the case for both the NAL single crystal sample and the magnetically aligned Pf1 coat protein sample. This result suggests that carbon site perdeuteration alone is not sufficient to further reduce ^{15}N line-widths in peptide samples. Effects of ^{1}H dilution were observed in SLF experiments for both the perdeuterated NAL crystal and the perdeuterated oriented membrane protein sample. The dipolar coupling frequency line-widths in both samples are much reduced in the absence of ^{1}H-^{1}H homonuclear decoupling during t_1. Based on the differences in line-widths between the protiated (2.2 kHz) and perdeuterated NAL crystals (0.85 kHz), SLF experiments show that the contribution of line-widths from the ^{1}H on carbon sites is approximately 1.35 kHz. Here perdeuteration can be applied where the use of high-power irradiation is limited by instrumentation or sample heating. In contrast, in experiments where the ^{1}H-^{1}H homonuclear dipolar couplings are attenuated, such as with SAMPI4, line-narrowing was not observed in the perdeuterated samples. The absence of further line-narrowing by homonuclear decoupling on the perdeuterated samples suggests that the homonuclear decoupling and perdeuteration operate on the same line broadening mechanisms and their effects are not additive.

Resonances in the HETCOR spectra shown in Figure 2.10A and B are tilted in appearance for the NAL single crystal samples, this was previously observed by Lu *et. al.* (2012). The explanation for the observation of the tilted resonances, however, is beyond the scope of this paper.

Remarkably, the results of passive homonuclear spin-exchange experiments are not altered by the presence of high levels of deuteration on single crystal samples. This suggests that the mechanism of homonuclear spin-exchange does not require the presence of strong and abundant ^{1}H-^{1}H dipolar couplings. In each protiated NAL molecule, there are thirteen ^{1}H bonded to carbons, one bonded to nitrogen, and one bonded to oxygen; in the “perdeuterated” case, there are no ^{1}H bonded to carbon, one bonded to nitrogen, and one bonded to oxygen. Thus, in the crystalline samples, the presence of ^{1}H is reduced from 100% to 13% by synthesis of the perdeuterated samples. If the dominant mechanism of spin-exchange is through the "abundant" ^{1}H spin bath, then different spin-exchange dynamics would be expected in highly deuterated samples. We have no evidence that this is the case. One explanation for the lack of difference might be that dilute spin-exchange is playing a role here. The possibilities of the dominant role of dilute spin-exchange mechanism was demonstrated previously in unenriched organic solids [38]. In contrast, a proton relay mechanism, such as that proposed for the MMHH experiment only requires two nearby ^{1}H for each ^{15}N spin pair and is not directly affected by “perdeuteration” of many carbon sites. Dilute spin-exchange works well on samples of perdeuterated NAL with as little as 5% Hartmann-Hahn mis-match. By contrast, protiated NAL requires at least 10%-15% Hartmann-Hahn mis-match to give measurable on- and off-diagonal resonances. This is because in the perdeuterated NAL crystal, there are fewer ^{1}H available to drain the ^{15}N magnetization during the MMHH mixing period. As a result, the experiments yield stronger signals. In addition, because MMHH works well at lower levels of Hartmann-Hahn mis-match on the perdeuterated NAL single crystal, the mixing is more efficient which results in stronger off-diagonal signals. In this case, even though the perdeuterated crystal is 25% smaller in size, acquisition of the same number of scans results in stronger or equal intensity on and off-diagonal signals.

2.5 Conclusions

Perdeuteration isolates ^{1}H nuclei in organic and biochemical molecules. It reduces most of the effects of the ^{1}H-^{1}H spin network on individual resonances and it prolongs the ^{1}H-^{15}N heteronuclear dipolar coupling evolution in SLF experiments. However, perdeuteration is not as effective as ^{1}H-^{1}H homonuclear decoupling in oriented sample solid-state NMR. This is because the ^{1}H back-exchange step leaves proximate ^{1}H nuclei, which still require substantial ^{1}H-^{1}H homonuclear decoupling. In addition, sensitivity enhancement due to deuteration was observed in the spin-diffusion experiments that utilized the mis-match Hartmann-Hahn mechanism.

2.6 Acknowledgements

We thank Dr. Chin Wu for assistance with the NMR instrumentation and Dr. Ratan Rai for helpful discussions. This research was supported by grants P41EB002031 and R35GM122501 from the National Institutes of Health and utilized the Biomedical Technology Resource Center for NMR Molecular Imaging of Proteins at the University of California, San Diego.

Chapter 2, in full, is a reprint of the material as it appears in: Long, Z, Park, SH, Opella SJ, (in press), Effects of deuteration on solid-state NMR spectra of single peptide crystals and oriented protein samples, *JMR,* (2019). The dissertation author is the primary researcher and author on the paper.

2.7 **References**

[1] H.L. Crespi, Rosenber.Rm, J.J. Katz, Proton Magnetic Resonance of Proteins Fully Deuterated except for 1h-Leucine Side Chains, Science, 161 (1968) 796.

[2] J.L. Markley, I. Putter, O. Jardetzky, High-Resolution Nuclear Magnetic Resonance Spectra of Selectively Deuterated Staphylococcal Nuclease, Science, 161 (1968) 1249-51.

[3] A.E. Mcdermott, F.J. Creuzet, A.C. Kolbert, R.G. Griffin, High-Resolution Magic-Angle-Spinning Nmr-Spectra of Protons in Deuterated Solids, Journal of Magnetic Resonance, 98 (1992) 408-413.

[4] C.R. Morcombe, E.K. Paulson, V. Gaponenko, R.A. Byrd, K.W. Zilm, H-1-N-15 correlation spectroscopy of nanocrystalline proteins, J Biomol Nmr, 31 (2005) 217-230.

[5] B. Reif, C.P. Jaroniec, C.M. Rienstra, M. Hohwy, R.G. Griffin, H-1-H-1 MAS correlation spectroscopy and distance measurements in a deuterated peptide, Journal of Magnetic Resonance, 151 (2001) 320-327.

[6] R.C. Hewitt, S. Meiboom, L.C. Snyder, Proton Nmr in Nematic Liquid Crystalline Solvents - Use of Deuterium Decoupling, J Chem Phys, 58 (1973) 5089-5095.

[7] L.C. Snyder, S. Meiboom, Theory of Proton Nmr with Deuteron Decoupling in Nematic Liquid Crystalline Solvents, J Chem Phys, 58 (1973) 5096-5103.

[8] A. Pines, D.J. Ruben, S. Vega, M. Mehring, New Approach to High-Resolution Proton Nmr in Solids - Deuterium Spin Decoupling by Multiple-Quantum Transitions, Phys Rev Lett, 36 (1976) 110-113.

[9] W.I. Goldburg, M. Lee, Nuclear Magnetic Resonance Line Narrowing by a Rotating rf Field, Phys Rev Lett, 11 (1963) 255-258.

[10] A. Bielecki, A.C. Kolbert, H.J.M. De Groot, R.G. Griffin, M.H. Levitt, Frequency-Switched Lee—Goldburg Sequences in Solids, in: W.S. Warren (Ed.) Advances in Magnetic and Optical Resonance, Academic Press, 1990, pp. 111-124.

[11] J.S. Waugh, L.M. Huber, U. Haeberlen, Approach to High-Resolution Nmr in Solids, Phys Rev Lett, 20 (1968) 180.

[12] A. Pines, W. Rhim, J.S. Waugh, Homogeneous and Inhomogeneous Nuclear Spin Echoes in Solids, Journal of Magnetic Resonance, 6 (1972) 457.

[13] R.K. Hester, J.L. Ackerman, B.L. Neff, J.S. Waugh, Separated Local Field Spectra in Nmr - Determination of Structure of Solids, Phys Rev Lett, 36 (1976) 1081-1083.

[14] J.S. Waugh, Uncoupling of Local Field Spectra in Nuclear Magnetic-Resonance - Determination of Atomic Positions in Solids, P Natl Acad Sci USA, 73 (1976) 1394-1397.

[15] C.H. Wu, A. Ramamoorthy, S.J. Opella, High-Resolution Heteronuclear Dipolar Solid-State Nmr-Spectroscopy, J Magn Reson Ser A, 109 (1994) 270-272.

[16] A.A. Nevzorov, S.J. Opella, A "Magic Sandwich" pulse sequence with reduced offset dependence for high-resolution separated local field spectroscopy, J Magn Reson, 164 (2003) 182-186.

[17] A.A. Nevzorov, S.J. Opella, Selective averaging for high-resolution solid-state NMR spectroscopy of aligned samples, J Magn Reson, 185 (2007) 59-70.

[18] S.H. Park, F.M. Marassi, D. Black, S.J. Opella, Structure and Dynamics of the Membrane-Bound Form of Pf1 Coat Protein: Implications of Structural Rearrangement for Virus Assembly, Biophys J, 99 (2010) 1465-1474.

[19] S.H. Park, S.J. Opella, Triton X-100 as the "Short-Chain Lipid" Improves the Magnetic Alignment and Stability of Membrane Proteins in Phosphatidylcholine Bilayers for Oriented-Sample Solid-State NMR Spectroscopy, J Am Chem Soc, 132 (2010) 12552-12553.

[20] N. Bloembergen, On the Interaction of Nuclear Spins in a Crystalline Lattice, Physica, 15 (1949) 386-426.

[21] D. Suter, R.R. Ernst, Spin Diffusion in Resolved Solid-State Nmr-Spectra, Phys Rev B, 32 (1985) 5608-5627.

[22] N.M. Szeverenyi, M.J. Sullivan, G.E. Maciel, Observation of Spin Exchange by Two-Dimensional Fourier-Transform C-13 Cross Polarization-Magic-Angle Spinning, J Magn Reson, 47 (1982) 462-475.

[23] A.A. Nevzorov, Mismatched Hartmann-Hahn conditions cause proton-mediated intermolecular magnetization transfer between dilute low-spin nuclei in NMR of static solids, J Am Chem Soc, 130 (2008) 11282-11283.

[24] G.J. Lu, S.J. Opella, Mechanism of dilute-spin-exchange in solid-state NMR, J Chem Phys, 140 (2014).

[25] P.J. Carroll, P.L. Stewart, S.J. Opella, Structures of two model peptides: N-acetyl-d,l-valine and N-acetyl-l-valyl-l-leucine, Acta Crystallographica Section C, 46 (1990) 243-246.

[26] D.S. Thiriot, A.A. Nevzorov, L. Zagyanskiy, C.H. Wu, S.J. Opella, Structure of the coat protein in Pf1 bacteriophage determined by solid-state NMR spectroscopy, J Mol Biol, 341 (2004) 869-879.

[27] S.H. Park, C. Yang, S.J. Opella, L.J. Mueller, Resolution and measurement of heteronuclear dipolar couplings of a noncrystalline protein immobilized in a biological supramolecular assembly by proton-detected MAS solid-state NMR spectroscopy, J Magn Reson, 237 (2013) 164-168.

[28] R.A. Schiksnis, M.J. Bogusky, P. Tsang, S.J. Opella, Structure and dynamics of the Pf1 filamentous bacteriophage coat protein in micelles, Biochemistry, 26 (1987) 1373-1381.

[29] S.A. McNeill, P.L. Gor'kov, K. Shetty, W.W. Brey, J.R. Long, A low-E magic angle spinning probe for biological solid state NMR at 750 MHz, J Magn Reson, 197 (2009) 135-144.

[30] N. Sinha, C.V. Grant, C.H. Wu, A.A. De Angelis, S.C. Howell, S.J. Opella, SPINAL modulated decoupling in high field double- and triple-resonance solid-state NMR experiments on stationary samples, J Magn Reson, 177 (2005) 197-202.

[31] G.J. Lu, S.H. Park, S.J. Opella, Improved 1H amide resonance line narrowing in oriented sample solid-state NMR of membrane proteins in phospholipid bilayers, J Magn Reson, 220 (2012) 54-61.

[32] F. Delaglio, S. Grzesiek, G.W. Vuister, G. Zhu, J. Pfeifer, A. Bax, NMRPipe: a multidimensional spectral processing system based on UNIX pipes, J Biomol NMR, 6 (1995) 277-293.

[33] L.A. Colnago, K.G. Valentine, S.J. Opella, Dynamics of Fd-Coat Protein in the Bacteriophage, Biochemistry-Us, 26 (1987) 847-854.

[34] A.L. Rheingold, CCDC 624793: Experimental Crystal Structure Determination, (2014).

[35] A. Pines, S. Vega, M. Mehring, Nmr Double-Quantum Spin Decoupling in Solids, Phys Rev B, 18 (1978) 112-125.

[36] R.H. Prigl, U., The Theoretical and Practical Limits of Resolution in Multiple-Pulse High-Resolution NMR of Solids, Academic Press, San Diego, 1990.

[37] S.H. Park, A.A. Mrse, A.A. Nevzorov, A.A. De Angelis, S.J. Opella, Rotational diffusion of membrane proteins in aligned phospholipid bilayers by solid-state NMR spectroscopy, J Magn Reson, 178 (2006) 162-165.

[38] J. Virlet, D. Ghesquieres, NMR longitudinal cross relaxation induced by natural abundance ^{13}C-^{13}C dipolar interaction in organic solids. Hexamethylethane, Chem Phys Lett, 73 (1980) 323-327.

Chapter 3: ^{1}H detection of ^{1}H-^{15}N heteronuclear dipolar oscillations improves the sensitivity of oriented sample (OS) solid-state NMR

3.1 Introduction

Indirect ^{1}H detection is widely used in nuclear magnetic resonance (NMR) spectroscopy [1-4]. It was first applied in double-resonance solid-state NMR experiments on organic solids [5], and then in solution NMR [6, 7]. Later it was applied to magic angle spinning (MAS) solid-state NMR experiments [8], especially those performed at ultra-fast MAS spinning speeds [9]. In all three cases, static solid-state NMR, solution NMR, and MAS solid-state NMR, sensitivity enhancement was observed in ^{1}H-detected compared to direct-detected experiments only because reasonable ^{1}H chemical shift line-widths could be obtained [8].

For ^{1}H detection experiments, solvent signal suppression is often needed, in particular for samples of biopolymers such as proteins in aqueous solutions. Consequently, many methods have been designed tlhat selectively inhibit the strong ^{1}H signals from water. One of the most widely implemented method is presaturation [10]. Compared to other methods, which use pulse field gradients (PFG) [11, 12], presaturation is relatively easy to implement, but potentially suffers from adverse effects such as saturation of signals from exchangeable ^{1}H as well as reduction of intensities of signals near the ^{1}H water resonance frequency. However, application of PFG requires additional hardware and more complex pulse sequences.

At the same time, in oriented sample solid-state NMR, the effects of the strong ^{1}H-^{1}H homonuclear dipole-dipole interactions result in large ^{1}H line-widths in the chemical shift dimension [13]. Direct detection of the ^{1}H signals requires both heteronuclear decoupling and homonuclear decoupling during signal acquisition which cannot be achieved with conventional continuous acquisition methods of the free induction decay. This is another reason why ^{1}H detection has not seen many applications in oriented sample solid-state NMR.

Windowed detection is an essential aspect of the acquisition of ^{1}H signals. This results in sensitivity enhancement that can be achieved in stationary solid samples such as amorphous proteins [14]. However, the need for resolution among ^{1}H chemical shift frequencies in complex protein spectra limits the wider use of these techniques. Even at high fields, the spans of the ^{1}H chemical shift frequencies are small compared to the resonance line-widths. For example, the ^{1}H line-widths of resonances from partially motionally-averaged residues can be improved to less than 4 ppm in a span of 12 ppm [13]. The less than ideal resolution results in many overlapping signals in one-dimensional spectra of medium and large size proteins. In comparison, the ^{1}H-^{15}N heteronuclear dipolar coupling frequency has a larger span of 10 kHz and relatively smaller resonance line-widths that can be equal to or less than 200 Hz [15]. Therefore, detection of the ^{1}H-^{15}N dipolar coupling frequencies from the amide N-H groups on the protein backbone can provide much better spectral resolution than the detection of the ^{1}H chemical shift frequencies.

Polarization inversion spin-exchange modulated observation (PISEMO) spectroscopy was developed to supplement the more widely applied polarization spin-exchange at the magic angle (PISEMA) experiments [16] with the addition of windowed-detection of ^{1}H signals by directly detecting the oscillating ^{1}H-^{15}N heteronuclear dipolar coupling frequencies [17]. During the PISEMO experiment the ^{1}H channel uses a semi-windowless WaHuHa pulse sequence to attenuate the ^{1}H-^{1}H dipolar interactions. At the same time the matched ^{15}N channel induces polarization inversion through spin-exchange under the influence of the heteronuclear dipolar couplings. This allows the ^{1}H detected PISEMO experiment to directly measure the heteronuclear coupling frequencies in the form of the modulated ^{1}H intensities.

To obtain greater efficiency of the ^{1}H channel with lossy biological samples, strip shields are often employed to enhance the efficiency of solenoid coils. It was found that when strip shields are incorporated inside the coils, they retain the quality factor (Q) of the high frequency ^{1}H channel for the solenoid coils when a lossy sample is place in the coil, without significant attenuation on the Q for the low frequency ^{15}N channel [18]. The application of this coil configuration retains the high filling factors of the ^{1}H channel compared to the cross-coil designs which typically use a orthogonal coil such as the modified Alderman-Grant coil [19] or loop gap resonator [20] for the ^{1}H channel that are larger in size. This probe configuration was chosen to deliver balanced performances for both ^{1}H and ^{15}N detection as well as RF homogeneity [21]. Here we improve the PISEMO experiment for use in hydrated samples by adding a saturation pulse after cross-polarization and before the multiple pulse sequence on the ^{1}H channel. The model system is a N-acetyl leucine (NAL) single crystal submerged in water, which allows for testing of the solvent suppression methods during the development of the biological sample version of the ^{1}H detected PISEMO pulse sequence. Pf1 coat protein in the filamentous phage particles is chosen as the benchmark protein for ^{1}H detection studies because of its robust stability and facile magnetic alignment properties [22] which greatly facilitate experimental optimization. The findings obtained with the relatively simple protein sample can be readily applied to more complex proteins using the oriented sample solid-state methods.

3.2 Experimental Methods

Experiments were performed using a probe with a single solenoid coil triple-tuned to the ^{1}H, ^{2}H, and ^{15}N resonance frequencies [23]. A strip shield [18] consisting of 6 copper strips (0.8 mm wide, 12 mm long, and 0.05 mm thick) separated by 0.8 mm gaps) on Teflon (0.03mm thick) sheets was inserted inside a 3.2 mm ID solenoid coil.

The quality factor (Q) of the probe was measured using a network analyzer. The effects of placing the strip shield inside the double-tuned solenoid coil are summarized in Table 3.1; the Qs of both the ^{1}H and ^{15}N channels were reduced by ~15% on a single crystal sample. The Q of the ^{15}N channel with Pf1 bacteriophage and protein-containing bicelle samples was also reduced by ~15%. Notably, it increased the ^{1}H Q of lossy samples, e.g. the phage sample (~36% increase) and the bicelle sample (~60% increase). This shows that the strip shield plays an essential role in obtaining high sensitivity spectra with ^{1}H detection methods in solid-state NMR.

Table 3.1. Quality factor of the probe's RF channels in the absence and presence of a strip shield.

	^{1}H Channel (olenoid)	**^{15}N Channel (solenoid)**	**^{1}H Channel (with strip shield)**	**^{15}N Channel (with strip shield)**
Crystal	186	59	155	50
Pf1 Phage	110	60	150	50
Triton Bicelle	86	57	138	50

The N-acetyl leucine (NAL) crystal was prepared as described previously [23]. Then 20 µL of water was added to a 4 mg ^{15}N labeled NAL crystal in a 3 mm OD flat bottom glass tube (newera-spectro.com). The bulk of the crystal is resistant to dissolution during room temperature experiments. It was sealed with a 3 mm OD rubber cap and silicone glue. The sample arrangement is illustrated in Figure 3.1.

Pf1 phage was grown as previously described [22], and then pelleted by centrifugation for four hours at 50k rpm. The pellet was resuspended to a final protein concentration of 50 mg/mL in 20 mM pH 8 sodium borate buffer. 50 µL of the sample was placed in a 3 mm x 10 mm glass sample tube (newera-spectro.com), sealed with a rubber cap and subsequently with silicone glue to prevent evaporation.

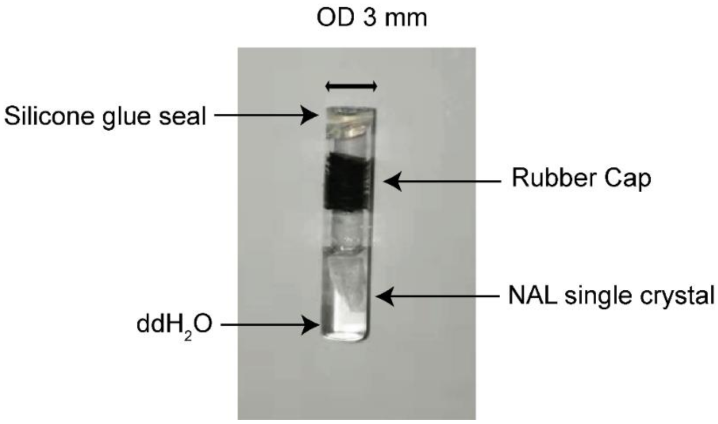

Figure 3.1. Picture of the water submerged single crystal sample placed in a 3 mm OD flat bottom NMR tube, capped with a piece of black rubber, and sealed with silicone glue to prevent losing of liquid due to evaporation.

The NMR experiments were performed on a spectrometer with a 700 MHz ^{1}H frequency. The spectra of the NAL crystal submerged in water were acquired with power level of 55 kHz, and the spectra for the Pf1 coat protein were acquired with a power level of 70 kHz. The timing diagrams for the pulse sequences are shown in Figure 3.2. We have previously described the use of both direct and indirect- detected versions of PISEMO NMR experiments without solvent suppression [17]. ^{15}N-detected PISEMO and ^{1}H-detected PISEMO are illustrated in Figure 3.2A and 3.2B, respectively. In applications of ^{1}H-detected PISEMO to the NAL crystal in water, the experimental parameters were: 2 scans, 128 t_1 points, and 4 sec z-filter. The large signal from the solvent (water) was suppressed by applying continuous wave irradiation of 7 kHz magnitude at the precise resonance frequency of the ^{1}H water during the z-filter interval. The X, Y, X, Y-phased saturation pulses were applied in the ^{1}H-detected PISEMO. The four 1-sec pulses utilized 10 kHz B_1. The ^{15}N detected PISEMO spectra were acquired with 55 kHz power, 4 scans and 256 t_1 points. The ^{1}H detected PISEMO spectra were acquired with 55 kHz irradiation, 2 scans and 512 t_1 points. Spectra of solvent-free crystals were acquired with 4 scans, and 256 t_1 points at 53 kHz power levels. Each of the X, Y, X, Y-phase saturation pulse used were 0.2 sec long to match the pulse length used in the protein experiments. The power levels were either 12 kHz or 0 kHz in order to determine whether there is any signal attenuation due to the saturation irradiation. NMR spectra for crystal samples were acquired at room temperature.

^{15}N-detected PISEMO spectra of the bacteriophage were acquired with 64 scans and 128 t_1 points (1.73 msec scaled acquisition time). The ^{1}H-detected PISEMO spectra of Pf1 bacteriophage were acquired with 32 scans and 256 t_1 points (5.12 msec). These spectral parameters enabled both dimensions of the spectra to have the same acquisition times. In the ^{1}H-detected experiment, a total of four 12.5 kHz 0.2 sec long pulses with phases X, Y, X, Y were used. NMR spectra for Pf1 phage coat protein were acquired at 0°C.

Data processing was performed using the program Topspin 3.1 (www.bruker.com) with the python module. Data points were taken from the selected detection windows. The data were phase shifted to maximize the signal intensity of the real data, then real data points were selected from the distorted points in the beginning and end of the detection window, and subsequently compiled into a complete data set. The data points from the same detection window were summed. In the presented experimental data, samples were taken at 0.05 µsec intervals. In each detection window, 1.4 µsec of data was extracted, which corresponds to 28 complex points, of which 14 are real points. Imaginary points were discarded. Squared sine bell functions were applied to process the protein data: in the two-dimensional experimental data, 45° shift for chemical shift dimension, 60° shift for dipolar coupling frequency dimension to present spectra with better peak shapes. No shaped function or line-broadening functions were applied to the shown one-dimensional spectral slices to preserve the veracity of the intensities used to compare sensitivities. Resonance assignments were based on previously published results [22].

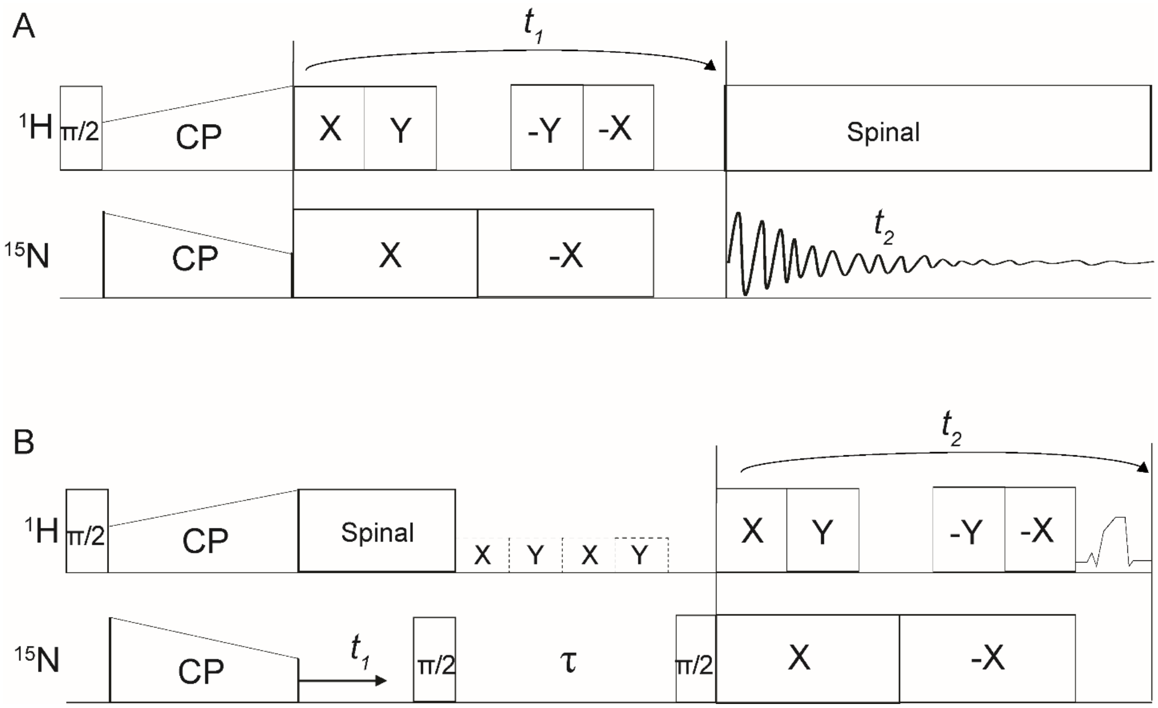

Figure 3.2. Timing diagrams for the pulse sequences used in the ^{1}H- and ^{15}N- detected PISEMO experiments. (A) ^{15}N-detected PISEMO. (B) ^{1}H-detected PISEMO. Dashed boxes indicate the saturation pulses during z-filter which are applied to protein samples. The pulses consist of 4 blocks of 0.2 s 13 kHz pulses with the phase X, Y, X, Y. (A-B) cross polarization utilizes double ramps with 60-100% ramp on the ^{1}H channel and 100-60% ramp on the ^{15}N channel both have a duration of 1 ms. During the multiple pulse cycles, the 4 pulses on the ^{1}H channel has phases in the order of X, Y, -Y, –X for the odd number of cycles, and –X, -Y, Y, X for the even number of cycles. The two pulses on the ^{15}N channel have phase X, and -X for odd number of cycles, and –X, and X for even number of cycles.

3.3 Results and Discussion

Each of the four molecules of NAL in a single crystal have a distinct orientation within the unit cell. Consequently, a solid-state NMR spectrum of a NAL single crystal has four signals, each of which is characterized by a unique frequency along the axis associated with an operative nuclear spin interaction. Here the frequencies reflect the angular dependence of the ^{15}N chemical shift and ^{1}H-^{15}N heteronuclear dipole-dipole couplings. This accounts for the resolution among signals in the spectra presented in Figures 3.2 and 3.3. As a result, differences of crystal orientations produces different resonance frequencies in the one- and two-dimensional spectra.

The ^{15}N chemical shift and ^{1}H-^{15}N dipolar coupling frequencies are readily observed for each amide site in two-dimensional separated local field (SLF) spectra of single crystals of uniformly ^{15}N enriched NAL. High resolution results from the implementation of WHH-4 for homonuclear decoupling. Here we are particularly interested in the ^{1}H-detected version of PISEMO. Since the ultimate goal is to perform ^{1}H detected PISEMO on proteins in aqueous solution it is necessary to add water suppression to the pulse sequences.

In ^{1}H detected PISEMO experiments the ^{1}H - ^{15}N heteronuclear dipolar coupling frequencies are observed directly. Most solvent molecules and phospholipids do not have abundant or ^{15}N-^{1}H bonds. In addition, because ^{1}H chemical shift frequencies are not directly measured solvent signals, in theory, would not interfere with protein signals, however, residual solvent signals is still strong and have to be dealt with to obtain sensitive protein signal. Noise from solvent signals is not completely randomized, this is seen between ± 4 kHz in Figure 3.3A with a NAL single crystal sample submerged in water. Because the spectrum in Figure 3.3A was collected without solvent suppression, the signal and noise have similar intensities as manifested in their having similar contour levels.

Application of low power continuous wave (CW) irradiation during the z-filter interval greatly reduces the unwanted noise. This is illustrated with the experimental data shown in Figure 3.3B. Comparing the resonances in the contour plot in Figure 3.3A to those in Figure 3.3B, enables the signals from the NAL single crystal to be readily distinguished from the noise in Figure 3.3A. Comparison of the one-dimensional slices in Figure 3.3C and 3.3D show that sensitivity is enhanced many folds with water suppression.

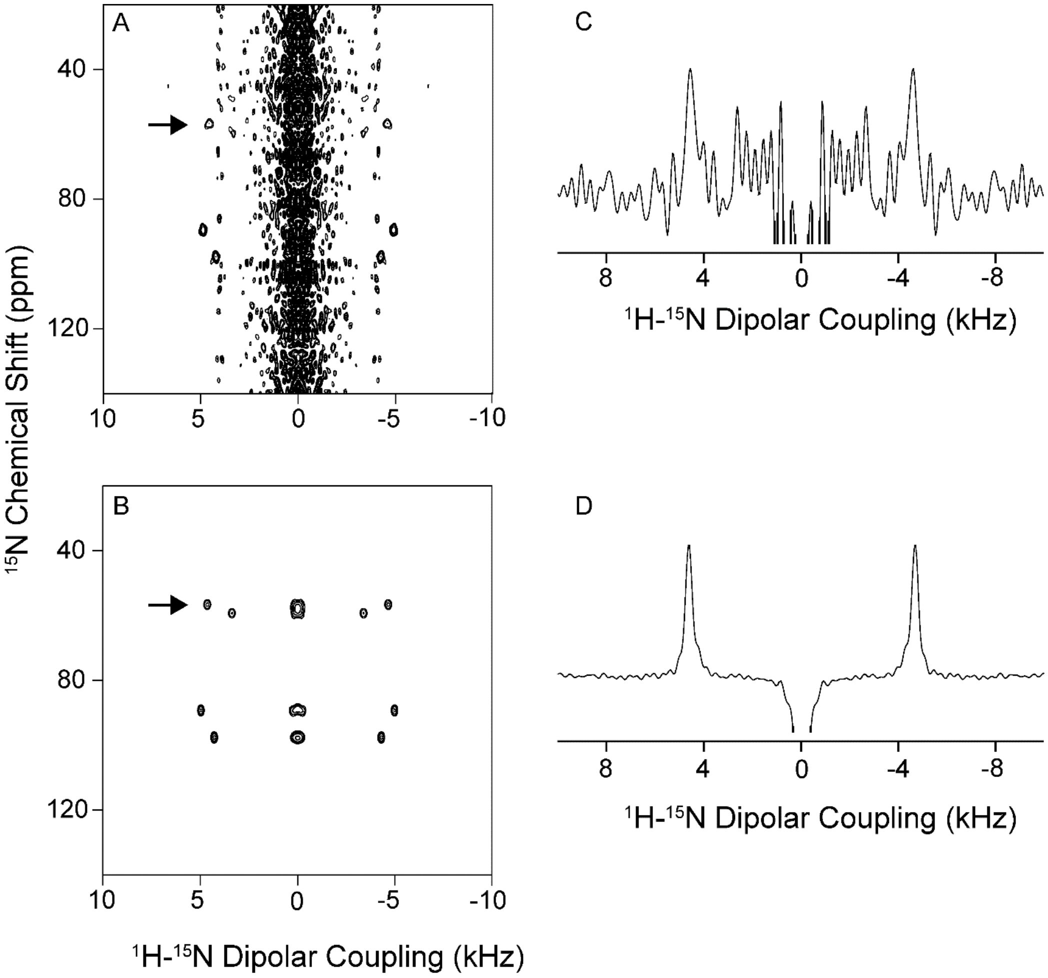

Figure 3.3. A ^{15}N labeled NAL crystal submerged in pure water was used to demonstrate the water saturation method during the z-filter to suppress signals from water ^{1}H. Spectra were acquired with 2 scans, 128 t_1 points at 55 kHz. (A) and (B) are the two-dimensional ^{1}H detected PISEMO spectra shown with the full dipolar coupling frequency domain. (A) uses a 4 sec delay during z-filter. (B) uses a 7 kHz continuous wave saturation pulse with a single phase x during the 4 sec z-filter. (C) and (D) are one-dimensional slices through the arrow in (A) and (B) respectively.

In Figure 3.3B, a 4 sec saturation pulse was required to sufficiently suppress the water signals using 6 kHz power, compared to Figure 3.3A where the 4 sec pulse was replaced with a 4 sec delay. In addition to the CW method, application of the 90º phase shifts during the saturation pulse was attempted. This phase shift was developed to destroy unrelated ^{1}H t_1 noise [24]. It is shown in Figure 3.4 that the 4 phase-shifted pulses can replace the CW saturation pulse for the water submerged crystal sample. The saturation duration used was 4 sec in total, at 10 kHz power level, the duration and the power level used in this experiment was not minimized. In this experiment, a signal-to-noise ratio enhancement of two-fold was obtained when compared to the ^{15}N detected spectrum, as shown in comparisons of the signal/noise levels of the slices in Figure 3.4C and 3.4D versus Figure 3.4E and 3.4F. Indifferent to crystal samples, seconds-long durations during the saturation pulses cannot be used on proteins because protein samples often have high levels of motions, which greatly reduce the T_1 of protein samples. This renders the CW method unfavorable for the application to proteins, since it requires seconds long saturation time.

When four phase-shifted pulses are applied during the time interval the z-filter of the PISEMO experiment, the time required for saturation of the magnetization can be reduced, shortening the overall experimental time. For example, for the Pf1 coat protein sample, the z-filter interval can be as short as 0.8 sec. This is significant for the application of the method to protein samples, where the amide ^{15}N T_1 is on the order of 10 sec. To demonstrate that saturation during the z-filter does not affect the NMR signals, the ^{1}H detected PISEMO experiment was performed on a dry NAL single crystal with or without the saturation pulses. The results are shown in Figure 3.5 where comparison of Figure

3.5A (with) and 3.5B (without) the application of the saturation pulse yield nearly identical spectra. The intensities of the resonance signals in the spectral slices shown in Figure 3.5C and 3.5D are very similar at the same noise level. It may be possible to further improve solvent suppression by taking advantage of the homospoil z-gradient incorporated into the MAS experiment MISSISSIPI [25] or a gradient coil with available accessories. Sufficient suppression of large solvent signals results in the ^{1}H detected PISEMO spectrum of Pf1 coat protein shown in Figure 3.6B.

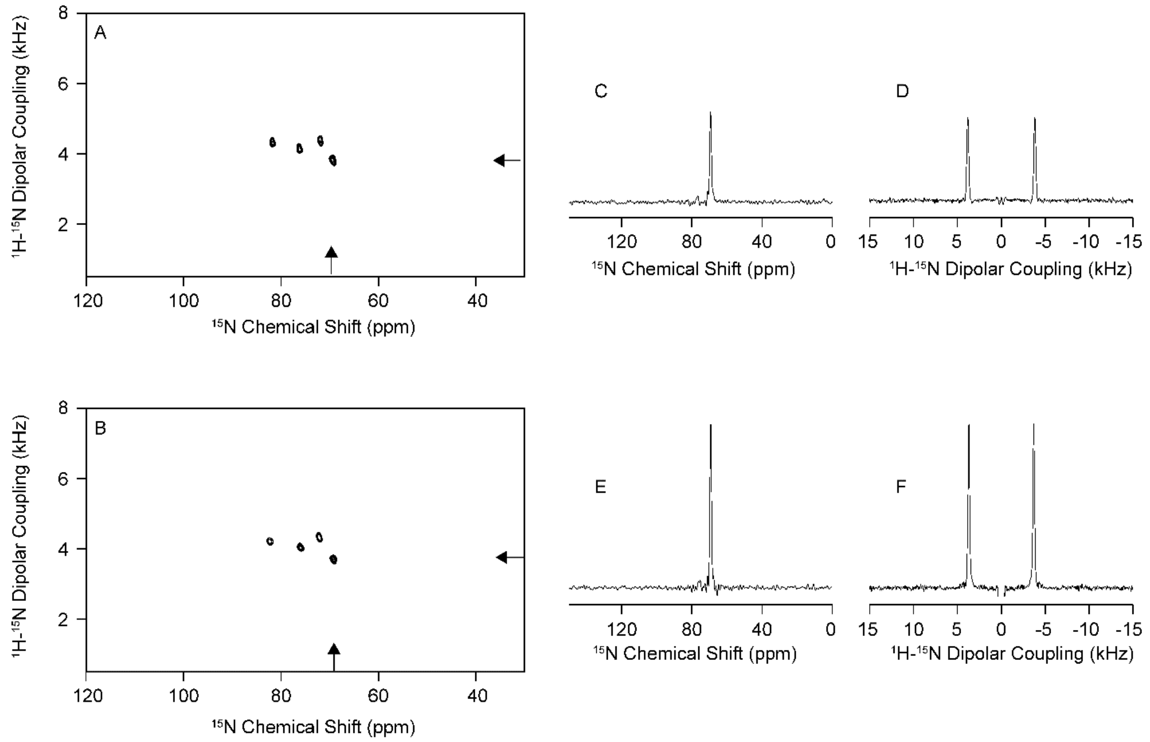

Figure 3.4. A ^{15}N labeled NAL crystal submerged in pure water was used to demonstrate the water saturation method during the z-filter to suppress signals from water ^{1}H. (A) is the ^{15}N detected PISEMO spectrum acquired with 4 scans and 256 t_1 points at 55 kHz .(B) is the ^{1}H detected PISEMO spectrum acquired with 2 scans, 512 t_1 points at 55 kHz. Four 10 kHz 1 sec long water suppression pulses of phases X,Y,X,Y were applied during the 4 sec z-filter. (C) and (E) are ^{15}N chemical shift dimension slices through the arrow in (A) and (B) respectively. (D) and (F) are ^{1}H-^{15}N dipolar coupling frequency dimension slices through the arrow in (A) and (B) respectively. The arrows points to the frequency where the slices are taken.

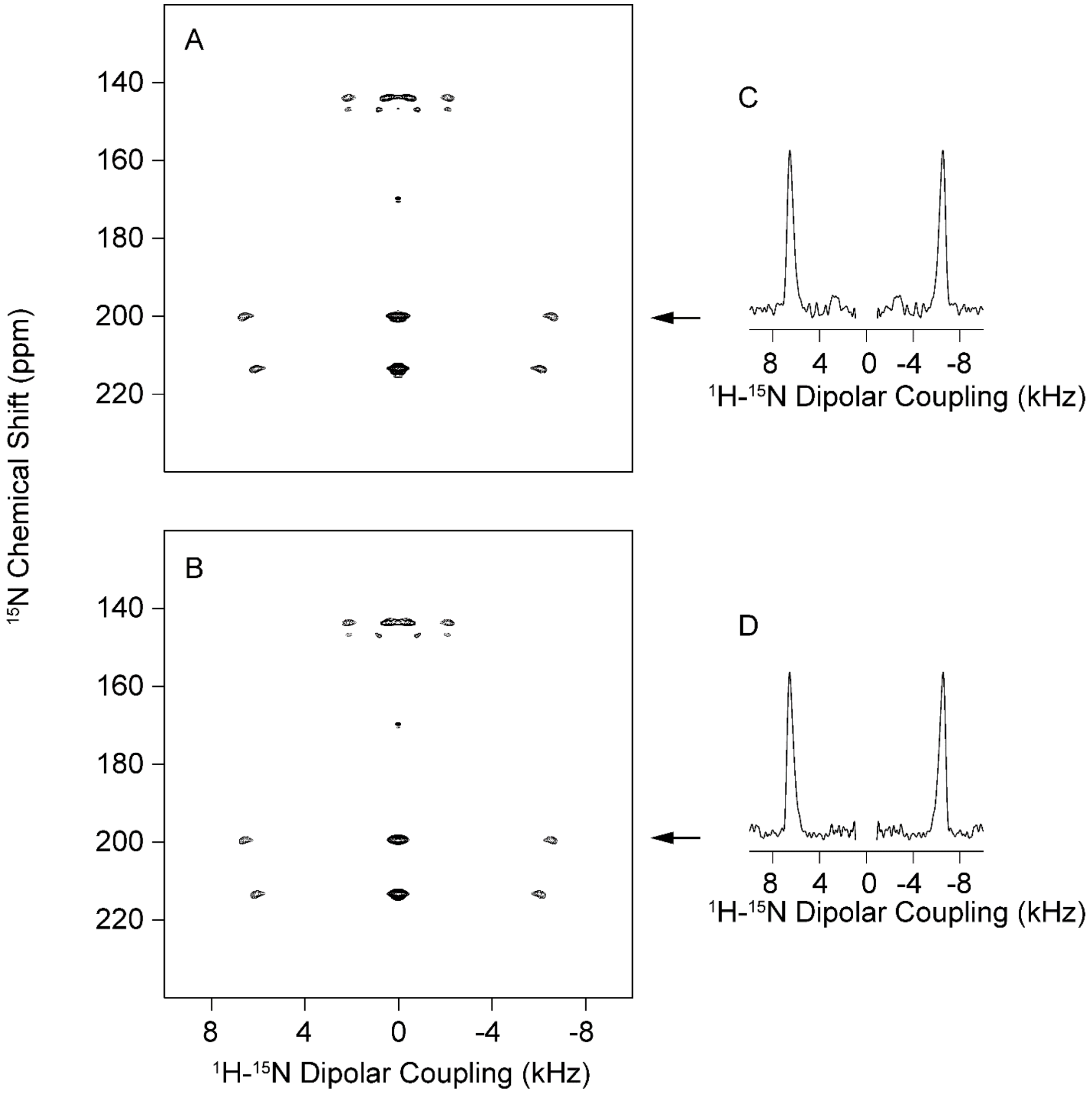

Figure 3.5. A dry ^{15}N labeled NAL crystal was used to demonstrate the water saturation method during the z-filter does not suppress signals from NAL ^{1}H. (A) and (B) are two-dimensional ^{1}H detected PISEMO spectra acquired with 4 scans, and 256 t_1 points at 53 kHz .(A) Four 12.5 kHz 1 sec long water suppression pulses of phases X,Y,X,Y were applied during the z-filter. (B) 0 kHz power was applied during a 0.8 sec z-filter. (C) and (D) are ^{1}H-^{15}N dipolar coupling frequency dimension slices through the arrow in (A) and (B) respectively.

Two-dimensional spectra of the structural-form of Pf1 coat protein in virus particles were acquired using ^{15}N-detected PISEMO (Figure 3.6A) and^{1}H-detected PISEMO with solvent suppression (Figure 3.6B). With equivalent data processing the resulting spectra are very similar. They are also similar to the previously published PISEMO spectra [22].

Thiriot *et. al.* [22] observed all 40 amide resonance signals expected at 0 ^{o}C in the helical region of the spectrum. Here only 38 resonances are observed in the helical region of the spectra. The two weakest signals are suppressed due to a smaller amount of sample and reduced signal averaging. All of the line-widths are similar, with ~250 Hz in the chemical shift dimension and ~500 Hz in the heteronuclear dipolar coupling dimension.

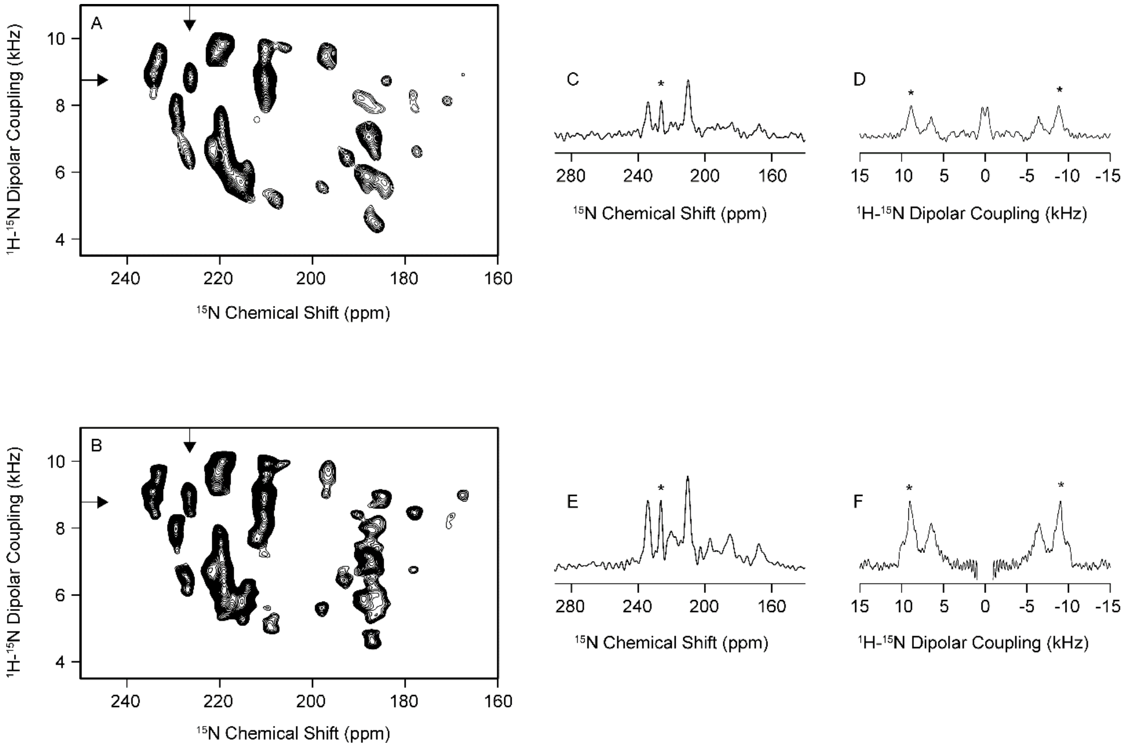

Figure 3.6. Comparisons of the PISEMO experiments of the Pf1 coat protein in phage and their one dimensional slices. (A) ^{15}N detected PISEMO spectrum acquired at 70 kHz with 64 scans and 128 t_1 points. (B) ^{1}H detected PISEMO spectrum acquired at 70 kHz with 32 scans and 256 t_1 points. (C-D) are 1D ^{15}N dimension and ^{1}H-^{15}N dipolar frequency dimension slices through peak I39 taken from (A). (E-F) are ^{15}N dimension and ^{1}H-^{15}N dipolar frequency dimension slices through peak I39 taken from (B). The arrows points to the frequency where the slices are taken, and the asterisk in (C-F) points to the location of the I39 peak in the spectra.

To make comparisons of the sensitivities of the ^{1}H-detected PISEMO spectra with the ^{15}N-detected PISEMO spectra, the number of scans in the ^{15}N detected experiments are doubled. The indirect dimension of the ^{15}N-detected PISEMO experiment measures phase insensitive ^{1}H-^{15}N dipolar coupling frequencies while the indirect dimension of the ^{1}H-detected PISEMO experiment measures phase-sensitive ^{15}N chemical shift frequencies. Indirect measurement of chemical shift generally requires two 90^o phase-shifted acquisitions for each t_1 value. The signal enhancement factors have been demonstrated previouly [8, 14, 17]:

$$\xi= (0.177)\ (\gamma_H/\gamma_N)^{3/2}\ (W_N/W_H)^{1/2}(Q_H/Q_N)^{1/2}(\eta_H/\eta_N)\ (SW_H/FW_H)^{1/2}\ (1)$$

Equation (1) can be used to determine the sensitivity enhancement factor ξ. The gyromagnetic ratio factor $(\gamma_H/\gamma_N)^{3/2}$ is 31.6 for ^{1}H-^{15}N heteronuclear experiments. The probe quality factor ratio $(Q_H/Q_N)^{1/2}$ is 1.73 as calculated from measured values given in table 1. The sample filling factor ratio η_H/η_N is 1 for a single coil probe design. Thus, equation (1) reduces to:

$$\xi=9.68\ (W_N/W_H)^{1/2}(SW_H/FW_H)^{1/2}\ (2)$$

The term $(SW_H/FW_H)^{1/2}$ influences the sensitivity enhancement factor because a much larger filter bandwidth (FW) has to be used compared to the spectral width (SW) [14]. In our experiments, to sample as fast as possible, we used a filter width of 200 MHz for a 10 MHz spectral width. In comparison, the ^{15}N-detected experiments used a 125 kHz filter bandwidth and 25 kHz spectral width. This larger filter width allowed more ^{1}H noise into the ^{1}H-detected data, reducing the signal/noise ratio. This is reflected in the $(SW_H/FW_H)^{1/2}$ factor which equals 0.224. In practice, this can be more accurately calculated by counting the data points in the detection windows due to our data processing method [17].

Throughout most of the detection window, the receiver gate was blocked, and no signal or noise was allowed through. During the detection windows, the effective dwell time is then equivalent to the multiple pulse cycle time. Distorted points within the detection window due to digital filtering are removed during data processing. The removal of the distorted points reduced the effective filter width to $1/t_s$, where t_s is the duration span of the total amount of the usable data within each detection window. In the protein experiment, 1.4 μs of usable signal data points in each cycle of 27 μs results in a $(SW_H/FW_H)^{1/2}$ value of 0.228. This value is different from previously calculated 0.224 because it reflects the removal of the distorted data points. In data processing, a total of 14 real data points was summed which resulted in 1.83 times enhancement compared to the case without such processing in the protein sample. As a result, combined with the previous calculations, 4.04 times signal enhancement for a peak that has $W_N = W_H$ can theoretically be achieved.

$$\xi=4.04\ (W_N/W_H)^{1/2} \quad (3)$$

In our protein sample, we found a range of resonance line-widths. The symbols W_N and W_H represent the resonance line-widths for the directly detected dimensions: W_N for ^{15}N detected experiments, and W_H for ^{1}H detected experiments. In fact, various levels of sensitivity enhancements for different residues were found within the same sample. In our sample, typical resonances have ^{15}N chemical shift line-width of 200 Hz, and ^{1}H - ^{15}N dipolar coupling frequency line-width of 600 Hz. This results in a theoretical sensitivity enhancement factor of 2.33. This is close to our experimental data shown in Figure 3.6. For example, the one-dimensional slices taken for peak I39 in the ^{1}H detected experiments have 1.84 (Figure 3.6E) fold sensitivity enhancement for the ^{15}N chemical shift dimension, compared to ^{15}N detection (Figure 3.6C). For the ^{1}H - ^{15}N dipolar coupling frequency dimension, 2.10 (Figure 3.6C) fold enhancement for signal/noise ratio was obtained compared to ^{15}N detection (Figure 3.6D). The application of the 0.8 sec saturation pulse during z-filter also contribute to some loss of sensitivity in the ^{1}H detection pulse to T_1 relaxation. This effect is estimated to be less than 10% based on the magnitude of the protein ^{1}H T_1.

Based on this analysis, the ^{1}H - ^{15}N heteronuclear dipolar coupling frequency line-width is the limiting factor in the sensitivity of the ^{1}H-detected PISEMO experiments. To improve the performance of the ^{1}H windowed-detection experiments, better multiple pulse sequences needs to be applied to improve ^{1}H - ^{1}H dipole-dipole averaging. In the meantime, sample qualities can be improved. Our Pf1 coat protein spectra were acquired at 0^{o}C but with the appropriate molecular motions in samples such as bilayer samples under physiological temperatures, protein line-widths can improve. The averaging due to rotational diffusion affects the decay of the ^{1}H-^{15}N dipolar coupling and ^{15}N chemical shift induction decay by different amounts. In recent studies, the resonance line-width of Pf1 coat protein in aligned triton bicelles can be improved to as narrow as 90 Hz for their ^{15}N chemical shift, and to 150 Hz for their ^{1}H-^{15}N dipolar coupling frequency at physiological temperatures and a ^{1}H frequency of 900 MHz [23]. Further line-widths improvements can be obtained with the use of aligned macrodiscs [26]. These bilayer samples are in sharp contrast to our phage-bond Pf1 coat protein used in this study which demonstrates broader line-widths and at a much lower temperature of 0^{o}C which quenches molecular motions. Therefore, it is likely that other optimized membrane protein samples can receive more benefits from the ^{1}H-detected PISEMO technique. Another factor which limits the sensitivity enhancements is the use of the States method [27] for phase sensitive ^{15}N chemical shifts detection in the indirection dimension. It requires two separate acquisitions for each t_1 value which doubles the overall experimental time. Many methods have been developed to shorten the acquisition requirements for the indirect dimensions. In particular, non-uniform sampling with data reconstruction [28-31] are becoming more widely employed in protein NMR spectroscopy. These and other methods have the potential to further improve water-suppressed versions of ^{1}H detected two-dimensional solid-state NMR experiments.

3.4 Conclusions

^{1}H detection was successfully applied to solid state NMR experiments with an oriented Pf1 phage protein sample. The application of a solvent saturation pulse during the z-filter enabled the ^{1}H detected PISEMO experiment on a hydrated protein sample, resulted in the first two-dimensional spectrum of an oriented protein obtained with the window detection technique. The sensitivity enhancement from the use of ^{1}H detection techniques is around two fold when applied to the Pf1 phage coat protein sample. However, for proteins with different ^{15}N resonances line-widths, or dipolar coupling frequency line-widths, the levels of enhancements can vary. This method will benefit future studies of membrane proteins oriented in the magnetic field.

3.5 Acknowledgement

We thank Dr. Chin Wu for help with the instrumentation and advice on data processing. We thank Dr. Jinfa Ying for assistance with the data processing script. We also thank Dr. Sabrina Berkamp and Dr. Jasmina Radoicic for assistance with sample preparation. This research was supported by grants P41EB002031 and R35GM122501 from the National Institutes of Health, and utilized the Biomedical Technology Resource Center for NMR Molecular Imaging of Proteins at the University of California, San Diego.

Chapter 3, in full, is a reprint of the material as it appears Long, Z, Opella SJ, (to be submitted), ^{1}H detection with water suppression of ^{1}H-^{15}N heteronuclear dipolar oscillations in single crystal peptide and oriented protein samples, (2019). The dissertation author is the primary researcher and author on the manuscript.

3.6 References

[1] L.B. Andreas, K. Jaudzems, J. Stanek, D. Lalli, A. Bertarello, T. Le Marchand, D.C.D. Paepe, S. Kotelovica, I. Akopjana, B. Knott, S. Wegner, F. Engelke, A. Lesage, L. Emsley, K. Tars, T. Herrmann, G. Pintacuda, Structure of fully protonated proteins by proton-detected magic-angle spinning NMR, P Natl Acad Sci USA, 113 (2016) 9187-9192.

[2] A. Bax, S. Subramanian, Sensitivity-Enhanced Two-Dimensional Heteronuclear Shift Correlation Nmr-Spectroscopy, Journal of Magnetic Resonance, 67 (1986) 565-569.

[3] D.H. Live, D.G. Davis, W.C. Agosta, D. Cowburn, Observation of 1000-Fold Enhancement of N-15 Nmr Via Proton-Detected Multiquantum Coherences - Studies of Large Peptides, Journal of the American Chemical Society, 106 (1984) 6104-6105.

[4] L. Muller, Sensitivity Enhanced Detection of Weak Nuclei Using Heteronuclear Multiple Quantum Coherence, Journal of the American Chemical Society, 101 (1979) 4481-4484.

[5] P.K. Grannell, P. Mansfield, M.A. Whitaker, C-13 Double-Resonance Fourier-Transform Spectroscopy in Solids, Phys Rev B, 8 (1973) 4149-4163.

[6] A. Bax, R.H. Griffey, B.L. Hawkins, Sensitivity-Enhanced Correlation of N-15 and H-1 Chemical-Shifts in Natural-Abundance Samples Via Multiple Quantum Coherence, Journal of the American Chemical Society, 105 (1983) 7188-7190.

[7] G. Bodenhausen, D.J. Ruben, Natural Abundance N-15 Nmr by Enhanced Heteronuclear Spectroscopy, Chem Phys Lett, 69 (1980) 185-189.

[8] Y. Ishii, R. Tycko, Sensitivity enhancement in solid state N-15 NMR by indirect detection with high-speed magic angle spinning, Journal of Magnetic Resonance, 142 (2000) 199-204.

[9] J.R. Lewandowski, J.N. Dumez, U. Akbey, S. Lange, L. Emsley, H. Oschkinat, Enhanced Resolution and Coherence Lifetimes in the Solid-State NMR Spectroscopy of Perdeuterated Proteins under Ultrafast Magic-Angle Spinning, J Phys Chem Lett, 2 (2011) 2205-2211.

[10] D.I. Hoult, Solvent Peak Saturation with Single-Phase and Quadrature Fourier Transformation, Journal of Magnetic Resonance, 21 (1976) 337-347.

[11] V. Chevelkov, B.J. van Rossum, F. Castellani, K. Rehbein, A. Diehl, M. Hohwy, S. Steuernagel, F. Engelke, H. Oschkinat, B. Reif, 1H detection in MAS solid-state NMR spectroscopy of biomacromolecules employing pulsed field gradients for residual solvent suppression, J Am Chem Soc, 125 (2003) 7788-7789.

[12] R.E. Hurd, Gradient-enhanced spectroscopy, J Magn Reson, 213 (1990) 467-473.

[13] G.J. Lu, S.H. Park, S.J. Opella, Improved H-1 amide resonance line narrowing in oriented sample solid-state NMR of membrane proteins in phospholipid bilayers, Journal of Magnetic Resonance, 220 (2012) 54-61.

[14] M. Hong, S. Yamaguchi, Sensitivity-enhanced static 15N NMR of solids by 1h indirect detection, J Magn Reson, 150 (2001) 43-48.

[15] A.A. Nevzorov, S.J. Opella, Selective averaging for high-resolution solid-state NMR spectroscopy of aligned samples, J Magn Reson, 185 (2007) 59-70.

[16] C.H. Wu, A. Ramamoorthy, S.J. Opella, High-Resolution Heteronuclear Dipolar Solid-State Nmr-Spectroscopy, J Magn Reson Ser A, 109 (1994) 270-272.

[17] C.H. Wu, S.J. Opella, Proton-detected separated local field spectroscopy, J Magn Reson, 190 (2008) 165-170.

[18] C.H. Wu, C.V. Grant, G.A. Cook, S.H. Park, S.J. Opella, A strip-shield improves the efficiency of a solenoid coil in probes for high-field solid-state NMR of lossy biological samples, Journal of Magnetic Resonance, 200 (2009) 74-80.

[19] C.V. Grant, Y. Yang, M. Glibowicka, C.H. Wu, S.H. Park, C.M. Deber, S.J. Opella, A Modified Alderman-Grant Coil makes possible an efficient cross-coil probe for high field solid-state NMR of lossy biological samples, Journal of Magnetic Resonance, 201 (2009) 87-92.

[20] P.L. Gor'kov, E.Y. Chekmenev, C. Li, M. Cotten, J.J. Buffy, N.J. Traaseth, G. Veglia, W.W. Brey, Using low-E resonators to reduce RF heating in biological samples for static solid-state NMR up to 900 MHz, J Magn Reson, 185 (2007) 77-93.

[21] C.V. Grant, C.H. Wu, S.J. Opella, Probes for high field solid-state NMR of lossy biological samples, J Magn Reson, 204 (2010) 180-188.

[22] D.S. Thiriot, A.A. Nevzorov, S.J. Opella, Structural basis of the temperature transition of Pf1 bacteriophage, Protein Sci, 14 (2005) 1064-1070.

[23] Z. Long, S.H. Park, S.J. Opella, Effects of deuteration on solid-state NMR spectra of single peptide crystals and oriented protein samples, J Magn Reson, 309 (2019) 106613.

[24] Y. Ishii, J.P. Yesinowski, R. Tycko, Sensitivity enhancement in solid-state C-13 NMR of synthetic polymers and biopolymers by H-1 NMR detection with high-speed magic angle spinning, Journal of the American Chemical Society, 123 (2001) 2921-2922.

[25] D.H. Zhou, C.M. Rienstra, High-performance solvent suppression for proton detected solid-state NMR, J Magn Reson, 192 (2008) 167-172.

[26] J. Radoicic, S.H. Park, S.J. Opella, Macrodiscs Comprising SMALPs for Oriented Sample Solid-State NMR Spectroscopy of Membrane Proteins, Biophys J, 115 (2018) 22-25.

[27] D.J. States, R.A. Haberkorn, D.J. Ruben, A Two-Dimensional Nuclear Overhauser Experiment with Pure Absorption Phase in 4 Quadrants, Journal of Magnetic Resonance, 48 (1982) 286-292.

[28] J.C.J. Barna, E.D. Laue, M.R. Mayger, J. Skilling, S.J.P. Worrall, Exponential Sampling, an Alternative Method for Sampling in Two-Dimensional Nmr Experiments, Journal of Magnetic Resonance, 73 (1987) 69-77.

[29] J.C. Hoch, Modern spectrum analysis in nuclear magnetic resonance: alternatives to the Fourier transform, Methods Enzymol, 176 (1989) 216-241.

[30] D. Rovnyak, D.P. Frueh, M. Sastry, Z.Y. Sun, A.S. Stern, J.C. Hoch, G. Wagner, Accelerated acquisition of high resolution triple-resonance spectra using non-uniform sampling and maximum entropy reconstruction, J Magn Reson, 170 (2004) 15-21.

[31] J. Ying, F. Delaglio, D.A. Torchia, A. Bax, Sparse multidimensional iterative lineshape-enhanced (SMILE) reconstruction of both non-uniformly sampled and conventional NMR data, J Biomol NMR, 68 (2017) 101-118.

Chapter 4: Design, purification and NMR spectroscopy of chimeric helical membrane proteins

4.1 Introduction

Cell membrane serves the important function to separate cytoplasm from the outside environment. At the same time, it contains essential sensor and portal proteins allowing cells to interact with its environment. In the human genome, 23% of all proteins are membrane proteins [1]. Membrane proteins are divided into three categories: integral membrane protein (IMP), membrane anchored protein, and peripheral membrane protein. Each type of membrane protein carry important functions for the cells participating in different biochemical processes. IMPs are considered part of the cellular membrane for they are embedded in the lipid bilayer. An important class of IMPs consist of α-helices that span the lipid bilayers, these IMPs are diverse and consist of one [2], two [3], three [4], four [4], five, six [5], seven [6], eight [7], nine [8], ten [9], eleven [10], twelve [11], thirteen [10], fourteen [12] helices, and more.

The studies of IMPs has been difficult compare to soluble proteins because many within the class are hard to obtain in pure forms. This is partially attributed to the highly hydrophobic properties of their transmembrane domains, which hinders both expression and purification when over-expressed in non-native hosts. Their preference for membrane partition resulted in their low solubility by themselves.

Traditionally, this problem was solved by choosing an appropriate detergent to stabilize the proteins during purification. Detergents form mixed micelles preventing exposed hydrophobic surfaces of the membrane proteins from aggregation in aqueous environments [13]. Detergents can subsequently be removed with various methods after lipids are added, including dialysis or using hydrophobic sorbents.

In addition to the stability problems during purification, sample under specific experimental conditions needs to be stable as well. The mercury transporter protein MerF has been the subject of many solid-state NMR studies because it has favorable properties in both expression-purification and NMR sample preparation [3, 14, 15]. Thus here starting from the MerF protein, a three helix protein was engineered to survey for changes in protein NMR spectra.

Building on the previous results, the chimeric protein MerF (1-72)-MerT (74-116) which consists of residue 1-72 of MerF and residue 74-116 of MerT. In the construct, all the original cysteine residues from MerF and MerT were mutated to serine to improve its stability during purification under non-reducing environments. The MerF-MerT chimera was designed based on the MerF and MerT from *pseudomonas aeruginosa* due to the presence of a more hydrophobic transmembrane helix within MerT (74-116). The protein is non-functional due to the mutation of the all the cysteine to serine. Here functional aspects of MerF and MerT are not explored, but instead, the focus would be given to the cysteine mutants to study how the third helix of MerT behaves in the lipid bilayer with or without influences from the first two helices. This three transmembrane design can be helpful for understanding the multi-transmembrane helix proteins in the lipid environments. Experimental data on the function and behavior of the third transmembrane helices of MerT remains largely absent, since the sequence between MerF and MerT contain 39% identity based on the alignments shown in Figure 4.1. It is not clear whether the MerT helix requires stabilization from the first two helices of MerT, and it is not clear how the third helix will behave within the chimera protein.

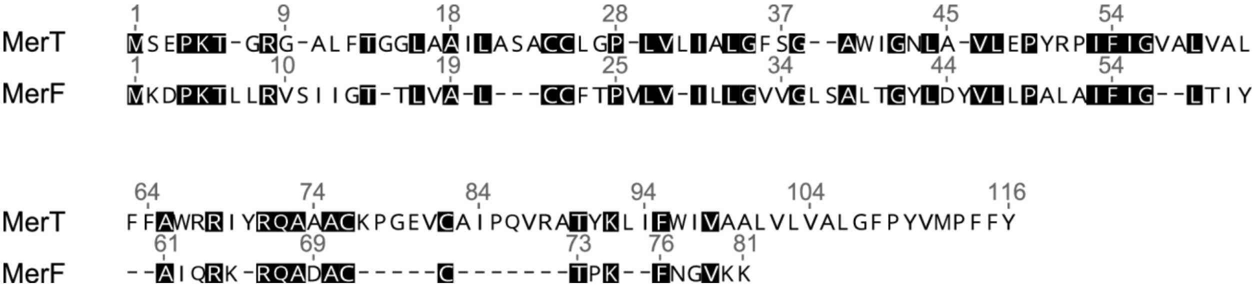

Figure 4.1 MerF and MerT alignments where identical residues are highlighted by the surrounding black box.

Another construct MerF (1-63)-MerT (89-116) that contains a shorter loop between MerF and MerT was also made. MerF (1-72)-MerT (74-116) and MerF (1-63)-MerT (89-116) differs in the intracellular loop of the protein where 24 residues are removed, two residues were put back in for convenience of cloning. This is seen in Figure 4.3 which is plotted in Protter (www.wlab.ethz.ch/protter) using Phobius (www.phobius.sbc.su.se/). Here for convenience we will refer to them as MerFTC, which stands for MerF-MerT chimera, and MerFTCΔ, which stands for MerF-MerT chimera with loop deletion. The predicted transmembrane domains are shown in Figure 4.2 calculated based on hydrophobicity calculations. However, using hydropathy plots shown in Figure 4.3, it is evident that hydrophobic residues exists beyond what was predicted to be transmembrane residues, as a result, whether the third helix in MerFTC constructs changes the first two helix can be deduced by comparisons of their NMR data.

Given previously observed conformational bias with N and C-terminal residues in MerF [15], the two chimera proteins made here can have interesting differences beyond the addition of residues. The chimera proteins can be used to understand effects caused by transient or stable interactions between the transmembrane helices or to illustrate preferences in conformational bias. Moreover, these effects can also be influenced by bilayer depths which can also be explored using this protein as a model system. The *pseudomonas aeruginosa* membrane consist of 35% of C16:0 phospholipids [16], by comparing lipid bilayers of C16:0 PC (2.6 nm) and C12:0 PC (1.95 nm) will predict that the thickness of the hydrocarbon regions to differ by 0.65 nm[17] or 1.2 turns of α-helix which is about 3-4 residues difference in the helix. The predicted 20 residues of the third helix of MerT roughly matches the thickness of the C16:0 PC bilayers. It is known previously that the MerF helical regions which span the membrane bilayers range between residues 5-40 (transmembrane domain 1) and 45-70 (transmembrane domain 2) [18]. The effects of bilayer depth and specific and non-specific transmembrane domain interactions can be studied in using the MerFTC constructs.

Large membrane proteins often can be found to have bulky loops between transmembrane helices. NMR studies of the two chimeric proteins can also help to better model and design stable multi-transmembrane helix proteins for functional scaffolds for the purposes of designing enzymatic reactions within or close to the surface of the membrane. Behavioral difference seen in NMR can also help to design spectroscopic tools to better study integral membrane proteins with different levels of conformational dynamics to achieve specific functions. MerFTC and MerFTCΔ proteins will serves as a stepping stone towards the development of NMR methods for more complex proteins.

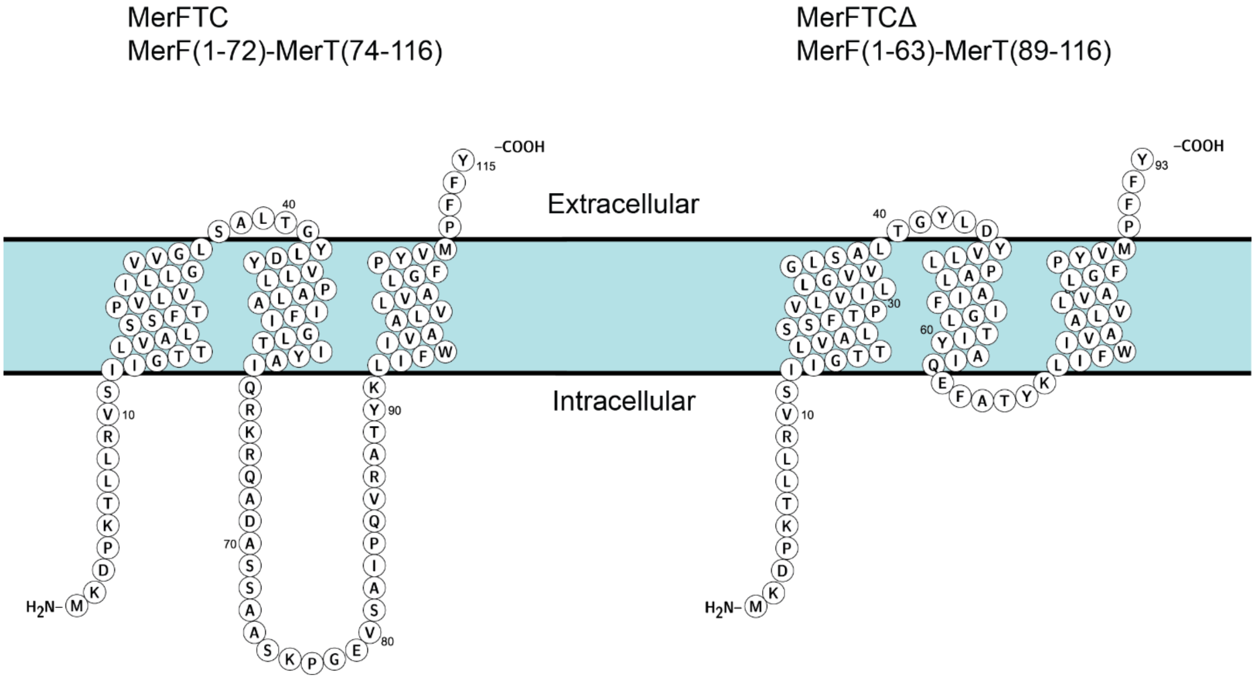

MerFTC
MerF(1-72)-MerT(74-116)

MerFTCΔ
MerF(1-63)-MerT(89-116)

Figure 4.2. Putative organization of the MerFTCΔ or MerF (1-72)-MerT (74-116) and MerFTCΔ orMerF (1-63)-MerT (89-116) proteins in the membrane bilayer shown in cyan.

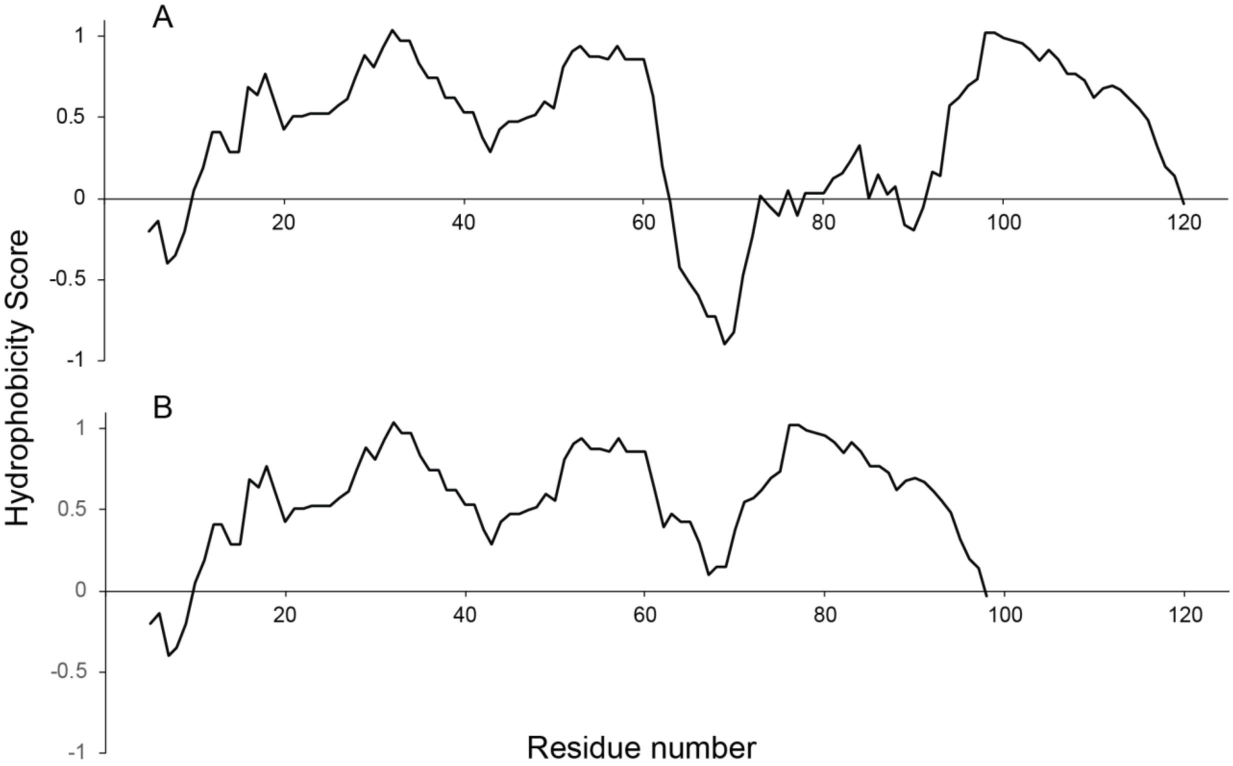

Figure 4.3 Hydrophobicity score generated by ProtScale (www.expasy.org), using the Eisenberg hydrophobicity scale. (A) MerF (1-63)-MerT (89-116) or MerFTC showing residue 5-120. (A) MerF (1-72)-MerT (74-116) or MerFTCΔ showing residue 5-98.

4.2 Materials and Methods

Codon optimization was performed to boost the expression level of the chimera constructs in *E.Coli*. Gene synthesis was performed with Genewiz (www.genewiz.com) and synthesized DNA was placed in pGEX vector (www.gelifesciences.com), and expressed in BL21 cells (www.neb.com). The DNA and protein sequences for the two constructs are shown below:

DNA sequence for the MerF(1-72)-MerT(74-116) protein (MerFTC)

5’-

GGATCCATGAAAGATCCGAAAACCCTGCTGCGCGTGAGCATTATTGGCACCACCC
TGGTGGCGCTGAGCAGCTTTACCCCGGTGCTGGTGATTCTGCTGGGCGTGGTGG
GCCTGAGCGCGCTGACCGGCTATCTGGATTATGTGCTGCTGCCGGCGCTGGCGA
TTTTTATTGGCCTGACCATTTATGCGATTCAGCGCAAACGCCAGGCGGATGCGAGC
AGCGCGGCGAGCAAACCGGGCGAAGTGAGCGCGATTCCGCAGGTGCGCGCGAC
CTATAAACTGATTTTTTGGATTGTGGCGGCGCTGGTGCTGGTGGCGCTGGGCTTTC
CGTATGTGATGCCGTTTTTTTATATGCATCATCATCATCATCAT

-3’

Protein sequence for the MerF(1-72)-MerT(74-116) protein (MerFTC)

N-
GSMKDPKTLLRVSIIGTTLVALSSFTPVLVILLGVVGLSALTGYLDYVLLPALAIFIGLTIYAI
QRKRQADASSAASKPGEVSAIPQVRATYKLIFWIVAALVLVALGFPYVMPFFYMHHHH
HH

-C

DNA sequence for the MerF(1-63)-MerT(89-116) protein (MerFTCΔ)

5’-

GGATCCATGAAAGATCCGAAAACCCTGCTGCGCGTGAGCATTATTGGCACCACCC
TGGTGGCGCTGAGCAGCTTTACCCCGGTGCTGGTGATTCTGCTGGGCGTGGTGG
GCCTGAGCGCGCTGACCGGCTATCTGGATTATGTGCTGCTGCCGGCGCTGGCGA
TTTTTATTGGCCTGACCATTTATGCGATTCAGGAATTCGCGACCTATAAACTGATTT

TTTGGATTGTGGCGGCGCTGGTGCTGGTGGCGCTGGGCTTTCCGTATGTGATGCC GTTTTTTTATATGCATCATCATCATCATCAT

-3’

Protein sequence for the MerF(1-63)-MerT(89-116) protein (MerFTCΔ)

N-
GSMKDPKTLLRVSIIGTTLVALSSFTPVLVILLGVVGLSALTGYLDYVLLPALAIFIGLTIYAI QEFATYKLIFWIVAALVLVALGFPYVMPFFYMHHHHHH

-C

Growth of the bacterial culture is started with transformation of the pGEX_MerFTC plasmid (or the pGEX_MerFTCΔ plasmid) into BL21 cells, a single colony is picked into a 20 mL 10% LB supplemented M9 media or LB culture and grown overnight. Then the small culture is transferred to the 1 L M9 or LB culture and grown until reaching an O.D.600 of 0.7 at temperatures between 25^{o}C and 37^{o}C, and induced by 50 μM IPTG for 6 hours. 250 mL worth of cell pellet is lysed in 35 mL of lysis buffer (20mM Tris-HCl pH 8.0, 15% glycerol, and 0.5M NaCl) by sonication. 40 unit of DNAse I (www.neb.com) is then added to the lysate and incubated for 10 minutes at room temperature before centrifugation at 40k rpm for 1 hour. The resulting pellet is washed with 40 mL of 20mM Tris-HCl pH 8.0 for 4 minutes, sonicated lightly and then centrifuge at 40k rpm to re-pellet. The resulting inclusion body is then sonicated in binding buffer (1% SDS, 0.5% N-lauroyl sarcosine with 20 mM Tris-HCl, 500 mM NaCl) and then centrifuged at 5k rpm for 10 minutes before loading onto a 20 mL Ni-NTA column. Binding through gentle shaking is completed for 4 hours. The column is then washed with 20 column volumes of thrombine cleavage buffer (0.5% N-lauroyl sarcosine, 20 mM Tris-HCl pH 8.0 , and 0.5 M NaCl) and then cleaved with 1000 units of bovine serum thrombin (www.mpbio.com) for 14 hours. The column is then washed with 200 mL of binding buffer before eluting with 50 mL of elution buffer (0.5% SDS, 20 mM Tris-HCl, pH 8.0, 250 mM Imidazole) Size exclusion chromatography was performed to further purify the desired proteins using a Superdex 200 Highload 26/60 column using buffer containing 0.5% SDS 20 mM HEPEs pH 7.5 and 50 mM NaCl. SDS-PAGE gels sampling the purification processes are shown in Figure 4.4 and Figure 4.5 for the two constructs respectively. Alternatively, purification was carried out using reverse-phase high-pressure liquid chromatography (rp-HPLC) for the MerFTC protein using a C4 column (www.waters.com) with a 2,2,2-trifluroroethanol/isopropanol/acetonitrile gradient . HPLC requires complete dialysis of SDS from the eluted proteins which results in white precipitates. The precipitated protein is then lyophilized to powder and dissolved in 50% trifluoroethanol (TFE)-water solution containing 0.1% trifluoroaceticacid (TFA) solution for rp-HPLC purification using a water-acetonitrile/TFE/isopropanol gradient with 0.1% trifluoroacetic acid on a C4 column (www.waters.com).

Solution NMR spectra for the MerFTC and MerFTCΔ samples with 5.0 pH in 20 mM HEPES buffer were acquired at 800 MHz ^{1}H frequencies for the temperature experiments and the two-dimensional HSQC at 75^{o}C. The spectra for ^{1}H/^{2}H exchange experiments were acquired at 600 MHz ^{1}H frequency at 50^{o}C. Solid-state NMR samples of DPPC/DHPC q=3.0 bicelles at pH7.5 were prepared using established protocols[15, 19, 20]. Oriented sample solid-state NMR spectra were acquired at 700 MHz ^{1}H frequency using 50 kHz $B_{1,}$ 5 sec recycle delay for the SAMMY experiment, and 6 sec recycle delay for the cross-polarization experiment using 60-100% and 100-60% double ramps. Solid-state NMR spectra were acquired at 40^{o}C. Spectrum analysis and data processing were performed using Topspin (www.bruker.com).

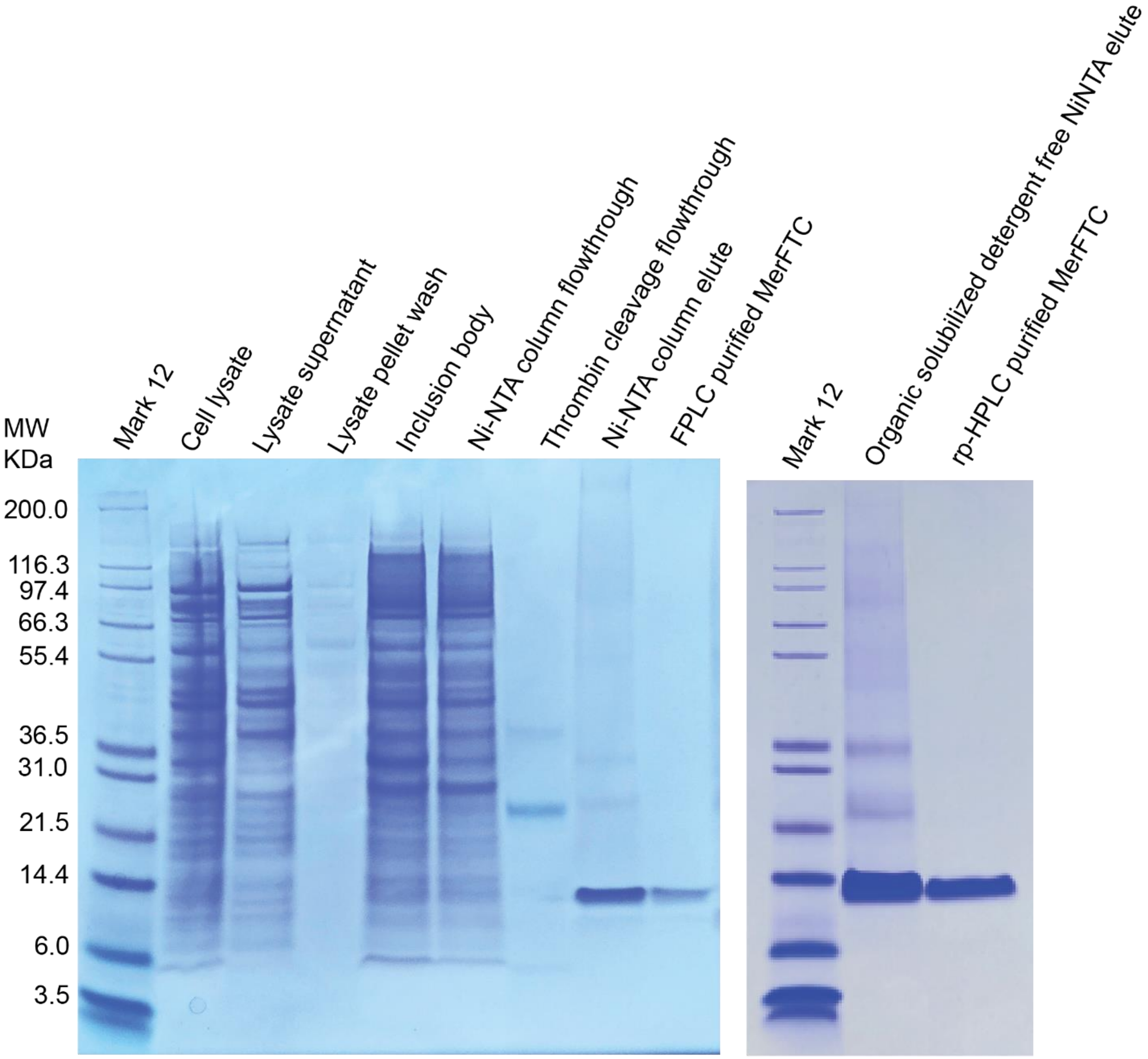

Figure 4.4 Gel showing purification of fusion protein MerFTC which is short for MerF (1-72)-MerT (74-116). (Lane1) Mark12. (Lane2) Cell lysate. (Lane3) Lysate supernatant. (Lane 4) Pellet wash (Lane 5) Inclusion body. (Lane 6) Nickel column flowthrough. (Lane 7) Thrombin cleavage flowthrough. (Lane 8) Nickel column elute of the cleaved MerFTCΔ. (Lane 9) Size exclusion chromatography purified MerFTC. (Lane 10) Mark 12. (Lane 11) Concentrated NiNTA eluted MerFTC dissolved in organics before rp-HPLC injection. (Lane 12) Pure MerFTC after rp-HPLC this is an alternative method to size exclusion chromatography.

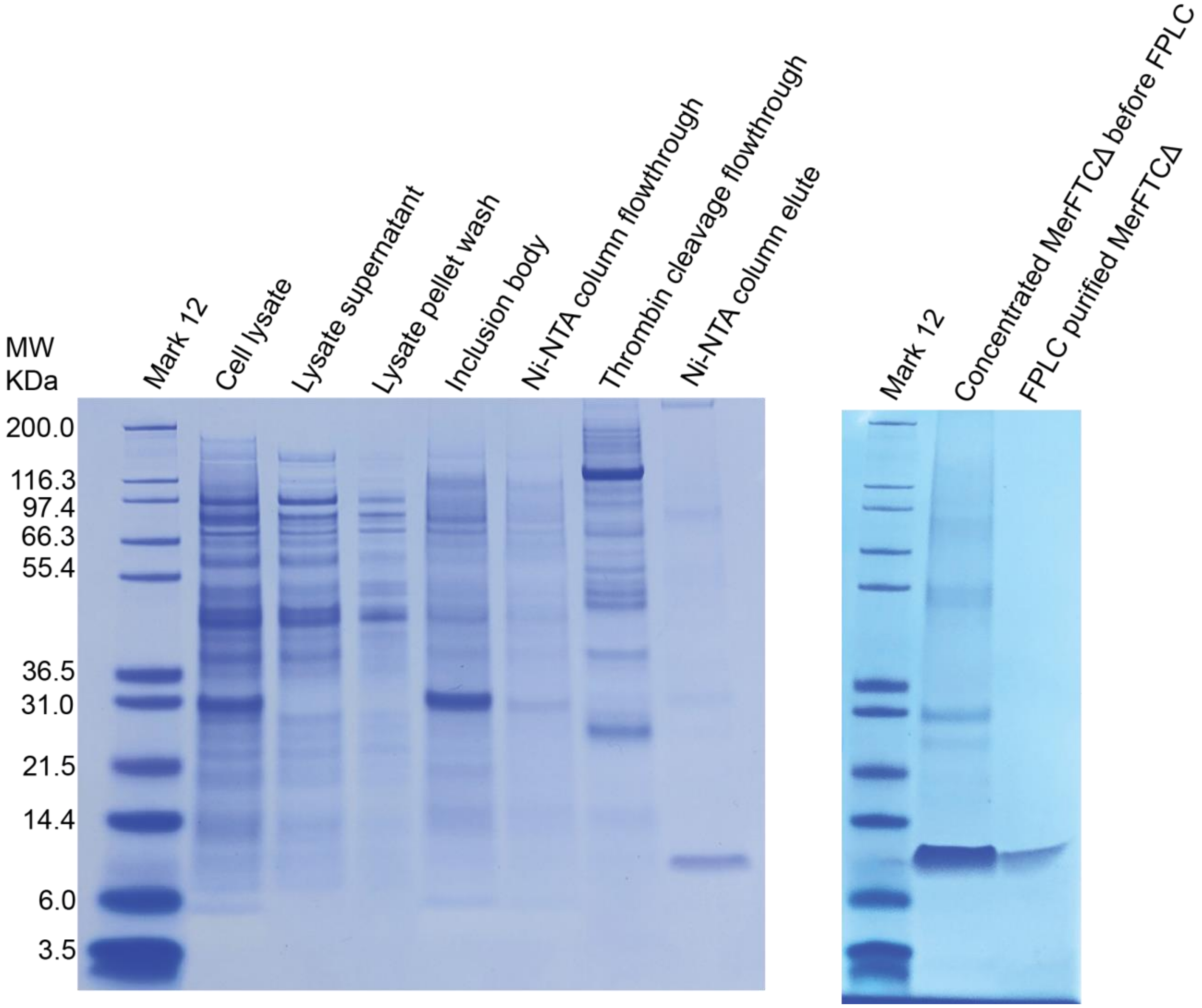

Figure 4.5 Gel showing purification of fusion protein MerFTCΔ which is short for MerF (1-63)-MerT (89-116). (Lane1) Mark12. (Lane2) Cell lysate. (Lane3) Lysate supernatant. (Lane 4) Pellet wash (Lane 5) Inclusion body. (Lane 6) Nickel column flowthrough. (Lane 7) Thrombin cleavage flowthrough. (Lane 8) Nickel column elute of the cleaved MerFTCΔ. (Lane 9) Mark 12. (Lane 10) Concentrated NiNTA eluted MerFTCΔ before size exclusion chromatography. (Lane 11) Pure MerFTCΔ after size exclusion chromatography.

4.3 Results and Discussions

NMR experiments of the MerFTC and MerFTCΔ were initially carried out in 0.5 M SDS for solution NMR expeirments to obtain approximate information about the lengths of the transmembrane helices. From Figure 4.6 it is evident that both proteins are stable at high temperatures, perhaps due to a lack of significant three dimensional folds such as that for globular proteins. This is common to membrane proteins where heat of denaturation can range to up to the boiling point. The transmembrane domains of the proteins are mostly embedded within the SDS mixed micelles, thus protected from protein aggregation. The fact that MerFTCΔ is more prone to aggregation during protein purification which suggests the existence of conformations where protein-protein interactions can be more favorable than protein- detergent interactions. This could be caused by detergent mismatch. In both MerFTC and MerFTCΔ spectral quality improves at higher temperatures. This is seen both in the one-dimensional spectra in Figure 4.6A and B. The two dimensional spectra of MerFTC and MerFTCΔ are shown in Figure 4.7A and B respectively. Of the 124 resonances in the MerFTC protein, there are 7 proline, therefore, about 114 resonances are expected in the two-dimensional spectrum. In MerFTCΔ, there are 5 proline residues in the 102 residue protein, therefore 97 resonances are expected. In Figure 4.8 B even though less than or equal to 97 resonances were expected 162 were counted, suggesting two sets of signals were present in the two-dimensional spectra. Examples of the additional resonances in Figure 4.7B by comparisons with Figure 4.7A are indicated by the red circle drawn around the resonances. This could be due to alternative conformations or protein dimerization and aggregation.

It is known that different detergents have different effects on different proteins. The use of detergents with shorter or longer hydrophobic tails has not been attempted for the MerFTCΔ protein. ^2H_2O exchange experiments were carried out with the MerFTC sample. With increasing amount of ^2H_2O in the sample, the labile ^{15}N-^1H sites rapidly exchange with the solvent and this exchange significantly reduces their signals. On the other hand, the structured, or buried sites would not be affected. In Figure 4.8 D, there are 25 resonances from MerFTC, this number is 11 residues more than what was found for the MerF protein reported in previous studies [14]. Previously, 25 residues were found to be alpha helical in SDS for MerF compared to 14 that resisted ^2H_2O exchange. With 11 and 14 residues in the two helices respectively, the results suggest only about 7 residues per helix are non-labile in solvent $^1H/^2H$ exchange. With this assumption the MerFTC protein should have one more helix, which agree with the predictions by the hydropathy plot.

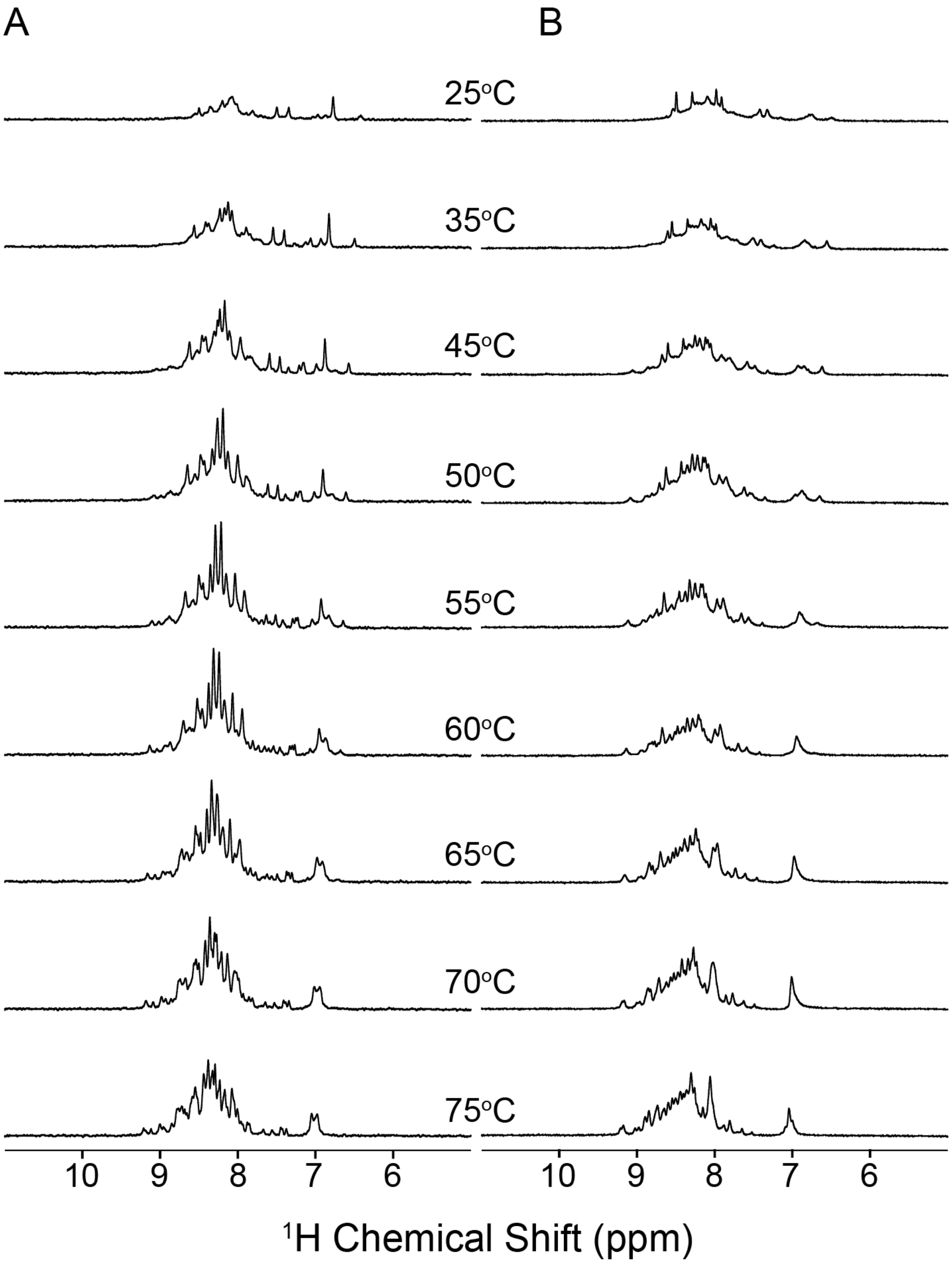

Figure 4.6 (A) ^{15}N edited ^{1}H spectra of the ^{15}N uniformly labeled MerF (1-72)-MerT (74-116) protein at pH 5.0, 50°C in 90% $^{1}H_2O$ and 10% $^{2}H_2O$, from 25°C -75°C.

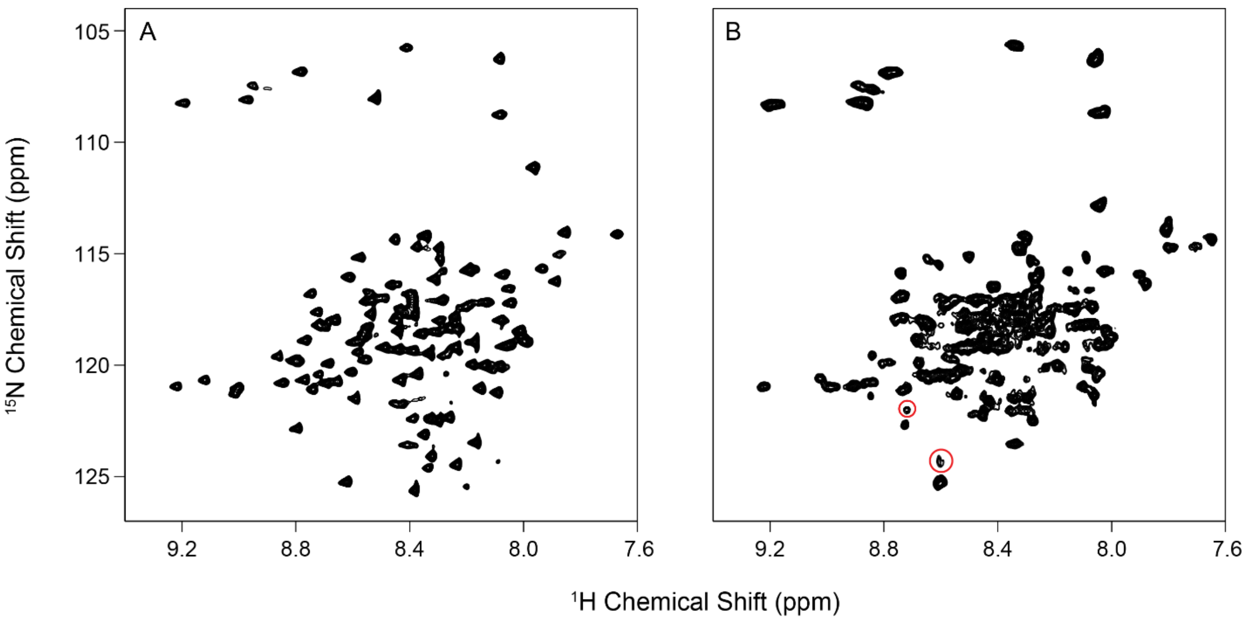

Figure 4.7 (A) Two-dimensional HSQC spectrum of the ^{15}N uniformly labeled MerF (1-72)-MerT (74-116) protein at pH 5.0, 75°C. Spectra were acquired at 800 MHz ^{1}H frequency. (B) HSQC spectrum of the ^{15}N uniformly labeled MerF (1-63)-MerT (89-116) protein at pH 5.0, 75°C. Spectra were acquired at 800 MHz ^{1}H frequency.

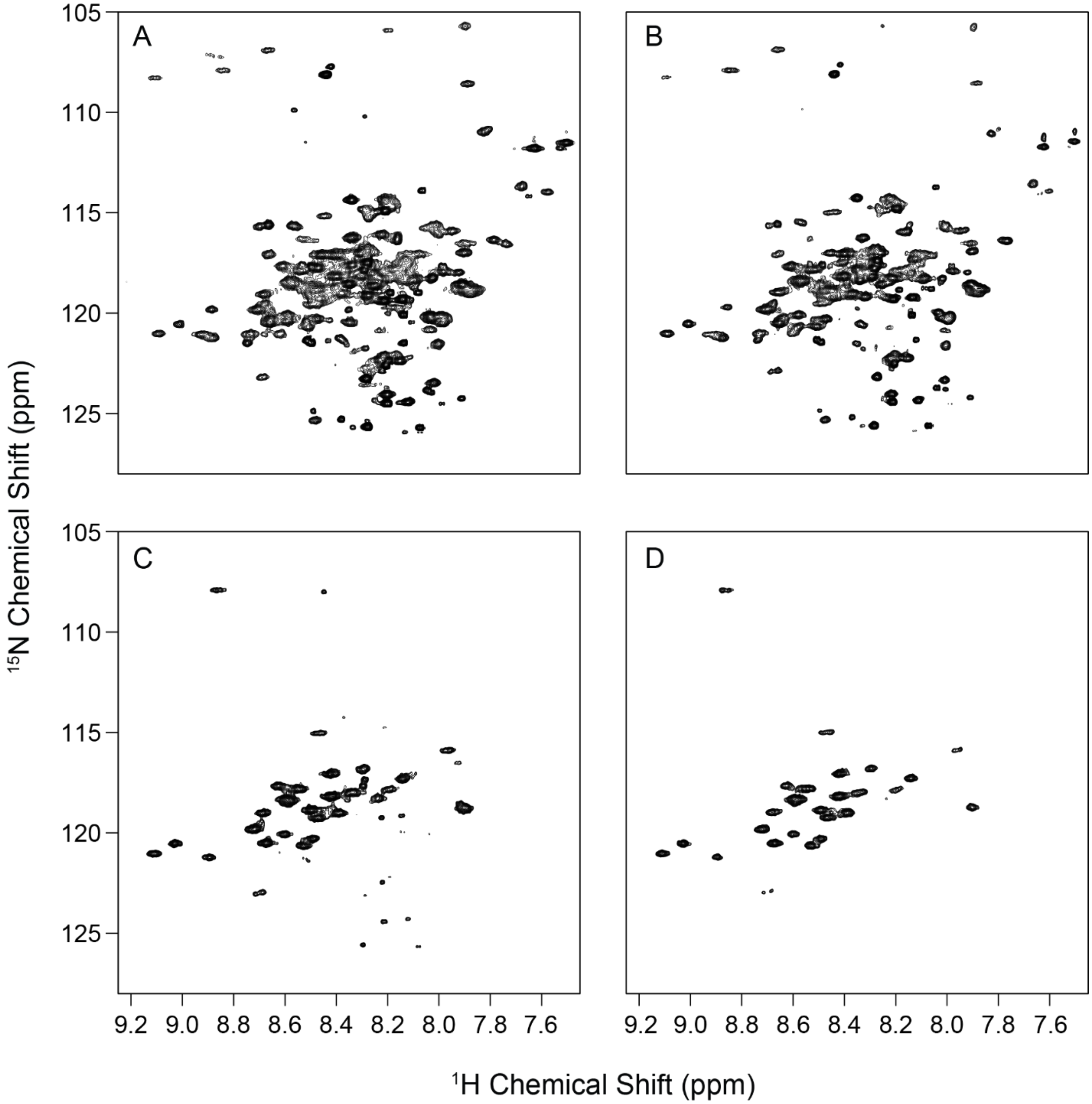

Figure 4.8 HSQC spectrum of the ^{15}N uniformly labeled MerF (1-72)-MerT (74-116) protein at pH 5.0, 50^{o}C (A) in 90% $^{1}H_2O$ and 10% $^{2}H_2O$, (B) in 60% $^{1}H_2O$ and 40% $^{2}H_2O$, (C) in 20% $^{1}H_2O$ and 80% $^{2}H_2O$, and (D) in 100% $^{2}H_2O$. Spectra were acquired at 600 MHz ^{1}H frequency.

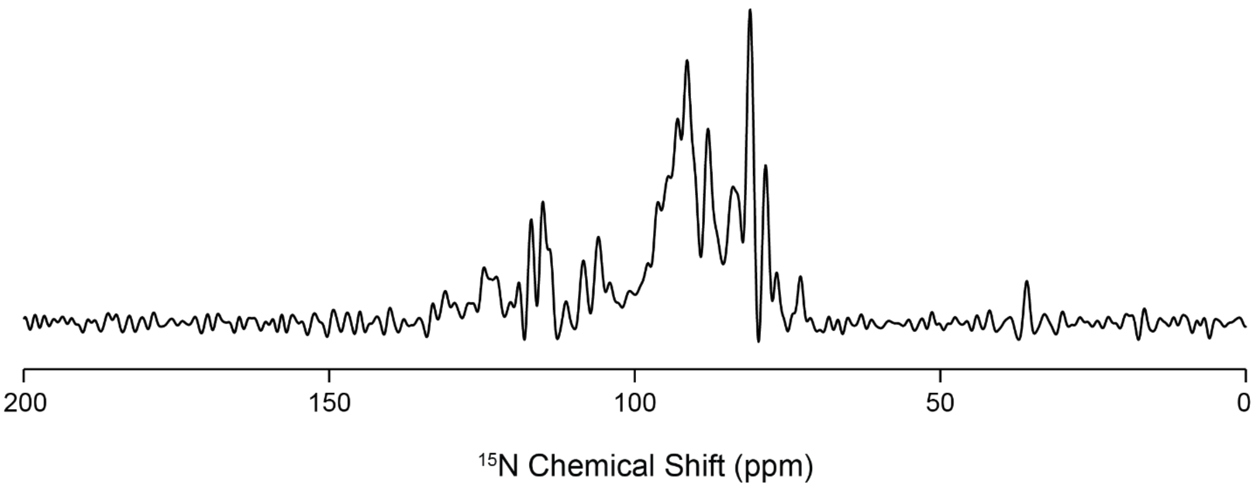

Figure 4.9 Oriented sample solid-state NMR spectra of MerFTC or MerF (1-72)-MerT (74-116) in DPPC/DHPC q=3.0 bicelle, pH 7.5. Spectra were collected at 40°C, with 8k scans, 6 sec recycle delay. Spectrum was acquired at 700 MHz ^{1}H frequency.

To further investigate the structural features of the transmembrane helices in MerFTC. Oriented sample solid-state NMR was used. The one-dimensional cross-polarization spectrum of MerFTC is shown in Figure 4.9 and the two-dimensional spectrum of MerFTC is shown in Fiugre 4.10. The one-dimensional spectrum in Figure 4.9 shows well aligned resonances within bicelles which have bilayer normal perpendicular to the external magnetic field. The two dimensional spectrum of MerFTC in bicelle shows additional resonance densities in between 100 ppm – 90 ppm region compared to the spectra of MerFt [3], leading to a conclusion that the third helix exist in the lipid bilayers. Assignments, however, is needed to further verify the resonances that belongs to the third helix. Figure 4.11 shows a prediction of the structure of MerFTC using homology prediction. The added helix is shown interacting with the first two helices within MerFTC. To verify this prediction requires further experimental evidence, and will be studied in future work.

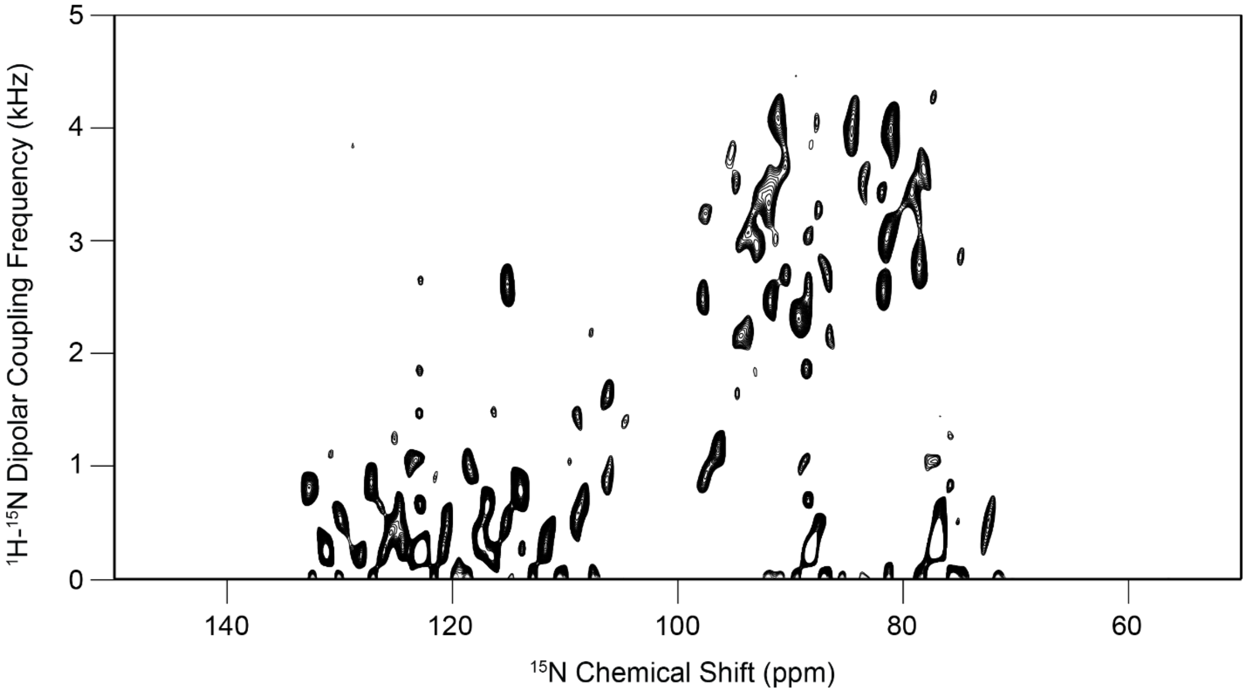

Figure 4.10 Oriented sample solid-state NMR spectra of MerFTC or MerF(1-72)-MerT(74-116) in DPPC/DHPC q=3.0 bicelle, pH 7.5. Spectra were collected at 40°C, with 1024 scans, 60 t_1 and 5 sec recycle delay. Spectrum was acquired at 700 MHz ^{1}H frequency.

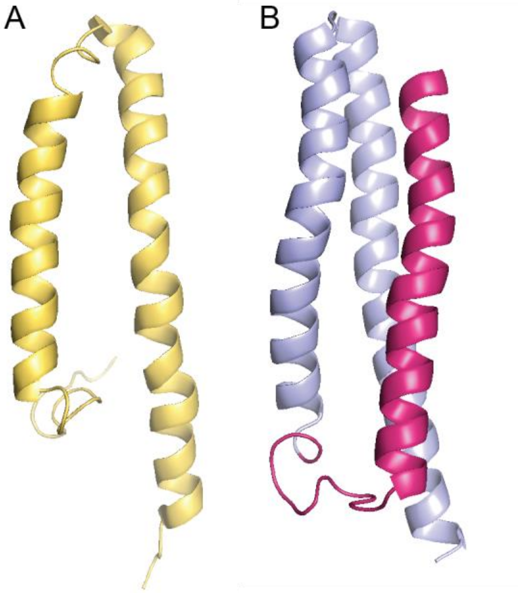

Figure 4.11 (A) structure of MerF protein in DMPC proteoliposomes 2OMZ (B) Model of MerFTC generated from IntFold program, the putated third helical loop is shown in front with the C-terminus pointing upwards in pink. From this structure prediction that has not taken into consideration of the effects of lipids, the third helix may form hydrophobic pockets with the first two helices.

4.4 Conclusions

The MerFTC and MerFTCΔ are two different chimeric proteins of MerF and MerT that have been successfully expressed here for NMR studies. In solution NMR, $^1H/^2H$ exchange experiment shows the existence of additional structure of MerFTC within the fold suggesting the existence of a third transmembrane helix. This is verified by solid-state NMR data showing additional resonance densities in the two-dimensional spectrum. Solution NMR data also show that the MerFTC protein is stable without a clear phase transition behavior when temperature is raised gradually to 75^oC. Further experiments are needed to verify the existence and structure of the third transmembrane helix in MerFTC.

4.5 Acknowledgement

We thank Dr. Sang Ho Park and Emily Wu for helpful discussions.

4.6 References

[1] M. Uhlen, L. Fagerberg, B.M. Hallstrom, C. Lindskog, P. Oksvold, A. Mardinoglu, A. Sivertsson, C. Kampf, E. Sjostedt, A. Asplund, I. Olsson, K. Edlund, E. Lundberg, S. Navani, C.A. Szigyarto, J. Odeberg, D. Djureinovic, J.O. Takanen, S. Hober, T. Alm, P.H. Edqvist, H. Berling, H. Tegel, J. Mulder, J. Rockberg, P. Nilsson, J.M. Schwenk, M. Hamsten, K. von Feilitzen, M. Forsberg, L. Persson, F. Johansson, M. Zwahlen, G. von Heijne, J. Nielsen, F. Ponten, Proteomics. Tissue-based map of the human proteome, Science, 347 (2015) 1260419.

[2] S.H. Park, F.M. Marassi, D. Black, S.J. Opella, Structure and dynamics of the membrane-bound form of Pf1 coat protein: implications of structural rearrangement for virus assembly, Biophys J, 99 (2010) 1465-1474.

[3] A.A. De Angelis, S.C. Howell, A.A. Nevzorov, S.J. Opella, Structure determination of a membrane protein with two trans-membrane helices in aligned phospholipid bicelles by solid-state NMR spectroscopy, J Am Chem Soc, 128 (2006) 12256-12267.

[4] J.R. Wilson, C. Leang, A.P. Morby, J.L. Hobman, N.L. Brown, MerF is a mercury transport protein: different structures but a common mechanism for mercuric ion transporters?, Febs Lett, 472 (2000) 78-82.

[5] G. Calamita, The Escherichia coli aquaporin-Z water channel, Mol Microbiol, 37 (2000) 254-262.

[6] R. Strotmann, K. Schrock, I. Boselt, C. Staubert, A. Russ, T. Schoneberg, Evolution of GPCR: change and continuity, Mol Cell Endocrinol, 331 (2011) 170-178.

[7] M.L. Oldham, J. Chen, Snapshots of the maltose transporter during ATP hydrolysis, Proc Natl Acad Sci U S A, 108 (2011) 15152-15156.

[8] C. Toyoshima, M. Nakasako, H. Nomura, H. Ogawa, Crystal structure of the calcium pump of sarcoplasmic reticulum at 2.6 angstrom resolution, Nature, 405 (2000) 647-655.

[9] G. Katona, U. Andreasson, E.M. Landau, L.E. Andreasson, R. Neutze, Lipidic cubic phase crystal structure of the photosynthetic reaction centre from Rhodobacter sphaeroides at 2.35A resolution, J Mol Biol, 331 (2003) 681-692.

[10] A. Albuquerque-Wendt, H.J. Hutte, F.F.R. Buettner, F.H. Routier, H. Bakker, Membrane Topological Model of Glycosyltransferases of the GT-C Superfamily, Int J Mol Sci, 20 (2019).

[11] S. Ekici, H. Yang, H.G. Koch, F. Daldal, Novel transporter required for biogenesis of cbb3-type cytochrome c oxidase in Rhodobacter capsulatus, MBio, 3 (2012).

[12] M. PanayotovaHeiermann, S. Eskandari, E. Turk, G.A. Zampighi, E.M. Wright, Five transmembrane helices form the sugar pathway through the Na+/glucose cotransporter., Journal of Biological Chemistry, 272 (1997) 20324-20327.

[13] C. Tanford, The hydrophobic effect : formation of micelles and biological membranes, 2nd edition. ed., 1979.

[14] S.C. Howell, M.F. Mesleh, S.J. Opella, NMR structure determination of a membrane protein with two transmembrane helices in micelles: MerF of the bacterial mercury detoxification system, Biochemistry, 44 (2005) 5196-5206.

[15] G.J. Lu, Y. Tian, N. Vora, F.M. Marassi, S.J. Opella, The structure of the mercury transporter MerF in phospholipid bilayers: a large conformational rearrangement results from N-terminal truncation, J Am Chem Soc, 135 (2013) 9299-9302.

[16] I.C. Hancock, P.M. Meadow, The extractable lipids of Pseudomonas aeruginosa, Biochim Biophys Acta, 187 (1969) 366-379.

[17] B.A. Lewis, D.M. Engelman, Lipid bilayer thickness varies linearly with acyl chain length in fluid phosphatidylcholine vesicles, J Mol Biol, 166 (1983) 211-217.

[18] Y. Tian, G.J. Lu, F.M. Marassi, S.J. Opella, Structure of the membrane protein MerF, a bacterial mercury transporter, improved by the inclusion of chemical shift anisotropy constraints, J Biomol NMR, 60 (2014) 67-71.

[19] A.A. De Angelis, S.J. Opella, Bicelle samples for solid-state NMR of membrane proteins, Nat Protoc, 2 (2007) 2332-2338.

[20] S.H. Park, A.A. De Angelis, A.A. Nevzorov, C.H. Wu, S.J. Opella, Three-dimensional structure of the transmembrane domain of Vpu from HIV-1 in aligned phospholipid bicelles, Biophys J, 91 (2006) 3032-3042.

Chapter 5: Application of NMR to the G protein-coupled receptor CXCR2 and its ligand CXCL5

5.1 Introduction

Until recently, 37% of all the FDA approved drugs targeting 672 unique human proteins target G-protein coupled receptors (GPCR) [1]. CXCR2 is a GPCR, it is a class A rhodopsin like GPCR and also belongs to the subfamily of CXC chemokine receptors. GPCRs are large integral membrane proteins that have 7-transmembrane domains. GPCR proteins share a lot of other similar features such as that they have their N-terminal domain in the extracellular side, and the C-terminal domain in the cytosol. Most importantly, one of the most important aspect of their functions involves its interaction with G proteins which can associate to the intracellular domains of GPCRs. The activation of the G proteins by GPCRs results in a myriad of signaling events which involves different protein kinases pathways, for example, mitogen-activated protein kinase, phosphatidylinositol 3-kinase, protein kinase A, B, and C. As a result, the consequences of the GPCR activation influences many levels of cellular biochemistry. Each GPCR are involved in different signaling events sensing different stimulations and relaying different signals across biological systems.

The function of CXCR2 is closely related to that of CXCR1. The two proteins has overlapping functions in chemotaxis: they both help traffic neutrophils to the site of inflammation [2]. Human CXCR1 and CXCR2 proteins also share close amino acid sequence resemblance sharing 77% identity. An alignment of the CXCR1 and CXCR2 amino acid sequences is shown in Figure 5. 1, residues that are different between them are highlighted. The locations of CXCR1 N-terminal, C-terminal and transmembrane domains are indicated below the amino acid sequences based on experimental data [3]. It can also be seen from Figure 5. 1 that helix 1, 2, 3 and 6 of CXCR1 and CXCR2 are completely the same, as well as all loops except for extracellular loop 2 (ECL2). Besides several key conserved residues, the N and C terminal domain of the CXCR1 and CXCR2 are almost completely different. This difference is reflected in their functional differences, where CXCR2 can be activated by 7 different chemokine ligands (CXCL1 , CXCL2, CXCL3, CXCL5, CXCL6, CXCL7, and CXCL8 (or IL-8)), CXCR1 can only be potently activated by 2 chemokine ligands (CXCL6 and CXCL8 (or IL-8)) [2]. CXCR2 has been targeted in many areas of inflammatory diseases, it is now emerging as an important drug target in cancer therapy [4]. Drugs specifically targeting CXCR2 might confer benefits to minimize adverse effects of targeting the abundant neutrophil in the immune system. Understanding the differences of CXCR1 and CXCR2 interactions with their ligand thus carries great relevance for these targeted therapies.

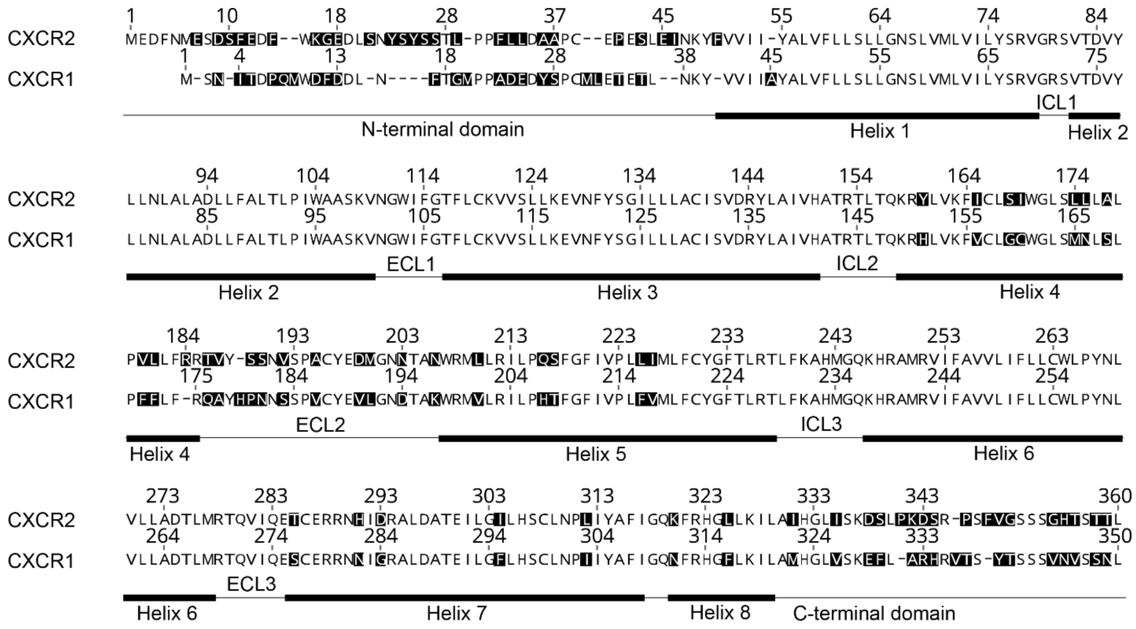

Figure 5.1 Alignment comparing the amino acid sequence of CXCR1 and CXCR2 and their N- and C- terminal domains.

During chemotaxis, neutrophils travel through the blood stream towards the origin of the stress signals. Stress is often caused by the detection of foreign materials, such as pathogens, or it can be caused by various types of injury in the tissue. To signal stress, tissue cells such as epithelial cells produce and secrete chemokine proteins to the surrounding environments. The chemokines form a gradient following which the neutrophils then can chase to the site of origin for the inflammation [5]. CXCL1, CXCL2, CXCL3, CXCL5, CXCL6, CXCL7, and CXCL8 are all CXC chemokine proteins and they all have similar folds [6]. In terms of their functions, there are discrepancies in literature in whether the ligands CXCL1, CXCL6, and CXCL7 bind to or activate CXCR1 *in vivo* [2, 7, 8], and *in vitro* [9]. The literature however, has consensus over the bias of chemokines for CXCR2 or CXCR1. The chemokine CXCL5 was chosen for studies here for it was reported to have been purified in enough quantities for biophysical studies [10], and its preference for CXCR2 but not CXCR1 in chemotaxis of neutrophils in human or mouse has been clear in literature [9, 11]. CXCL5 is also called epithelial-derived neutrophil-activating peptide 78 (ENA-78). It was first identified with neutrophil activating properties because of its sequence homology to IL-8 [12]. CXCL5 has a common fold to other CXC chemokines, which has an N-terminal loop, an anti-parallel beta sheet, and a C-terminal α-helix [6, 10], in addition, the N-terminal loop of CXC chemokines is known to be deterministic in receptor selectivity however homologies between these chemokine proteins are low [13]. Using CXCR2, CXCR1, IL-8, and CXCL5, comparison studies can be made in the context of the full length receptors and the chemokines elucidating the origin of ligand preference in the receptors.

Examples of biophysical studies of the full length CXCR2 protein has been lacking, but examples of the protein behaviors can be found on other GPCR proteins. First and foremost, its closest relative CXCR1 has been extensively studied with biophysical techniques, including a structure deposited in the protein data bank [14-16]. There are also features that are common to all GPCRs, for example, it is known that the activation of the GPCRs triggers major conformational changes in the transmembrane helices number 5-7 [17], which is accompanied by the activation of the G proteins. Similarities and differences has been found in their conformational dynamics in this process [18]. For example, the dynamics of β_2-adrenergic receptors has been studied with single molecule FRET, which measured its correlation time scales to a range from nanoseconds to milliseconds [19]. This means ensemble studies have to either capture the GPCR in a distinctive conformation like the case in x-ray crystallography or deal with the existence of dynamical conformations. GPCRs are also allosterically regulated by ligands, ions, and lipids [20-22]. This highlights the differences sample environment can exert on the obtained results. Structural studies of the GPCRs has been complicated by the dynamics and sample environments. In recent studies, unmodified GPCR metabotropic glutamate receptors (mGlus) embedded in MSP1D1 Nanodiscs [23]. Mutation free structures were obtained in native bilayer environments using Cryo-EM. Moreover, recent studies of cryo-EM heterotrimeric G proteins complex were also important advances in biophysical studies of the GPCRs [24]. Compared to the explosive growth of cryo-EM in the decade, NMR spectroscopy has seen gradual developments in the structural biology of large protein complexes because of the obstacles in sample preparations, spectroscopy, and data processing. This study presents initial data on the NMR spectra of CXCR2, laying down the first of the studies of the full length CXCR2 with protein NMR spectroscopy.

Using NMR, mobility of the parts of CXCR2 were determined using solution state nuclear magnetic resonance (NMR) spectroscopy. The size of the GPCRs can be difficult for protein NMR using solution state techniques. As more native-like lipid bilayer environments are adopted to study GPCRs in native states, their particle size become larger and molecular tumbling become slower resulting in broader line-widths for the proteins in solution NMR. Here a smaller version of the membrane scaffolding protein MSP1D1ΔH5 was used for NMR studies. The protein was developed for solution NMR spectroscopy and was shown to assemble nanodiscs with diameter less than 10 nm [25]. Success, was also achieved on a GPCR using MSP1D1ΔH5 nanodiscs containing the neurotensin receptor 1 (NTR1) protein and DMPC/DMPG lipids. The NTR1, however, was extensive mutated [26].

To study the GPCRs, native and stable lipid bilayer environments are essential. On the other hand, whether lipid bilayer environment are compatible with different biophysical techniques also needs to be taken into considerations. Micelles and liposomes are basic tools to study membrane proteins in NMR spectroscopy, there are disadvantages for these systems. Micelles are convenient and small, the detergents in micelles can prevent protein aggregation by masking the hydrophobic parts of the proteins, and in many cases it is also an important initial step in membrane protein extraction [27, 28]. Detergents, however, do not provide a native bilayer environment for the solubilized membrane proteins, thus protein structure in micelles can be different from that in lipid bilayer environments. Moreover, the detergents used can also interact with non-transmembrane regions of the protein, and can partially or completely disrupt the structure and function of the protein. Many GPCRs are found to be active in non-ionic detergents such as dodecylphosphocholine (DPC), or n-dodecyl-B-D-maltoside (DDM). Others are found to be active, but with measurable differences in ligand binding or G protein activation [29]. Since early studies showed that detergents and lipids can be found stably bound to GPCRs in crystal structured, lipids are known to be essential for the structural integrity of these proteins [30]. Not-surprisingly, given that different lipids are now known to allosterically regulate GPCRs [31], significant differences are found when detergent incorporated GPCRs are compared to the liposome incorporated counterparts [32].

Liposomes on the other hand has the disadvantage that only one side of the GPCR embedded theoretically would be accessible to ligands or G-proteins. As a result, lipid bilayer disks contain both the lipid bilayer environment, and accessibility on both sides have made experiments easier. These include high density lipoprotein (HDL) disks [33] and nanodiscs [34]. The accessibility feature for these disk/discs is especially desirable because GPCRs bind to their ligand on the extracellular side, while activates the heterotrimeric G-protein on the intracellular side. Here, various membrane bilayer technologies was experimented on the CXCR2 protein. NMR spectra obtained for CXCR2 in each lipid bilayer system are presented here.

Bicelles are important methods for constructing a bilayer disc. The bilayer forming lipids such as 1, 2-dilauroyl-sn-glycero-3-phosphocholine (DLPC), 1,2-dimyristoyl-sn-glycero-3-phosphocholine (DMPC), 1,2-dipalmitoyl-sn-glycero-3-phosphocholine (DPPC), and etc. was mixed with detergents such as 1,2-dihexanoyl-sn-glycero-3-phosphocholine or C6:0PC (DHPC) [35] and triton X-100 [36] to form bicelles. Bicelles are lipid bilayer particles stabilized by the detergents on the edges to mask the highly hydrophobic acyl chains. Typical bicelles used for studying membrane proteins are highly dynamic and goes through phase transitions at both low temperature (isotropic to gel phase), and high temperature (gel phase to liquid crystalline phase). There are, however, different bicelle recipes which has different phase transition properties. Large bicelles exists as discoidal structures with lipid bilayers at temperatures below the lipid phase transition temperature [37]. When the lipid to detergent ratio q of bicelles gets smaller, the bicelles size get smaller and the signature ^{31}P spectrum for the phospholipid head group become isotropic for NMR spectroscopy [38]. For the studies of CXCR2, small and large bicelles were both used. The small bicelles are advantageous for the study of mobile residues, while the large bicelles were more suitable for observation of the relatively immobile transmembrane domains. The large bicelles can be magnetically aligned under the influence of the external magnetic field [35]. The system can be utilized to observe proteins embedded in the bicelles [39]. Since the earliest studies by Howard and Opella (1996), many proteins have been studied when aligned in the bicelle environments, these includes the GPCR CXCR1.

Nanodiscs was also used in NMR studies as well as functional assays for the CXCR2 protein. The membrane scaffolding protein or MSP was originally derived from the ApoI protein in human. Compared to the bicelles, the MSP-nanodiscs are not dynamic systems, for there is no apparent phase transitions at high temperatures and high concentrations, and when the MSP protein dissociates from the bilayers, the consequential precipitation of the bilayer membrane components is irreversible. The formed nanodiscs are very stable, and can be stored at 4 ^{o}C for long peroids of time. In addition to MSP1D1ΔH5 belt protein assembled nanodiscs, polymers can also be used in the same purpose. Polymers like the styrene-maleic acid (SMA) and the diisobutylene-maleic acid (DIBMA) also makes small size discs [40-42]. Today, plenty of literature exist about these disc forming polymers and their applications in membrane protein studies. Together, these new methods represent great opportunities today for the study of different aspects of membrane proteins, especially large membrane proteins such as the CXCR2 using biophysical techniques.

The binding constant of IL-8 to CXCR1 and CXCR2 are both measured *in vivo* to be in the lower nanomolar range 0.5-3 nM with ^{125}I radio-ligand binding assays and fluorescence spectroscopy [43-45], the binding constant for CXCL5 to CXCR2 was measured to be 2.3 nM using ^{125}I radio-ligand assays [11]. Data in regards to the potency of CXCL5 and IL-8 for activation of CXCR1 and CXCR2 was reported by Ahuja and Murphy (1996) [9]. In the study, the EC_{50} of IL-8 for both CXCR1 and CXCR2 was measured to be 4 nM while the EC_{50} of CXCL5 for CXCR1 was measured to be 40 nM compared to 10 nM for CXCR2. These results suggest CXCL5 is a less potent agonist for CXCR1 [9]. Moreover, studies in by Ahuja and Murphy (1996) also presented data of radio ligand binding between CXCR1 and CXCL5 and found levels of specific binding estimated to be larger than 0.5 μM through competition assays against IL-8 [9]. A different study at the same time also estimated affinity of CXCL5 for CXCR1 to be larger than 0.3 μM [11]. These data strongly suggest the selectivity bias of CXCR1 for IL-8 compared to CXCL5, and on the other hand the relative lack of selectivity of CXCR2 for IL-8 or CXCL5. Early *in vitro* studies of the receptors focusing on isolated CXCR1 N-terminal domain has found that it is structured in DPC micelles and do not exist as a random coil. In the study CXCR1 N-terminal peptide was found to have strong binding to IL-8 but only binds CXCL1 in micelles [46]. Since N-terminal domain of CXCR1 and CXCR2 were believed to be ligand selective [21] and necessary for receptor activation [47, 48]. Comparisons of N-terminal domain of CXCR2 and CXCR1 was carried out. Mapping of the IL-8 interaction sites on the N-terminal domain of CXCR1 has yielded results showing multiple changes in CXCR1 residue 10, 16, 18, 19, 23, 26, 27, 31 and 33 measured by the perturbation of the resonances in the heteronuclear single quantum coherence (HSQC) spectra of the CXCR1 N-terminal peptide [49]. This results suggest the binding of IL-8 induces changes in almost the entire N-terminal domain of CXCR1. It is also known that other parts of the receptor such as CXCR1 and CXCR2 also binds to chemokine proteins [13, 50]. Here using NMR methods, the relative mobility of the terminal domains of CXCR2 is characterized in the full length receptor. This is also the first example of biophysical studies of the highly purified full length CXCR2 receptor and its interactions with chemokine ligands.

5.2 Materials and Methods

Protein Purification

Codon optimized DNA sequence for the human CXCR2 protein (www.genscript.com) was cloned into pGEX plasmid between the thrombin cleavage sites and the c-terminal stop codon. The resulting plasmid was transform into BL21 competent cells (www.neb.com). A single colony was selected for the 10 mL LB starter culture for 8 hours, and 0.1 mL of the culture was transferred to 50 mL M9 media supplemented with ^{15}N enriched ammonium sulfate and/or ^{13}C enriched glucose for overnight growth. In the case for ^{15}N enriched and ^{13}C natural abundant samples, 1 g of ^{15}N ammonium sulfate and 2% glucose was supplemented. In the case for ^{15}N, ^{13}C double labeled sample, 1 g of ^{15}N ammonium sulfate and 1 g of ^{13}C glucose was used. All isotopes were obtained from Cambridge isotope laboratories (www.isotope.com). The 50 mL culture was then transferred into 500 mL culture until O.D. at 600 nm wavelength reaches 0.5. Then protein production was induced with 0.1 mM IPTG. The purification methods then follows the published protocols for CXCR1 [3, 14, 51] except for the dialysis procedures after addition of 10:1 weight ratio of lipid to protein content. Temperature regulation at 23-25^{o}C with a fish tank temperature regulator was included for the detergent dialysis of CXCR2. For the dialysis, specifically with a 1:100 volume ratio dialysis against 20 mM HEPES pH 7.4 for the first dialysis (16 hours), against 20 mM HEPES pH 7.4 20 mM KCl for the second dialysis (8-16 hours), and 20 mM HEPES pH 7.4 60 mM KCl for 3-5 more dialysis (8-16 hours each). N-terminal peptide of CXCR1 was purified based on established protocols [14].

Nanodisc incorporation of CXCR2 follows the published protocols [25, 52] using the molar ratios of protein: lipid: MSP1D1ΔH5 (1:400:10), and SDS dialysis was carried out using dialysis against 20 mM HEPES pH 7.4 following the same procedures shown above. Size exclusion chromatography was carried out in 20 mM HEPES pH 7.4, 50 mM NaCl buffer using a HiLoad 16/60 superdex 200 column. All CXCR1 constructs were purified with established protocols [3, 14, 51].

Codon optimized DNA sequence of CXCL5 (www.genscript.com) was cloned into the Ptrc vector along with the fusion partner thioredoxin (trx). pTRC-LIC was a gift from Cheryl Arrowsmith (Addgene plasmid # 62343). A thrombin cleavage site was added between Trx and CXCL5. Sequencing was performed with the pBad reverse primer to confirm the sequence of the plasmid. Plasmid was transformed into NEB Shuffle Express cells at 30^oC grown for at least 24 hours on an agar/carbenicilin plate. A single colony was inoculated into a tube of 15 mL LB media shaked at 30^oC for at least 14 hours. 100 μL of the LB overnight media was transferred to 50 mL M9 media and subsequently grown for at least 20 hours at 30^oC. When O.D. at 600 nm wavelength reaches 0.8-0.9, culture was induced with a final concentration of 0.2 mM IPTG. Centrifugation was used to pellet cells. Cell pellet for 1 L worth of media was re-suspended in 50 mL lysis buffer containing 0.3M NaCl and 20mM Tris-HCl pH7.45, 60 mg of lysozyme, and 40 units of DNAse I (www.neb.com). A total of 4 freeze thaw cycles were performed in liquid nitrogen and 40^oC water bath. Lysate solution was treated with polyethylenimine (PEI) (www.sigmaaldrich.com) (final concentration 0.2% v/v). Then, treated solution was incubated on ice for 30 mintues. After incubation, precipitated DNA and cell debris were pelleted at 40K rpm for 40 minutes, supernatant was then placed in a 100 mL beaker with

30 g AMS added progressively to precipitate proteins. Protein was pelleted at 20K rpm for 30 minutes. Binding buffer with pH 8.0 containing 0.3 M NaCl, 20 mM Tris-HCl, and 20 mM Imidazole was used to gently re-suspend the pellet. Binding buffer solubilized protein was filtered with 0.22 μm filter (www.emdmilipore.com), and flown through the Ni-NTA column for 4 times. Alternatively lysate was not treated with PEI but instead subject to treatment in a glass-dounce homogenizer to shear the viscous DNA. The resulting solution was then centrifuged at 40 K rpm for 40 minutes at 4^{o}C, and the resulting supernatant was loaded onto a Biorad G-25 column packed with Ni-NTA (Nickel Nitrilotriacetic acid) agarose resin (www.qiagen.com). Column was washed with 0.3 M NaCl, 20 mM Tris-HCl pH 8.0, 30mM Imidazole for 20 column volume of wash buffer. 400 units per liter of bacterial culture pallet of bovine serum thrombin was added to the column to allow enzymatic cleavage at room temperature for 4 hours or 4^{o}C for 20 hours. Trifluoroacetic acid (TFA) was added to the flowthrough of the Ni-NTA column, to a final concentration of 0.1%. The solution was then injected onto a C18 column, for reverse-phase HPLC separation using a water/acetonitrile gradient. Alternatively the solution can be injected onto a C4 column, for reverse-phase HPLC separation using a water/trifluoroethanol-isopropanol gradient. The eluted protein was dried with dry N_2 gas to remove the organics, lyophilized, and then re-dissolved in 20mM HEPEs, pH 6.0 or pH 7.5 until further use.

IL-8 samples were prepared according to published protocols [49, 53]. IL-8 and IL-8 (1-66). In both CXCL5 and IL-8 purification, the histidine affinity tag stays with the thioredoxin fusion protein after enzymatic cleavage. The cleavage was designed to leave no additoinal residues in the chemokine proteins.

ELISA assay

Empty Nanodisc with uncleaved MSP1D1ΔH5 was diluted in 20mM HEPES, pH 7.5. CXCR2 Nanodisc with cleaved MSP1D1ΔH5 in diluted in 20mM HEPES, pH 7.5. PBST buffer was prepared by adding 0.01% Tween20 (www.abcam.com) to PBS solution. Blocking solution was made with 2% BSA and 1% Casein in PBS (10-20mL). Anti IL-8 anti body was obtained from Biolegend (biolegend.com) and diluted in PBST with 4% BSA (Sigma A2934). The exact product number of BSA was important for obtaining good blocking results. Streptavidin-HRP (STREP-HRP) and TMB solution were obtained from ThermoFisher (thermofisher.com). 100 μL of 20mM Nanodiscs were coated onto wells of the 96-well Nunc ELISA plate (thermofisher.com) at 4ºC overnight. Each sample was duplicated. The wells were washed with 300 μL of PBS three times with 5 minutes waiting time each. Then wells were blocked with 200 μL of blocking solution for 4 hours at room temperature. Wells were then washed three times with PBST using 300 μL buffer. IL-8 or CXCL5 were incubated in each wells for 4 hours at room temperature in 20 mM HEPES. With a total of 100 μL volume the concentration of the chemokines range from 0 nM - 3200 nM. Wells were then washed with PBST three times each with a 5 minutes incubation. A 1:500 antibody dilution in PBST was added to each well (100uL/well) with 1 hour incubation. Wells were washed three times with PBST each with a 5 minutes incubation. A 1:800 dilution of STREP-HRP in PBST was added to each well (100uL/well) with 1 hour incubation. Wells were washed three times with PBST each with a 5 minutes incubation. 50uL TMB was added to each well with 10 minutes -15 minutes incubation time for color development. Then 50 μL of 0.16 M H_2SO_4 was added to each well to stop the reaction. Readings from 450 nm and 550 nm was collected and subtracted to obtain the final results. The curves were fitted with the Hill equation using the SciDAVIS software (scidavis.sourceforge.net).

NMR Samples

CXCR1 and CXCR2 isotropic bicelle samples were prepared following established protocols [14, 51]. Aligned CXCR2 q=3.2 bicelle samples were prepared following established protocols [51]. MAS solid-state NMR sample for CXCR2 in liposomes were prepared based on established protocols [3]. The assembled MSP1D1ΔH5 nanodisc sample were concentrated using an Amicon 30 kD molecule weight cutoff centrifuge concentrator for NMR. SMA 3:1 (SL 25010 P20) was provided by polyscope (http://www.polyscope.eu), and DIBMA was obtained from Anatrace (www.anatrace.com). The SMALPs and DIBMALPs samples contain 1:4 weight to weight ratio of lipid to SMA and lipid to DIBMA polymer respectively. The polymers were mixed with proteoliposome containing CXCR2 at pH 8.0 with 1 mL volume. Then the protein containing nanodiscs were purified using Ni-NTA resin. The binding and washing buffer contains 0.5 M NaCl and 20 mM Tris-HCl pH 8.0. The elution buffer contains 0.5 M NaCl, 20 mM Tris-HCl, pH 8.0 and 0.5 M Imidazole. The eluted protein was dialyzed in 20 mM HEPES pH 8.0 and concentrated in an Amicon 50 kD molecule weight cutoff centrifuge concentrator to make NMR samples. The SMALPs sample was kept at pH 8.0 while the DIBMALPs sample was adjusted to pH 5.0.

Solution NMR spectroscopy

Solution NMR spectra, including the CXCR1 N-terminal titration spectra, of CXCL5 was acquired at ^{1}H frequency of 600 MHz at 25^{o}C. Solution NMR spectra of CXCR2 was acquired at ^{1}H frequency of 800 MHz at 50^{o}C. The MSP1D1ΔH5 nanodisc spectrum was acquired at 800 MHz ^{1}H frequency at 40^{o}C, SMALPs nanodisc spectrum was acquired at 800 MHz ^{1}H frequency at 4^{o}C, and DIBMALPs nanodisc spectrum was acquired at 800 MHz ^{1}H frequency at 50^{o}C. Titration experiments of proteoliposomes and CXCL5 and IL-8 (1-66) were carried out at 600 MHz ^{1}H frequency. To equalize the total lipid in the proteoliposome titration experiments, empty DMPC liposomes were made using the lipid film resuspension method and mixed with different protein containing proteoliposomes. Competition experiments were acquired at 800 MHz ^{1}H frequency.

Titration of CXCR1 N-terminal domain to CXCL5 was carried out at 25^{0}C where concentrated CXCR1 N-terminal domain was added to CXCL5 gradually. The resulting CXCL5 concentration was adjusted based on volume change. Solution NMR assignments of CXCL5 was transferred from literature [10]. The heteronuclear single quantum coherence (HSQC) spectrum was acquired at 600 MHz ^{1}H frequency.

Solid-state NMR spectroscopy

Magic angle spinning (MAS) solid-state NMR spectrum of CXCR2 proteoliposome was acquired at 750 MHz ^{1}H frequency at 4^{o}C, and 10 kHz magic angle spinning speed, using a 50 msec proton driven spin diffusion (PDSD) mixing time. Aligned bicelle sample of CXCR2 was acquired at 700 MHz ^{1}H frequency, at 40^{o}C, using 50 kHz ^{1}H and ^{15}N B_1

on a homebuilt ^{1}H-^{15}N MAGC (modified alderman grant coil) –solenoid double resonance cross coil probe [54]. NMR data processing was performed in Topspin (www.bruker.com), NMRpipe [55], NMRFAM-SPARKY [56], and chemical shift perturbation mapping was made using UCSF chimera [57].

5.3 Results

Purification of CXCR2 and CXCL5

Purification of CXCR2 and CXCL5 yields pure protein as seen by their SDS-PAGE gel in Figure 5.2. In Figure 5.2B CXCR2 incorporated MSP1D1ΔH5 nanodiscs is seen containing an additional band for the MSP1D1ΔH5 belt protein and also showing the relative ratio of the two proteins in nanodiscs. The size exclusion chromatogram of the formed nanodiscs is shown in Figure 5.2C showing the expected size and size distribution of the small nanodiscs containing CXCR2. Additional purified CXCR2 constructs with different truncations are shown in Figure 5.2D. ELISA assays in Figure 5.3 were used to demonstrate the binding of CXCL5 and IL-8 to CXCR2 and based on approximate curve fitting, the binding of CXCR2 and the two ligands are estimated to be in the nanomolar range.

Figure 5.2 Purification of monomeric CXCR2-WT into (A) proteoliposomes and (B) MSP1D1ΔH5 nanodiscs. (C) Size exclusion chromatography chromatogram of CXCR2 nanodisc using Superdex200 Hiload 16/60 column using a flow rate of 0.7 mL/min. (D) Purification of 4 constructs of CXCR2 monomers (from left to right): CXCR2-WT (1-360), CXCR2-ΔN (32-360), CXCR2-ΔC (1-329), and CXCR2- ΔNC (32-329). The bands are arranged in descending order from left to right. (E) Purification of the CXCL5 protein. Lane 1 is the mark 12 protein maker, lane 2 is the solubilized fraction of the cell lysate after centrifugation, lane 3 is the Ni-NTA column flowthrough, lane 4 is the fraction that bound to the Nickel resin after on-column thrombin cleavage, lane 5 is the eluted CXCL5 after thrombin cleavage and thrombin, lane 6 is the rp-HPLC purified CXCL5 rehydrated in 20mM HEPES, pH 7.5. (F) Two dimensional HSQC spectrum of ^{15}N enriched CXCL5 including the backbone N-H and the side chain regions.

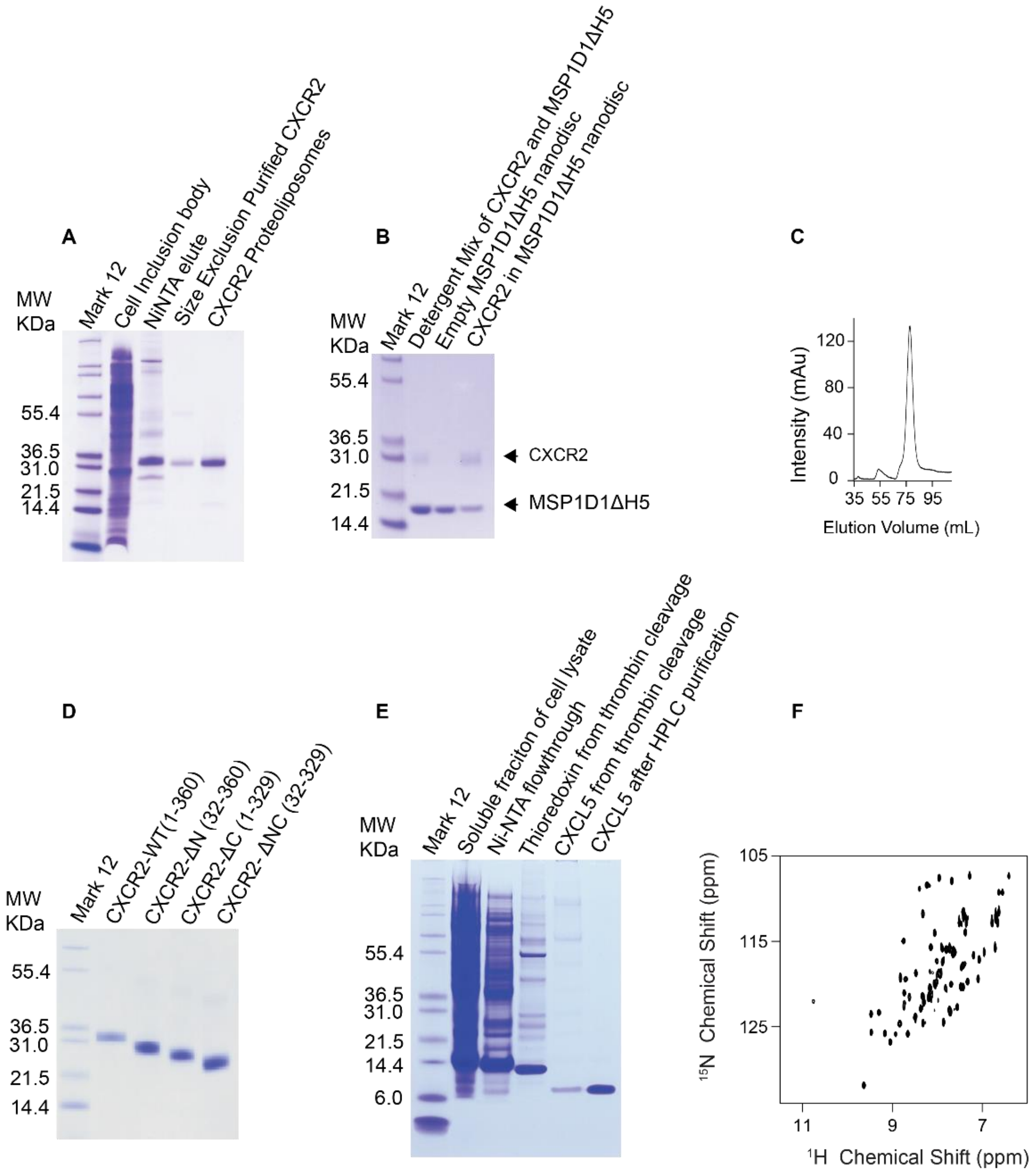
A
MW KDa
Mark 12
Cell Inclusion body
NiNTA elute
Size Exclusion Purified CXCR2
CXCR2 Proteoliposomes
55.4
36.5
31.0
21.5
14.4
B
MW KDa
Mark 12
Detergent Mix of CXCR2 and MSP1D1ΔH5
Empty MSP1D1ΔH5 nanodisc
CXCR2 in MSP1D1ΔH5 nanodisc
55.4
36.5
31.0
21.5
14.4
CXCR2
MSP1D1ΔH5
C
Intensity (mAu)
120
80
40
0
35
55
75
95
Elution Volume (mL)
D
MW KDa
Mark 12
CXCR2-WT(1-360)
CXCR2-ΔN (32-360)
CXCR2-ΔC (1-329)
CXCR2- ΔNC (32-329)
55.4
36.5
31.0
21.5
14.4
E
MW KDa
Mark 12
Soluble fraciton of cell lysate
Ni-NTA flowthrough
Thioredoxin from thrombin cleavage
CXCL5 from thrombin cleavage
CXCL5 after HPLC purification
55.4
36.5
31.0
21.5
14.4
6.0
F
15N Chemical Shift (ppm)
105
115
125
11
9
7
1H Chemical Shift (ppm)

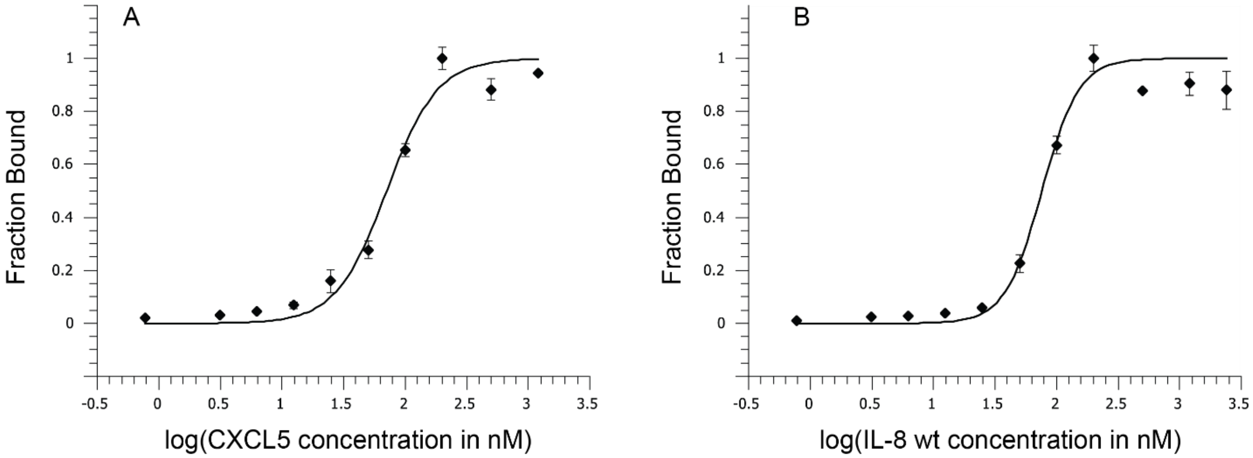

Figure 5.3 Elisa experiments showing ligand binding (A) CXCR2 in MSP1D1ΔH5 nanodisc binding with CXCL5. (B) CXCR2 in MSP1D1ΔH5 in nanodisc binding with IL-8 wt. Error bars are calculated from sample duplicates.

Solid-State NMR studies of CXCR2 in lipid bilayers

Solid-state NMR spectroscopy was used to examine the condition of the CXCR2 protein purified into proteoliposomes. A two-dimensional ^{13}C-^{13}C correlation spectrum was acquired under the magic angle spinning conditions, the observation of abundant cross peaks in Figure 5.4 suggest the purified CXCR2 protein is folded. In addition, using the oriented (OS) sample solid-state NMR method, CXCR2 in DMPC/DHPC bicelles can be magnetically aligned in the magnetic field. The acquired spectrum shown in Figure 5.5 suggests that the purified protein is not aggregated, signified by the lack of a powder pattern.

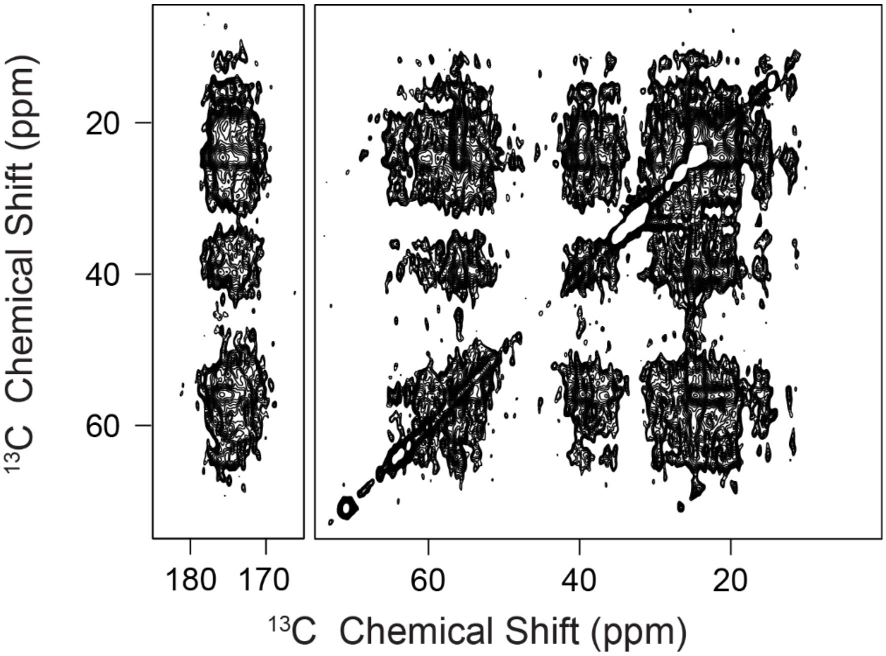

Figure 5.4 Selected sections of the ^{13}C-^{13}C correlation spectrum of ^{13}C, ^{15}N enriched CXCR2 WT (1:10 (wt/wt) protein/DMPC) proteoliposome at 4^{o}C, 10 kHz MAS, 50 msec PDSD mixing showing all of the ^{13}C resonances from CXCR2 and all of their through space correlations due to ^{13}C-^{13}C dipolar interactions.

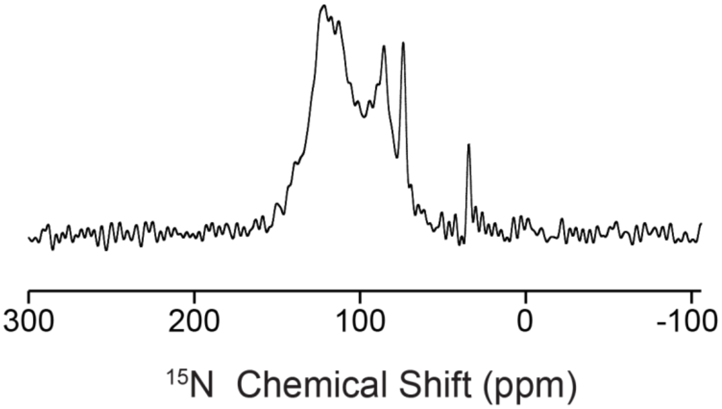

Figure 5.5 Cross-polarization mismatch optimized IS transfer (CP-MOIST) spectrum of CXCR2 (1-360) in q=3.2 DMPC/DHPC bicelle, at 38^{o}C, pH7.4.

Solution NMR of CXCR2 in different membrane mimetic systems

There are mobile residues in CXCR2 that can be studied with the solution NMR method. These residues are expected to be located at the termini of the protein. It can be seen by comparison with Figure 5.7A that the DMPC/DHPC bicelle system provides more well-resolved NMR resonances, however, they present a different spectral pattern compared to the different nanodisc samples. The different nanodiscs have similar to each other but not identical spectral patterns. Based on sequence alignment of CXCR1 and CXCR2 shown in Figure 5.1, the expected N-terminal domain of CXCR2 is predicted to be 48 residues long, and the expected C-terminal domain of CXCR2 is predicted to be 42 residues long. The counting of 31-35 residues in nanodisc samples of CXCR2 suggest that not all of the terminal domain of CXCR2 in native bilayer environments are mobile.

Solution NMR spectra in bicelle shown in Figure 5.6 demonstrates the relative mobility of the residues in the N-terminal and C-terminal domains by comparing the full length protein to the different truncated mutants. These sets of experiments uses DMPC/DHPC bicelles to allow observation of well resolved resonances for the terminal signals of CXCR2. Overall, a large portion of the N-terminal domain residues is not visible in solution NMR spectra. This is seen based on comparisons within Figure 5.6 (A, B, C, and D) where Figure 5.6 A and B share the most visual resemblance Indicating that most of the spectrally dispersed resonances in Figure 5.6 A belongs to the C-terminal domain of the protein. Figure 5.6 C and D also share many resonances indicating that most of the resonances seen in Figure 5.6 C belongs to the remaining resonance in the N and C-terminal domain of the CXCR2 receptor. Moreover, when the number of resonances are counted in Figure 5.6, the number of resonances from CXCR2 (1-360) is 68, from CXCR2 (32-360) is 56, from CXCR2 (1-329) is 28 and from CXCR2 (32-329) is 25. Since all the CXCR2 constructs contain additional an N-terminal Glycine, a Serine and six C-terminal Histidine residues, 7-8 common residues to the four spectra in Figure 5.7 can be subtracted from the residue counts, yielding 60 residues for CXCR2 (1-360), 48 residues for CXCR2 (32-360), 20 residues for CXCR2 (1-329), and 17 residues for CXCR2 (32-329). The differences in residues suggest less than 12 residues in CXCR2 N-terminal domain is mobile, and less than 40 residues in the CXCR2 C-terminal domain is mobile. The remaining 17 residues as a result of double truncation is only 3 residues less than that of CXCR2 (1-329) suggesting the truncation of the structured residues in the termini mobilizes additional residues these domains.

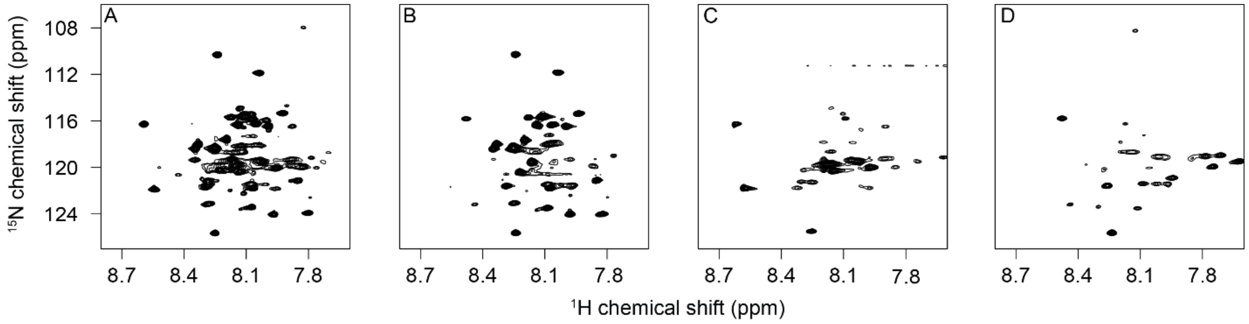

Figure 5.6 Different CXCR2 constructs in q=0.1DMPC/DHPC bicelle at pH4.0 and 50°C shown with high contour levels to present all the resonances. (A) CXCR2-WT (1-360). (B) CXCR2-ΔN (32-360). (C) CXCR2-ΔC (1-329). (D) CXCR2- ΔNC (32-329).

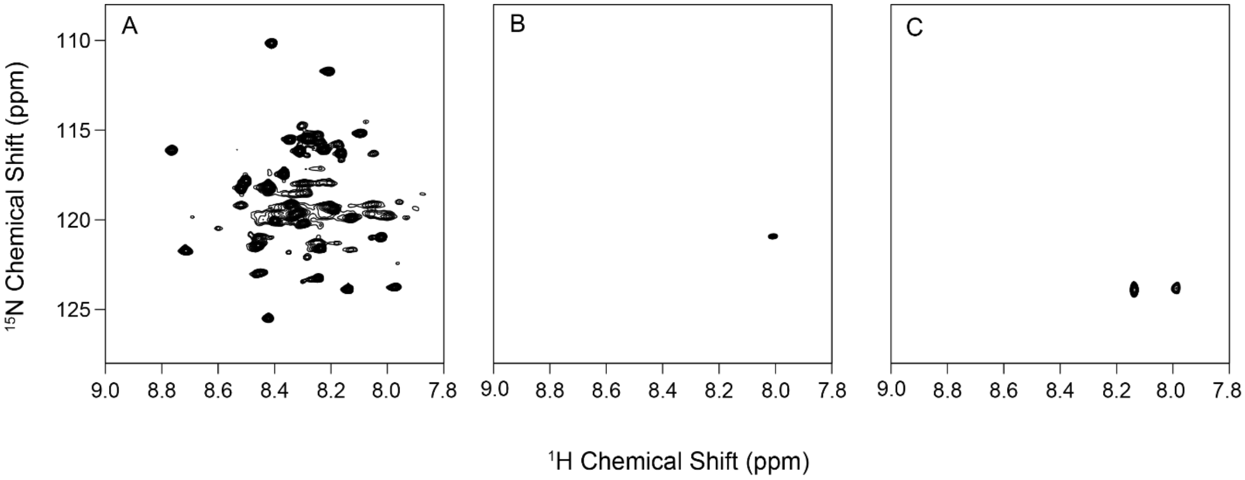

Figure 5.7 HSQC spectra of CXCR2-WT (1-360) in q=0.1DMPC/DHPC bicelle at pH4.0 and 50°C shown with similar contour levels for all three spectra. (A) Uniformly ^{15}N enriched protein. (B) ^{15}N Leucine selectively labeled protein. (C) ^{15}N Valine selectively labeled protein.

In an attempt to partially assign the CXCR2 termini, amino acid selectively labeled samples were made that enriches only the leucine or valine amino acids, the HSQC spectra of bicelle samples were acquired for the leucine and valine labeled samples. The results in Figure 5.7B shows two resonances that can be attributed to leucine while in Figure 5.7C, only one resonance can be attributed to valine. Additional weak resonances in the spectra for selectively labeled samples was seen and can be due to isotopic scrambling as a result of amino acid interconversions during cell growth. There are 2 leucine and 0 valine in 1-31 region of the N-terminal domain, and 3 leucine and 1 valine, in the 330-360 region of CXCR2 C-terminal domain, and in the full length CXCR2, there are 65 leucine and 25 valine. The absence of most of the leucine and valine in solution NMR spectroscopy again suggests that most of the protein remain immobile. Combining the information obtained in Figure 5.7 and 5.8, it can be determined that the two leucine resonances in Figure 5.8 B can also be found in Figure 5.7 A and B but not in C and D. Therefore, the two leucine residues in the NMR spectra are form the C-terminal domain of CXCR2. The same reasoning can be made for the valine residue in Figure 5.8 C that it belongs to the C-terminal domain of CXCR2. Since only one valine is in the 330-360 region, the strong resonance at 8.0 ppm (^{1}H chemical shift) and 128.9 ppm (^{15}N chemical shift) can be assigned to valine 349. Since only three leucine residues are in the 330-360 region the resonances in Figure 5.8 B can be attributed to two of the three leucines at position 334, 340 and 360, but exact assignments are not known. The first leucine residue in the N-terminal domain of CXCR2 is leucine 20, and since this residue is absent from the solution NMR spectra. It is additional evidence supporting the immobility of the N-terminal domain of CXCR2 around residue 20.

CXCR2 was incorporated into different nanodiscs to for solution NMR. However, despite optimization, solution NMR HSQC spectra of these small discs samples yielded less than 40 resonances for the full length protein. Different pH and temperatures were used for MSP1D1ΔH5 nanodiscs (35 resonances), SMALPs nanodiscs (31 resonances), and DIBMALPs nanodiscs (31 resonances). In all cases more than 300 residues of CXCR2 were absent from the two-dimensional spectra (Figure 5.8).

A similar comparison of the CXCR2 (1-360) and CXCR2 (32-360) in MSP1D1ΔH5 nanodiscs results in 16 resonances difference, shown in Figure 5.9A and Figure 5.9B. If the additional glycine and serine from the N-terminus are subtracted from the count, 14 resonances for the mobile N-terminal end in MSP1D1ΔH5 nanodiscs is found to be mobile. In the nanodiscs samples the CXCR2 C-terminal domain, the 4 additional resonances around 117 ppm (^{15}N), 8.2 ppm (^{1}H) appeared as a result of N-terminal truncation. Excluding the 4 resideus, only about 17 residues from the C-terminal domain of CXCR2 is mobile including the six added histidine residues. This result suggest under physiological conditions, large parts of the C-terminal domain of CXCR2 also remain immobile. By comparing the number of resonances in bicelles and nanodiscs for full length CXCR2, which contain much fewer resonances, it is likely that the observation of structured N-terminal domain in CXCR2 remains true in small nanodics of SMALPs and DIBMALPs.

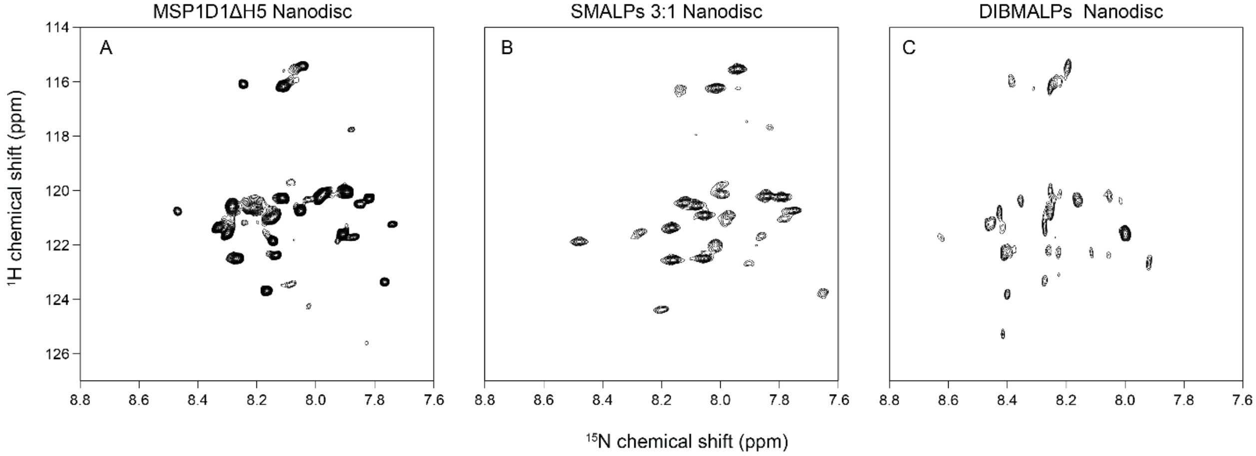

Figure 5.8 HSQC spectra of CXCR2 (1-360) in different membrane mimetic systems. (A) CXCR2 in MSP1D1ΔH5 nanodisc at pH 7.2 and 40°C. (B) CXCR2 in SMALPs 3:1 nanodisc at pH 8.0 and 4°C. (C) CXCR2 in DIBMALPs nanodisc at pH 5.0 and 50°C.

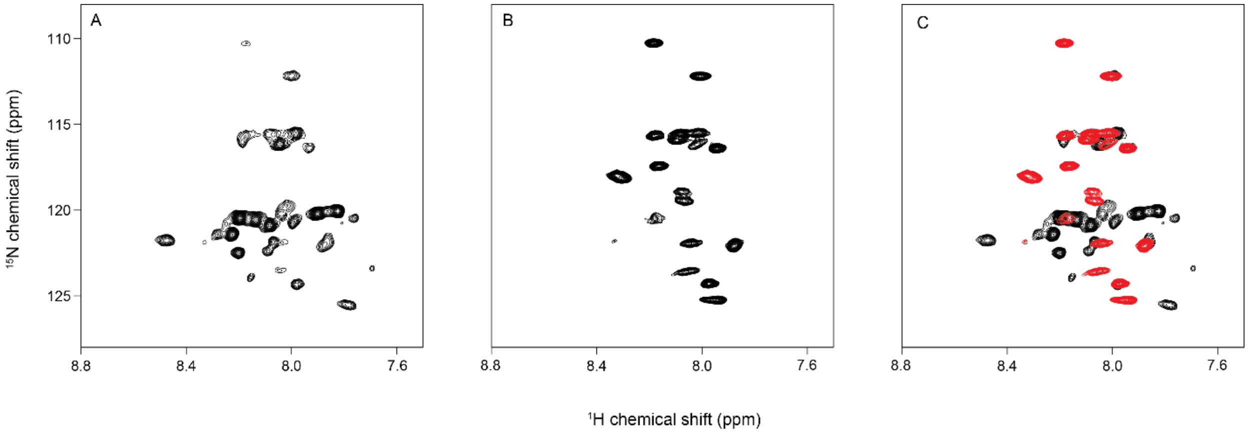

Figure 5.9 (A) HSQC spectrum of CXCR2 (1-360) in MSP1D1ΔH5 nanodisc at pH 7.4 and 25°C. (B) HSQC spectrum of CXCR2 (32-360) in MSP1D1ΔH5 nanodisc at pH 7.4 and 25°C. (C) is an overlay of (A) and (B).

Solution NMR studies of Chemokine immobilization by CXCR1 and CXCR2

The interaction between CXCR2 with its chemokine ligands was studied in the perspective of the chemokines. Due to their small sizes, all parts of their sequences are accessible to solution NMR. The purified ^{15}N enriched chemokine protein CXCL5 was observed using the HSQC experiment, the two dimensional HSQC spectrum in Figure 5.2F shows well dispersed resonances indicating proper folding of the protein. This spectrum also matches with the previously published NMR spectra for the CXCL5 protein [10].

The characterization of the binding between CXCR2 and CXCL5 was carried out between CXCR2 in DMPC proteoliposome under physiological conditions. Different molar ratios of un-enriched CXCR2 and ^{15}N enriched CXCL5 were mixed and the ^{15}N-edited ^{1}H spectra of the labeled CXCL5 was collected (Figure 5.10B). The binding between un-enriched CXCR2 and ^{15}N enriched IL-8 (1-66) was carried out in the same way (Figure 5.10A). IL-8 (1-66) is a monomeric construct of IL-8 [53], like CXCL5 or wild type IL-8 it has a 1:1 binding ratio to the receptors. In both spectra (Figure 5.10 A and B), chemical shift perturbation was not overserved. The titration of CXCR2 receptor containing proteoliposomes reduces CXCL5 and IL-8(1-66) signals from the NMR experiments indicating specific binding.

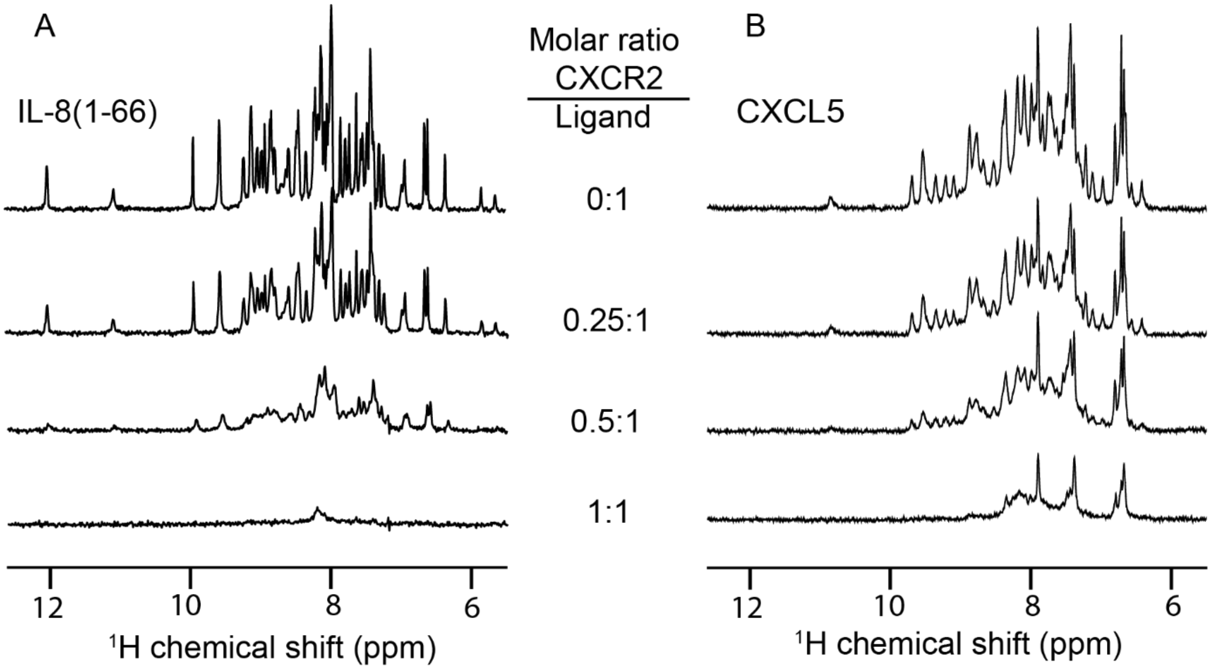

Figure 5.10 ^{15}N edited ^{1}H spectra of IL-8(1-66) and CXCL5 mixed with different amount of CXCR2 reconstituted in DMPC liposomes. Molar ratios ranges from 0:1 (CXCR2: Chemokine) to 1:1. (A) CXCR2 proteoliposome titrated with IL-8(1-66). (B) CXCR2 proteoliposome titrated with CXCL5.

Observation of binding of CXCL5 to CXCR1

The binding of CXCL5 and CXCR1 was observed in NMR binding experiments as well. Shown in Figure 5.11A, in equimolar ratio mixture of un-enriched CXCR1 proteoliposome and ^{15}N enriched CXCL5, the NMR signal of CXCL5 almost completely diminished from the spectrum. This suggest presence of binding between CXCL5 and CXCR1. To verify the previously observed ligand bias in CXCR1 [9], competition of un-enriched IL-8 (1-66) for ^{15}N enriched CXCL5 was carried out and the results were shown in Figure 5.10B. In this competition experiment, 1:1 molar ratio of un-enriched CXCR1 proteoliposomes were first added to ^{15}N enriched CXCL5 reducing the NMR signal of CXCL5 to noise levels. Then when unenriched IL-8 (1-66) was added, the CXCL5 NMR signal recovers. At 1:1 ratio of CXCR1 and IL-8 (1-66) the signal of CXCL5 recovers to 84%. If CXCL5 and IL-8 has similar Kd for CXCR1, competition may end up with about half of the signal recovery. For the CXCR1 to chemokine ratio would be 1:2. From Figure 5.11A -C it can be seen that at receptor to chemokine ratios of 0.5:1, the amount of chemokine bound is larger or equal to 50%. The fact that IL-8 (1-66) is able to compete for CXCL5 and recover more than 50% of the CXCL5 signal suggest IL-8 (1-66) binds to CXCR1 more strongly.

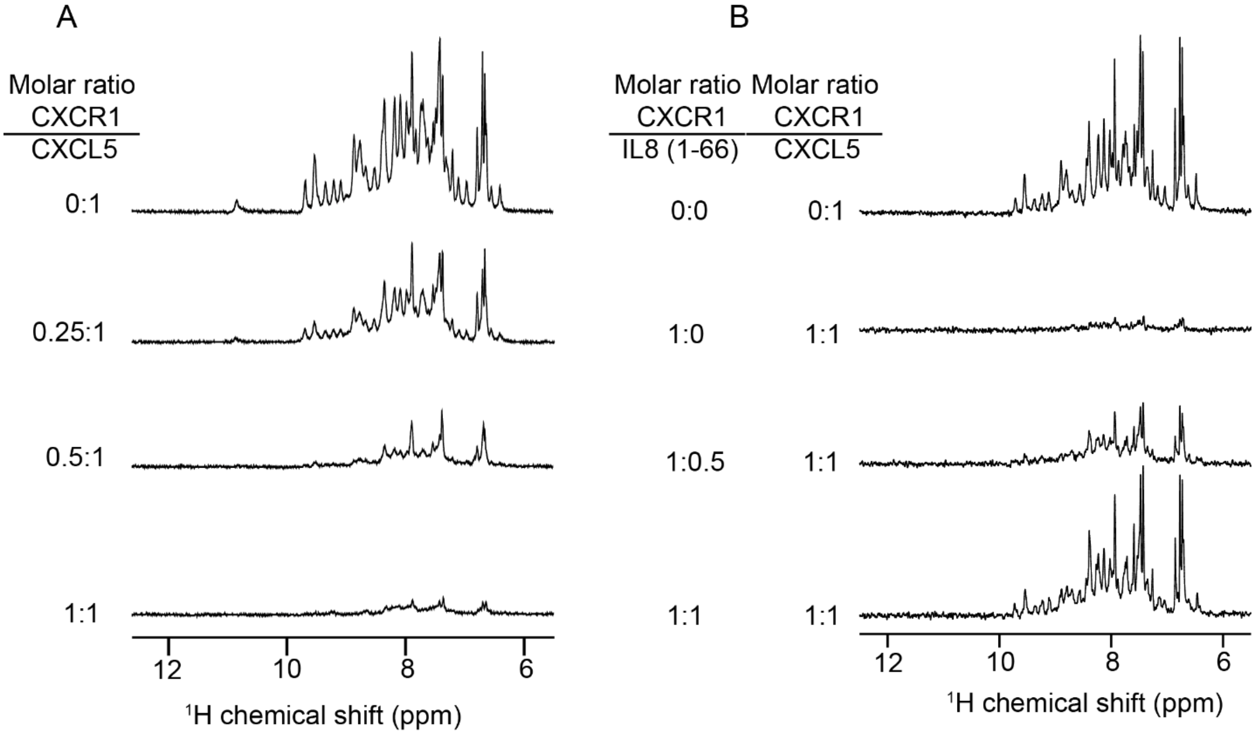

Figure 5.11 (A) ^{15}N edited ^{1}H spectra of CXCL5 mixed with different amount of CXCR1 reconstituted in DMPC liposomes. Molar ratios ranges from 0:1 (CXCR1:CXCL5) to 1:1. (B) ^{15}N edited ^{1}H spectra of CXCL5 mixed with 1:1 molar ratio of CXCR1 reconstituted in DMPC liposomes, and subsequently IL-8 (1-66). Molar ratios of CXCR1: IL-8 (1-66)) ranges from 1:0 to 1:1.

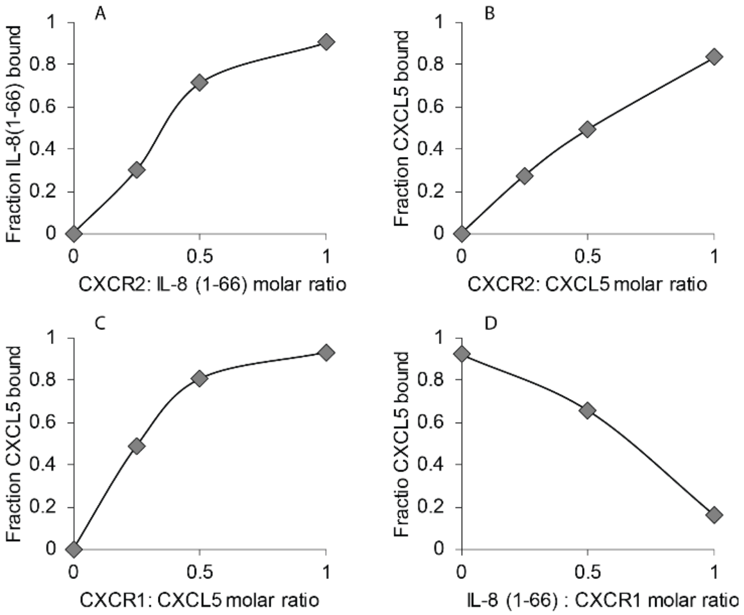

Figure 5.12 Percent chemokine bound calculated from Intensity measurements in Figure 5.10 and 5.11 versus molar ratios (A) Corresponds to 5.10A showing immobilization of IL-8 (1-66) by CXCR2. (B) Corresponds to Figure 5.10B showing immobilization of CXCL5 by CXCR2. (C) Corresponds to Figure 5.11A showing immobilization of CXCL5 by CXCR1. (D) Correspond to Figure 5.11B showing showing recovery of the immobilized CXCL5 by IL-8 (1-66). These comparisons demonstrates that IL-8 (1-66) competes with CXCL5 for CXCR1(1-350) and has a stronger affinity.

To further investigate the binding interactions between CXCR1 and CXCL5. The isolated N-terminal domain peptide of CXCR1 was chosen for the studies to allow observation of chemical shift perturbations (CSP). The results are shown in Figure 5.13A where a section of the two dimensional HSQC spectra during the titration of CXCR1 N-terminal domain to CXCL5 where resonances are shown moving in response to the increase in N-terminal domain of CXCR1 concentrations. Titrations stopped at 1:18.28 molar ratio where most of the CXCL5 chemical shift perturbation plateau. The calculated CSP is then presented in Figure 5.17B in yellow vertical bars overlay with the published data of CXCL5 CSP caused by CXCR2 N-terminal domain (in grey vertical bars) [58]. Significant differences are present in the comparisons. Residue 16-26 from the N-loop, and residue 52-55 from the β-sheet of CXCL5 are largely perturbed upon binding of CXCR2 N-terminal domain. This is in contrast to the isolated residues (18, 43, 44, 57, and 72) perturbed upon CXCL5 binding to CXCR1 N-terminal domain. The experimental data obtained here suggests weaker specificity of CXCL5 to CXCR1 N-terminal domain compared to CXCR2 N-terminal domain. The CSP quantified in Figure 5.13B is mapped onto the structure of CXCL5 shown in Figure 5.14 where the perturbed sites are coated in red.

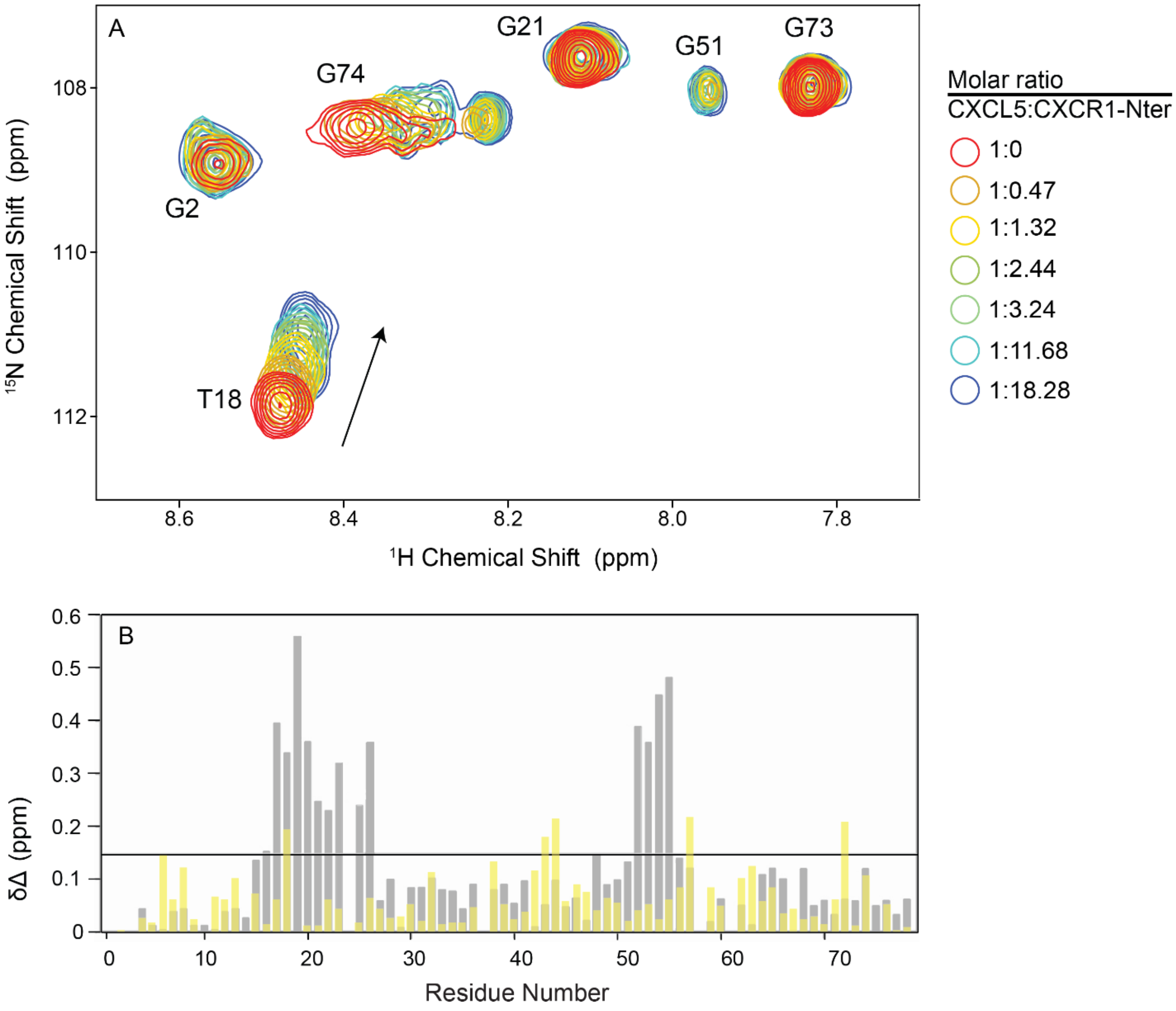

Figure 5.13 Titration of the CXCR1 N-terminal domain to ^{15}N enriched CXCL5. (A) Section of the two-dimensional HSQC spectra overlaid on top of each other. The spectra of different resonances correspond to each molar ratio of CXCL5 and CXCR1-Nterminal domains are color-coated from red (no CXCR1 N-terminal peptide) to blue (saturated with the N-terminal peptide). (B) The calculated chemical shift perturbation from the titration experiments of CXCR1 N-terminal domain to uniformly ^{15}N enriched CXCL5 (yellow bars). The residues T18, E43, V44, D57, and D72 are seen above the 0.15 chemical shift change (δΔ) scale shown as a horizontal line. Grey bars represents the chemical shift perturbation from titration of CXCR2 N-terminal domain to uniformly ^{15}N enriched CXCL5. Data in the grey bars is from previously published results [58].

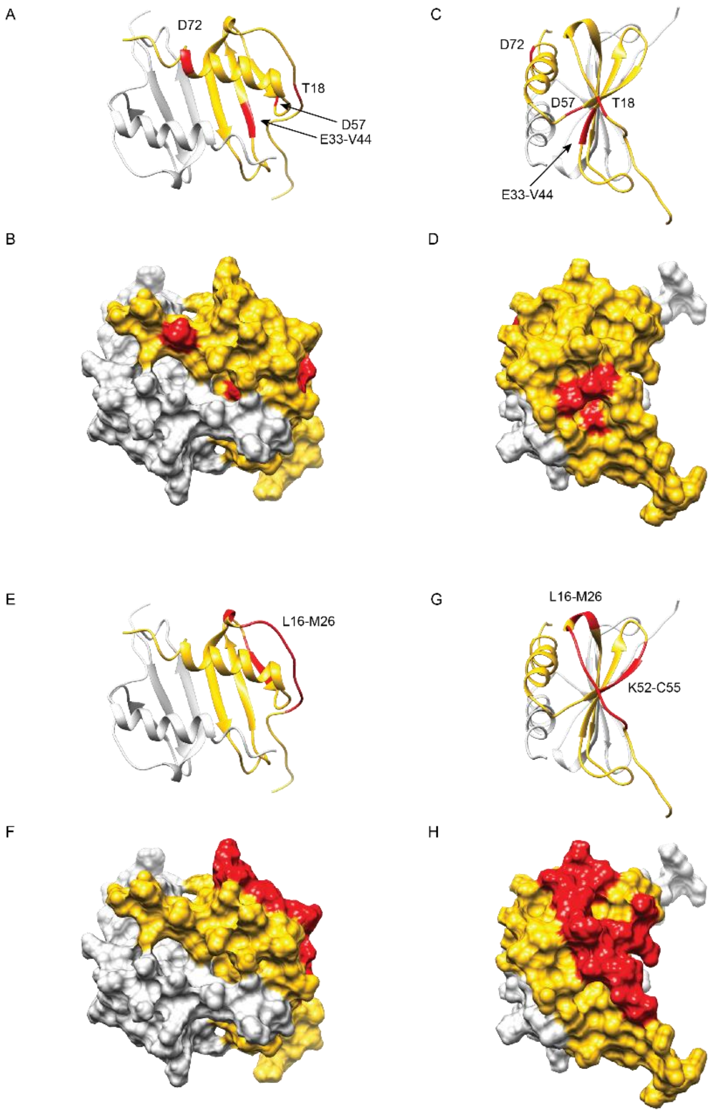

Figure 5.14 Chemical shift perturbation (CSP) mapping onto the dimeric solution NMR structure of CXCL5 (PDB: 2mgs) where highly perturbed residues are shown in red, the rest are shown in gold. The other monomeric molecule of CXCL5 was colored in white to highlight the dimer interface. (A-D) CSP of CXCL5 induced by CXCR1-N-terminal domain binding mapped onto the. (G-L) CSP of CXCL5 induced by CXCR2-N-terminal domain binding using published CSP data [10]. (A, B, E, F) are the front views in ribbon and surface representations with the N-terminal loop and C-terminal helix facing the front. (C, D, G, H) are the horizontally rotated side views in ribbon and surface representations.

5.4 Discussions

Ligand binding of purified CXCR2 was demonstrated using both NMR and ELISA methods. Both IL-8 and CXCL5 binds to CXCR2 in both the DMPC liposome and DMPC MSP1D1ΔH5 nanodiscs, suggesting the purified CXCR2 protein is functional in terms of ligand binding. Both methods, however, cannot provide accurate binding constants for the chemokine and chemokine receptor binding. The immobilization of IL-8 and CXCL5 observed in solution NMR suggest strong binding. However, due to the large size of the liposomes, binding of the chemokines simply reduces the intensity of the small ligands, and thus chemical shift changes of IL-8 or CXCL5 due to binding are inaccessible information. The ELISA experiment provide a direct clue that these interactions exist in the lower nano-molar range, however, due to the lack of curve saturation which require high concentrations of receptors, accurate fitting of the Hill equation could not be achieved.

To study the termini of CXCR2, truncation of the entire N-termini was not resorted to preserve conserved disulfide bonds in the N-terminal domain. In addition, residues close to the disulfide bond was preserve to allow efficient thrombin cleavage during protein purification. Truncation in the C-terminal domain also leave behind residues to allow enough exposure of the added His-tag at the C-terminal region to facilitate protein purification. Previous study on CXCR1 has concluded that 19 residues from the CXCR1 N-terminal domain and 25 residues from the CXCR1 C-terminal domains are mobile. They are assigned to the first 19 residues of the N-terminal domain of CXCR1 and the last 25 residues of CXCR1 [14].

CXCL5 was first cloned into the pET31b vector with a factor Xa cleavage site using previously established protocols [10]. During protein purification, large amounts of the protein was lost due to aggregation after factor Xa cleavage. Due to the relative stability of the CXCL5 protein in high salt buffers, the WelQut enzyme (www.thermofisher.com) was also tried after engineering a cleavage site replacing the factor Xa site. Aggregation remained a problem. A hypothesis was generated after the realization that the original 80 mg/L fusion protein yield almost all resulted in aggregation, that the produced CXCL5 was improperly folded. Given the reducing environment in *E.Coli* the correct formations of the two pairs of disulfide bonds within CXCL5 might be important. With the hypothesis that proper formation of the disulfides in *E.Coli*, might be the major hindrance for obtaining more of the correctly folded protein. The combination of the use of a tightly-controlled weak promoter (ptrc) and the use of the disulfide promoting BL21 Shuffle strain, allowed significant improvement of the final yield of CXCL5. However, the choice of expression system reduces the fusion protein yield significantly to less than 40 mg/L. The choice of thrombin as the cleavage enzyme in the final protocol is a result of the salt stability of the thioredoxin-CXCL5 fusion protein in 250-500 mM NaCl salinity. Overall the purification of CXCL5 is optimized resulted in larger portions of correctly folded protein.

Solution NMR results with the three types of CXCR2 containing nanodiscs samples suggest there are only about 30-35 observable mobile residues of CXCR2 in nanodiscs. This can be due to the size of the nanodisc or other factors such as dynamics. Using DMPC/DHPC q=0.1 bicelle allows the study of CXCR2 termini in the context of the full length protein. Although the bicelle spectra do not overlap with that of the nanodisc samples, they provide information on the relative mobility of the different domains.

Combining the information from the DMPC/DHPC q=0.1 bicelle and nanodisc samples, it can be concluded that the first 12-16 residues in CXCR2 N-terminal domain are relatively mobile, as well as the last 16 residues in the C-terminal domain. At high temperatures and low pH, about 20 additional residues becomes mobile in the C-terminal domain. The immobilized residues in N-terminal domain of CXCR2 remain invisible in solution NMR even at pH 4 and 50°C suggests the N-terminal domain of CXCR2 is structured either through interactions with the other extracellular domains or through the disulfide bond. This has significant implications for future studies because prior studies of the isolated N-terminal domains may not present a full picture of the CXCR2 N-terminal domain participation in ligand interactions. The structured and immobile N-terminal domain of CXCR2 and CXCR1 in the context of the full length receptors were used in chemokine binding studies here.

The results observed in spectra for the ^{15}N edited ^{1}H chemical shift experiments where receptors in proteoliposomes are added to the chemokines suggest CXCL5 and IL-8 (1-66) are binding to and immobilized by CXCR2. This result is also supported by the ELISA experiments where the binding of chemokines to the receptor is detected by antibodies against the histidine tag on only the receptors. In the context of the full length CXCR1 receptor, binding of CXCL5 caused immobilization of the CXCL5 at equimolar ratios. To determine whether the binding of the CXCL5 with CXCR1 involves CXCR1 N-terminal domain. Chemical shift perturbation cause by CXCR1 N-terminal peptide titration to ^{15}N enriched CXCL5 was measured. The CSP data with comparison from literature data [58] suggest the residue N-loop region of CXCL5 residues 17-25, which is perturbed by N-terminal peptide of CXCR2, is not significantly altered by N-terminal peptide of

CXCR1 except for T18. It is possible the lack of specific interactions which may reposition the N-terminal ELR motif containing loop might explained the lack of potency of CXCL5 for CXCR1 since it is well known that the N-loop of the chemokine binding region is responsible for binding the receptor CXCR1 and CXCR2 N-terminal domain [45, 59]. In addition, a second major CSP site for CXCR2 N-terminal peptide to CXCL5 from residue 52-55 which is spatially close to the N-loop site but located on the beta strands was not found in CXCR1 N-terminal peptide binding perturbations. Instead the perturbation for CXCR1 N-terminal domain changes residue 43, 44, and 57 which lays beneath T18, and 72 located in a different part of the CXCL5 protein, however, they all have small amplitudes of perturbations induced by CXCR1 N-terminal peptide binding.

In terms of chemokine binding regions, studies using CXCR1 and CXCR2 N-terminal domain and IL-8 has demonstrated similar binding regions on the chemokine IL-8 [49, 53, 60]. This is similar to the observation of Sepuru *et. al.* (2016) shown for CXCL5, where both the N-terminal domain of the chemokines and residues on the β sheet are significantly perturbed in titration experiments [58], or of CXCL1 binding to CXCR2 N-terminal domain [61] or CXCL7 binding to CXCR2 N-terminal domain [62]. The interaction scheme can even be observed in the CSP induced by binding of high affinity antagonist hG31P mutant of IL-8(3-72) to CXCR1 N-terminal domain where the binding sites on mutant IL-8 is mapped to homologous regions within IL-8 structure but contain extremely small amplitudes [63]. The small amplitudes of CSP measurements for CXCL5 binding to CXCR1 compares to the hG31P case. Interestingly, CSP induced by CXCR2-N terminal domain on CXCL7 also has small amplitudes despite having 10 nM affinity [62]. As a result, small CSP amplitudes alone might not predict ligand bias or affinity in this case.

And it is worth mentioning that all the mentioned research uses the same chemical shift scaling methods. Instead of the magnitude of the CSP, the CSP pattern might be a better predictor of the strength of ligand-receptor interactions.

Combining our data with previous studies, CXCL5 is a weak agonist for CXCR1, and that has affinities for CXCR1 as well as CXCR2. CXCL5 interaction with CXCR1 N-terminal domain was also observed. The fact that previous studies failed to directly capture the weak binding of CXCL5 to CXCR1 indicate that this binding is weak [9, 11], and are not accessible to the assay techniques used [64]. Also when comparing to *in vivo* studies, differences in posttranslational modification can be argued, since CXCR2 protein obtained here is expressed in *E.Coli* and previous studies in HEX cells (human cell line) and COS-7 cells (monkey cell line). Possible differences in CXCL5 posttranslational modifications can be argued as well.

The proteoliposome binding experiments of CXCL5 and CXCR1 demonstrate binding of CXCL5 to full length CXCR1 however, it cannot provide accurate range of K_d. To further characterize and compare the interaction between CXCL5, CXCR1 and CXCR2, solid-state NMR methods [15, 49, 65] as well as other biophysical techniques has to be utilized. The relative affinity however, can be obtained using competition experiments [11]. It is known that chemokine forms heterodimers [66], to eliminate the effect of chemokine self-interactions, IL-8 (1-66) which is known to favor the monomer state was used in the competition experiments. The competition of unlabeled IL-8 (1-66) for ^{15}N enriched CXCL5 showed stronger binding of IL-8 (1-66) for CXCR1. It is evident that at ligand to receptor molar ratio of 2:1, in which include 1:1 molar ratios for both IL-8

(1-66) and CXCL5, show 84% of the signal from CXCL5. Since IL-8 (1-66) was added after CXCL5, this result establishes the stronger affinity of IL-8 for CXCR1. However, additional binding sites between chemokines and the receptors are not accessible in these experiments, future studies will utilize solid-state NMR methods. Furthermore G protein activation studies are also needed to demonstrate that the purified protein is fully functional.

To sum up, here we demonstrate purification of the G protein-coupled receptor CXCR2 and its functional ligand binding. It was also demonstrated that the terminal domains of CXCR2 are structured with only a small fraction of residues visible in solution NMR. Here evidence for chemokine CXCL5 binding to CXCR1 is also demonstrated, the binding site on CXCL5 was mapped with NMR chemical shift perturbation. The presence of ligand bias using NMR spectroscopy in the context of full length receptors is also presented, attributed to the lack of binding sites on CXCL5 N-terminal loop for CXCR1 N-terminal domain.

5.5 Conclusion

Using NMR we demonstrated that the CXCR2 N- and C-terminal domain are structured. With only about 10 residues in the N-terminal domain accessible to solution NMR techniques which measures signals from mobile protein residues. The C-terminal domain of CXCR2 can become more mobile in low pH and at high temperatures. We also demonstrated the functional binding of CXCL5 and IL-8 to CXCR2 using NMR and ELISA, and found less favorable binding of CXCL5 to CXCR1 through both competition experiments and chemical shift perturbation experiments with the CXCR1 N-terminal peptide. The results suggests weaker CXCL5 specificity on the N-loop might explain the function of CXL5 as weak agonist of CXCR2, and overall lack of strong binding sites on CXCL5 might explain why IL-8 has higher affinity and is a favorable ligand for CXCR1, however, due to the possible existence of additional binding sites outside of the CXCR1 N-terminal domain, methods that focus on immobilized residues of the receptors has to be utilized.

5.6 Acknowledgements

We thank Dr. Jasmina Radoicic, for the help with CXCR1, and many helpful suggestions of the optimization of CXCR2. We thank Dr. Sabrina Berkamp for the help with IL-8, helpful suggestions for the purification of CXCL5, and the chemokine- receptor binding experiments. We thank Dr. Sang Ho Park for many helpful suggestions on CXCR2, CXCL5 and NMR experiments. We thank Dr. Bibhuti Das and Dr. Ratan Rai for the help with magic-angle spinning and solid-state NMR experiments. We thank Dr. Anna De Angelis and Dr. Albert Wu for helpful suggestions and help with instrumentation. We thank Professor Roger Sunahara for helpful discussions of GPCR topics. We thank Cheryl Arrowsmith for sharing the pTRC-LIC plasmid.

Chapter 5, in full, is a reprint of the material as it appears Long, Z, Opella SJ, (to be submitted), Studies of Full Length and Truncated Chemokine Receptors Reveal mechanism of Chemokine Signaling Bias for CXCR1 and CXCR2, (2019). The dissertation author is the primary researcher and author on the manuscript.

5.7 References

[1] D.S. Wishart, Y.D. Feunang, A.C. Guo, E.J. Lo, A. Marcu, J.R. Grant, T. Sajed, D. Johnson, C. Li, Z. Sayeeda, N. Assempour, I. Iynkkaran, Y. Liu, A. Maciejewski, N. Gale, A. Wilson, L. Chin, R. Cummings, D. Le, A. Pon, C. Knox, M. Wilson, DrugBank 5.0: a major update to the DrugBank database for 2018, Nucleic Acids Res, 46 (2018) D1074-D1082.

[2] J.W. Griffith, C.L. Sokol, A.D. Luster, Chemokines and chemokine receptors: positioning cells for host defense and immunity, Annu Rev Immunol, 32 (2014) 659-702.

[3] S.H. Park, B.B. Das, F. Casagrande, Y. Tian, H.J. Nothnagel, M. Chu, H. Kiefer, K. Maier, A.A. De Angelis, F.M. Marassi, S.J. Opella, Structure of the chemokine receptor CXCR1 in phospholipid bilayers, Nature, 491 (2012) 779-783.

[4] Y. Cheng, X.L. Ma, Y.Q. Wei, X.W. Wei, Potential roles and targeted therapy of the CXCLs/CXCR2 axis in cancer and inflammatory diseases, Biochim Biophys Acta Rev Cancer, 1871 (2019) 289-312.

[5] B. Petri, M.J. Sanz, Neutrophil chemotaxis, Cell Tissue Res, 371 (2018) 425-436.

[6] M.C. Miller, K.H. Mayo, Chemokines from a Structural Perspective, Int J Mol Sci, 18 (2017).

[7] N. Nagarsheth, M.S. Wicha, W. Zou, Chemokines in the cancer microenvironment and their relevance in cancer immunotherapy, Nat Rev Immunol, 17 (2017) 559-572.

[8] S.J. Allen, S.E. Crown, T.M. Handel, Chemokine: receptor structure, interactions, and antagonism, Annu Rev Immunol, 25 (2007) 787-820.

[9] S.K. Ahuja, P.M. Murphy, The CXC chemokines growth-regulated oncogene (GRO) alpha, GRObeta, GROgamma, neutrophil-activating peptide-2, and epithelial cell-derived neutrophil-activating peptide-78 are potent agonists for the type B, but not the type A, human interleukin-8 receptor, J Biol Chem, 271 (1996) 20545-20550.

[10] K.M. Sepuru, K.M. Poluri, K. Rajarathnam, Solution structure of CXCL5--a novel chemokine and adipokine implicated in inflammation and obesity, PLoS One, 9 (2014) e93228.

[11] C.R. Bozic, N.P. Gerard, C. Gerard, Receptor binding specificity and pulmonary gene expression of the neutrophil-activating peptide ENA-78, Am J Respir Cell Mol Biol, 14 (1996) 302-308.

[12] A. Walz, R. Burgener, B. Car, M. Baggiolini, S.L. Kunkel, R.M. Strieter, Structure and neutrophil-activating properties of a novel inflammatory peptide (ENA-78) with homology to interleukin 8, J Exp Med, 174 (1991) 1355-1362.

[13] L. Rajagopalan, K. Rajarathnam, Structural basis of chemokine receptor function--a model for binding affinity and ligand selectivity, Biosci Rep, 26 (2006) 325-339.

[14] S.H. Park, F. Casagrande, B.B. Das, L. Albrecht, M. Chu, S.J. Opella, Local and global dynamics of the G protein-coupled receptor CXCR1, Biochemistry, 50 (2011) 2371-2380.

[15] S.H. Park, S. Berkamp, J. Radoicic, A.A. De Angelis, S.J. Opella, Interaction of Monomeric Interleukin-8 with CXCR1 Mapped by Proton-Detected Fast MAS Solid-State NMR, Biophys J, 113 (2017) 2695-2705.

[16] S.H. Park, F. Casagrande, L. Cho, L. Albrecht, S.J. Opella, Interactions of interleukin-8 with the human chemokine receptor CXCR1 in phospholipid bilayers by NMR spectroscopy, J Mol Biol, 414 (2011) 194-203.

[17] N.R. Latorraca, A.J. Venkatakrishnan, R.O. Dror, GPCR Dynamics: Structures in Motion, Chem Rev, 117 (2017) 139-155.

[18] A. Manglik, B. Kobilka, The role of protein dynamics in GPCR function: insights from the beta2AR and rhodopsin, Curr Opin Cell Biol, 27 (2014) 136-143.

[19] S. Bockenhauer, A. Furstenberg, X.J. Yao, B.K. Kobilka, W.E. Moerner, Conformational dynamics of single G protein-coupled receptors in solution, J Phys Chem B, 115 (2011) 13328-13338.

[20] W. Liu, E. Chun, A.A. Thompson, P. Chubukov, F. Xu, V. Katritch, G.W. Han, C.B. Roth, L.H. Heitman, I.J. AP, V. Cherezov, R.C. Stevens, Structural basis for allosteric regulation of GPCRs by sodium ions, Science, 337 (2012) 232-236.

[21] G.J. LaRosa, K.M. Thomas, M.E. Kaufmann, R. Mark, M. White, L. Taylor, G. Gray, D. Witt, J. Navarro, Amino terminus of the interleukin-8 receptor is a major determinant of receptor subtype specificity, J Biol Chem, 267 (1992) 25402-25406.

[22] R. Dawaliby, C. Trubbia, C. Delporte, M. Masureel, P. Van Antwerpen, B.K. Kobilka, C. Govaerts, Allosteric regulation of G protein-coupled receptor activity by phospholipids, Nat Chem Biol, 12 (2016) 35-39.

[23] A. Koehl, H.L. Hu, D. Feng, B.F. Sun, Y. Zhang, M.J. Robertson, M. Chu, T.S. Kobilka, T. Laermans, J. Steyaert, J. Tarrasch, S. Dutta, R. Fonseca, W.I. Weis, J.M.

Mathiesen, G. Skiniotis, B.K. Kobilka, Structural insights into the activation of metabotropic glutamate receptors, Nature, 566 (2019) 79-+.

[24] J. Garcia-Nafria, C.G. Tate, Cryo-Electron Microscopy: Moving Beyond X-Ray Crystal Structures for Drug Receptors and Drug Development, Annu Rev Pharmacol Toxicol, (2019).

[25] F. Hagn, M. Etzkorn, T. Raschle, G. Wagner, Optimized phospholipid bilayer nanodiscs facilitate high-resolution structure determination of membrane proteins, J Am Chem Soc, 135 (2013) 1919-1925.

[26] M.L. Nasr, D. Baptista, M. Strauss, Z.J. Sun, S. Grigoriu, S. Huser, A. Pluckthun, F. Hagn, T. Walz, J.M. Hogle, G. Wagner, Covalently circularized nanodiscs for studying membrane proteins and viral entry, Nat Methods, 14 (2017) 49-52.

[27] A.M. Seddon, P. Curnow, P.J. Booth, Membrane proteins, lipids and detergents: not just a soap opera, Biochim Biophys Acta, 1666 (2004) 105-117.

[28] M. le Maire, P. Champeil, J.V. Moller, Interaction of membrane proteins and lipids with solubilizing detergents, Biochim Biophys Acta, 1508 (2000) 86-111.

[29] E. Serebryany, G.A. Zhu, E.C.Y. Yan, Artificial membrane-like environments for in vitro studies of purified G-protein coupled receptors, Bba-Biomembranes, 1818 (2012) 225-233.

[30] J. Li, P.C. Edwards, M. Burghammer, C. Villa, G.F. Schertler, Structure of bovine rhodopsin in a trigonal crystal form, J Mol Biol, 343 (2004) 1409-1438.

[31] R. Dawaliby, C. Trubbia, C. Delporte, M. Masureel, P. Van Antwerpen, B.K. Kobilka, C. Govaerts, Allosteric regulation of G protein-coupled receptor activity by phospholipids, Nat Chem Biol, 12 (2016) 35-+.

[32] D.P. Staus, L.M. Wingler, D. Pichugin, R.S. Prosser, R.J. Lefkowitz, Detergent- and phospholipid-based reconstitution systems have differential effects on constitutive activity of G protein–coupled receptors, Journal of Biological Chemistry, (2019).

[33] M.R. Whorton, M.P. Bokoch, S.G. Rasmussen, B. Huang, R.N. Zare, B. Kobilka, R.K. Sunahara, A monomeric G protein-coupled receptor isolated in a high-density lipoprotein particle efficiently activates its G protein, Proc Natl Acad Sci U S A, 104 (2007) 7682-7687.

[34] I.G. Denisov, S.G. Sligar, Nanodiscs for structural and functional studies of membrane proteins, Nat Struct Mol Biol, 23 (2016) 481-486.

[35] C.R. Sanders, 2nd, J.P. Schwonek, Characterization of magnetically orientable bilayers in mixtures of dihexanoylphosphatidylcholine and dimyristoylphosphatidylcholine by solid-state NMR, Biochemistry, 31 (1992) 8898-8905.

[36] S.H. Park, S.J. Opella, Triton X-100 as the "Short-Chain Lipid" Improves the Magnetic Alignment and Stability of Membrane Proteins in Phosphatidylcholine Bilayers for Oriented-Sample Solid-State NMR Spectroscopy, J Am Chem Soc, 132 (2010) 12552-12553.

[37] M.N. Triba, P.F. Devaux, D.E. Warschawski, Effects of lipid chain length and unsaturation on bicelles stability. A phosphorus NMR study, Biophys J, 91 (2006) 1357-1367.

[38] R.R. Vold, R.S. Prosser, Magnetically oriented phospholipid bilayered micelles for structural studies of polypeptides. Does the ideal bicelle exist?, J Magn Reson Ser B, 113 (1996) 267-271.

[39] K.P. Howard, S.J. Opella, High-resolution solid-state NMR spectra of integral membrane proteins reconstituted into magnetically oriented phospholipid bilayers, J Magn Reson Ser B, 112 (1996) 91-94.

[40] T.J. Knowles, R. Finka, C. Smith, Y.P. Lin, T. Dafforn, M. Overduin, Membrane proteins solubilized intact in lipid containing nanoparticles bounded by styrene maleic acid copolymer, J Am Chem Soc, 131 (2009) 7484-7485.

[41] A.O. Oluwole, B. Danielczak, A. Meister, J.O. Babalola, C. Vargas, S. Keller, Solubilization of Membrane Proteins into Functional Lipid-Bilayer Nanodiscs Using a Diisobutylene/Maleic Acid Copolymer, Angew Chem Int Edit, 56 (2017) 1919-1924.

[42] A.O. Oluwole, J. Klingler, B. Danielczak, J.O. Babalola, C. Vargas, G. Pabst, S. Keller, Formation of Lipid-Bilayer Nanodiscs by Diisobutylene/Maleic Acid (DIBMA) Copolymer, Langmuir, 33 (2017) 14378-14388.

[43] J. Lee, R. Horuk, G.C. Rice, G.L. Bennett, T. Camerato, W.I. Wood, Characterization of two high affinity human interleukin-8 receptors, J Biol Chem, 267 (1992) 16283-16287.

[44] J. Inglese, P. Samama, S. Patel, J. Burbaum, I.L. Stroke, K.C. Appell, Chemokine receptor-ligand interactions measured using time-resolved fluorescence, Biochemistry, 37 (1998) 2372-2377.

[45] L. Wu, N. Ruffing, X. Shi, W. Newman, D. Soler, C.R. Mackay, S. Qin, Discrete steps in binding and signaling of interleukin-8 with its receptor, J Biol Chem, 271 (1996) 31202-31209.

[46] L. Rajagopalan, K. Rajarathnam, Ligand selectivity and affinity of chemokine receptor CXCR1. Role of N-terminal domain, J Biol Chem, 279 (2004) 30000-30008.

[47] A.J. Laarman, G. Mijnheer, J.M. Mootz, W.J.M. van Rooijen, M. Ruyken, C.L. Malone, E.C. Heezius, R. Ward, G. Milligan, J.A.G. van Strijp, C.J.C. de Haas, A.R. Horswill, K.P.M. van Kessel, S.H.M. Rooijakkers, Staphylococcus aureus Staphopain A inhibits CXCR2-dependent neutrophil activation and chemotaxis, Embo J, 31 (2012) 3607-3619.

[48] J. Norgauer, B. Metzner, I. Schraufstatter, Expression and growth-promoting function of the IL-8 receptor beta in human melanoma cells, J Immunol, 156 (1996) 1132-1137.

[49] S.H. Park, F. Casagrande, L. Cho, L. Albrecht, S.J. Opella, Interactions of Interleukin-8 with the Human Chemokine Receptor CXCR1 in Phospholipid Bilayers by NMR Spectroscopy, Journal of Molecular Biology, 414 (2011) 194-203.

[50] S.R. Leong, R.C. Kabakoff, C.A. Hebert, Complete mutagenesis of the extracellular domain of interleukin-8 (IL-8) type A receptor identifies charged residues mediating IL-8 binding and signal transduction, J Biol Chem, 269 (1994) 19343-19348.

[51] S.H. Park, F. Casagrande, M. Chu, K. Maier, H. Kiefer, S.J. Opella, Optimization of purification and refolding of the human chemokine receptor CXCR1 improves the stability of proteoliposomes for structure determination, Biochim Biophys Acta, 1818 (2012) 584-591.

[52] T.H. Bayburt, S.G. Sligar, Self-assembly of single integral membrane proteins into soluble nanoscale phospholipid bilayers, Protein Sci, 12 (2003) 2476-2481.

[53] S. Berkamp, S.H. Park, A.A. De Angelis, F.M. Marassi, S.J. Opella, Structure of monomeric Interleukin-8 and its interactions with the N-terminal Binding Site-I of CXCR1 by solution NMR spectroscopy, J Biomol NMR, 69 (2017) 111-121.

[54] C.V. Grant, Y. Yang, M. Glibowicka, C.H. Wu, S.H. Park, C.M. Deber, S.J. Opella, A Modified Alderman-Grant Coil makes possible an efficient cross-coil probe for high field solid-state NMR of lossy biological samples, J Magn Reson, 201 (2009) 87-92.

[55] F. Delaglio, S. Grzesiek, G.W. Vuister, G. Zhu, J. Pfeifer, A. Bax, NMRPipe: a multidimensional spectral processing system based on UNIX pipes, J Biomol NMR, 6 (1995) 277-293.

[56] W. Lee, M. Tonelli, J.L. Markley, NMRFAM-SPARKY: enhanced software for biomolecular NMR spectroscopy, Bioinformatics, 31 (2015) 1325-1327.

[57] E.F. Pettersen, T.D. Goddard, C.C. Huang, G.S. Couch, D.M. Greenblatt, E.C. Meng, T.E. Ferrin, UCSF Chimera--a visualization system for exploratory research and analysis, J Comput Chem, 25 (2004) 1605-1612.

[58] K.M. Sepuru, B. Nagarajan, U.R. Desai, K. Rajarathnam, Molecular Basis of Chemokine CXCL5-Glycosaminoglycan Interactions, J Biol Chem, 291 (2016) 20539-20550.

[59] K. Rajarathnam, M. Schnoor, R.M. Richardson, S. Rajagopal, How do chemokines navigate neutrophils to the target site: Dissecting the structural mechanisms and signaling pathways, Cell Signal, 54 (2019) 69-80.

[60] N.J. Skelton, C. Quan, D. Reilly, H. Lowman, Structure of a CXC chemokine-receptor fragment in complex with interleukin-8, Structure, 7 (1999) 157-168.

[61] A. Ravindran, K.V. Sawant, J. Sarmiento, J. Navarro, K. Rajarathnam, Chemokine CXCL1 dimer is a potent agonist for the CXCR2 receptor, J Biol Chem, 288 (2013) 12244-12252.

[62] A.J. Brown, K.M. Sepuru, K. Rajarathnam, Structural Basis of Native CXCL7 Monomer Binding to CXCR2 Receptor N-Domain and Glycosaminoglycan Heparin, Int J Mol Sci, 18 (2017).

[63] H.T. Cheng, H.Y. Yu, J.R. Gordon, F. Li, J.W. Cheng, Effects of K11R and G31P Mutations on the Structure and Biological Activities of CXCL8: Solution Structure of Human CXCL8((3-72))K11R/G31P, Molecules, 22 (2017).

[64] E.C. Hulme, M.A. Trevethick, Ligand binding assays at equilibrium: validation and interpretation, Brit J Pharmacol, 161 (2010) 1219-1237.

[65] S. Berkamp, Interaction Studies of the Chemokine Interleukin-8 with the G Protein-Coupled Receptor CXCR1 by Nuclear Magnetic Resonance Spectroscopy, in, 2018.

[66] I.V. Nesmelova, Y. Sham, J. Gao, K.H. Mayo, CXC and CC chemokines form mixed heterodimers: association free energies from molecular dynamics simulations and experimental correlations, J Biol Chem, 283 (2008) 24155-24166.

Chapter 6. Summary

Here the study of integral membrane proteins is pursued using NMR methods. From model system of N-acetyl leucine single crystals to the single transmembrane helix protein pF1 coat protein, to three helix protein MerFTC and MerFTCΔ, on towards the study of a human G protein-coupled receptor CXCR2. The studies presented here include methods developments of NMR sample, instrumentation, and spectroscopy, revealing new perspectives in different areas of NMR.

Using model peptides and model proteins. The use of perdeuteration in oriented sample solid state NMR is explored for the first time. The aim was to improve spectral resolution. This was achieved in specific experiments such as the separated local field experiment and surprisingly perdeuteration also improves the sensitivity of the mismatched Hartmann Hahn experiment. Use of ^{1}H detection to improve experimental sensitivity was also explored for the first time on a protein sample with the oriented sample solid-state NMR technique. Sensitivity enhancement was found to be highly dependent on the sample quality. With the model protein Pf1 major coat protein, two-fold signal to noise ratio enhancement was measured.

Studies of a three transmembrane helix chimera protein were designed to foster understanding of membrane protein behaviors in NMR spectroscopy. Two constructs of the MerFTC and MerFTCΔ were successfully expressed and purified for NMR experiments. Data verified the existence of a third helix within the protein. Further comparative studies will improve understanding of the behaviors of integral membrane protein domains and better design NMR methods to study complex integral membrane proteins.

NMR experiments were used to study the CXCR2 protein, using truncated CXCR2 proteins and selective labeling, the solution NMR spectra of CXCR2 was partially assigned. Data suggest that the N- and C-terminal domains of CXCR2 are largely immobile, except for about 10 residues close to the termini. In addition, raising the temperature and lowering the pH can mobilized residues in the C-terminal domain of CXCR2 but not residues in the N-terminal domain. A chemokine protein CXCL5 was also purified. Using NMR and ELISA, the binding of CXCL5 and IL-8 to CXCR2 was demonstrated. Our data also suggests different affinities of CXCL5 for CXCR1 compared to IL-8 (1-66). Using the isolated N-terminal peptide of CXCR1, weaker binding of CXCL5 to CXCR1 N-terminal domains was demonstrated.

Here developments for NMR methods for the studies of CXCR2 has greatly advanced the field of oriented sample solid-state NMR. Utilizing new tools of deuteration, and ^{1}H detection, as well as methods in sample preparation for membrane proteins and functional purification of CXCR2 and CXCL5 the molecular details of ligand-receptor interactions can be further described using NMR. The work presented will greatly facilitate future research on the structural biology of CXCR2.

APPENDIX. A Making Perdeuterated and Fully Deuterated ^{15}N U N-acetylated Leucine Crystals

Reagents:

Deuterated L-leucine (DNLM-4642 from Cambridge Isotope Laboratories) and (100mg)

Fresh deuterated acetic anhydride (DLM-1162-5 from Cambridge Isotope Laboratories) (0.8-1mL)

Fresh Glacial Acetic Acid (Fisher Chemical A38S) (4-6mL)

HPLC water (Alfa Aesar 7732-18-5) (15-18mL)

Materials:

Round-bottomed flask (10-20mL)

Small magnetic Stir-Bar

10mL flat-bottomed beaker

10mL syringe

0.2µm syringe filter (small)

Long glass test-tubes

Equipments:

Magnetic stir-plate with heater

Bath sonicator

Lyophilizer

Nitrogen stream

Dull ended tweezers

Fume hood

Procedures:

Pre-clean all tubes and beakers and stir-bars with mili-Q water then place into an oven to dry.

1. Weigh 100mg of leucine and carefully transfer it to the round-bottomed flask with a stir-bar.
2. Carefully add in 4mL of fresh glacial acetic acid.
3. Stir with heat until all leucine crystal dissolved (lowest heat possible: a rule of thumb is if you can touch it with your finger then it is not too hot).
4. Add in 800uL of acetic anhydride, put the cap loosely on. And leave it stirring for 2hours.
5. Turn off heat for 30mins-2hours.
6. Use a gentle flow of nitrogen gas to cool down then evaporate the acetic acid. (It should take 1-4hours for the acetic acid to be blown away.
7. Dissolve the crust (should be white, if yellow in color suggests over-heating occurred) in 10 mL of warm HPLC water and heat gently until everything dissolves.
8. Filter the liquid into a long glass tube using a 10mL syringe.
9. Flash freezer in liquid nitrogen and then lyophilize for at least 1day, or if possible 2 days.

10. Re-dissolve in 5-6mL of HPLC water (or 1:1 water:acetone which works better for the deuterated crystals), heat until dissolves.

    10*.In the case of fully deuterated NAL crystal, one would instead dissolve the NAL powder in 5-6mL D_2O and lyophilize for at least 2 times, before dissolving another time in D_2O before step 11.

11. Filter the liquid into a beaker place in a stationary hood, with minimal disturbances possible. After this procedure the beaker should not be moved until the crystal is ready to be harvested with a pair of clean dull ended tweezers. The pH of the redissolved NAL solution is 5.2.
12. For the fully deruterated crystal, it was placed in a dehydration chamber sealed with vacuum grease and filled with drying pellets.

Check the crystal growth at Day2

The preparation should take 2-4 days, the crystal growth should take 4-10 days. The overall process should take at least 1 week.

Figure A1. Crystal growth for 5 days, size ~1.2 mg.

Figure A2. Setup in a hood at step #6 showing the experimental setup.

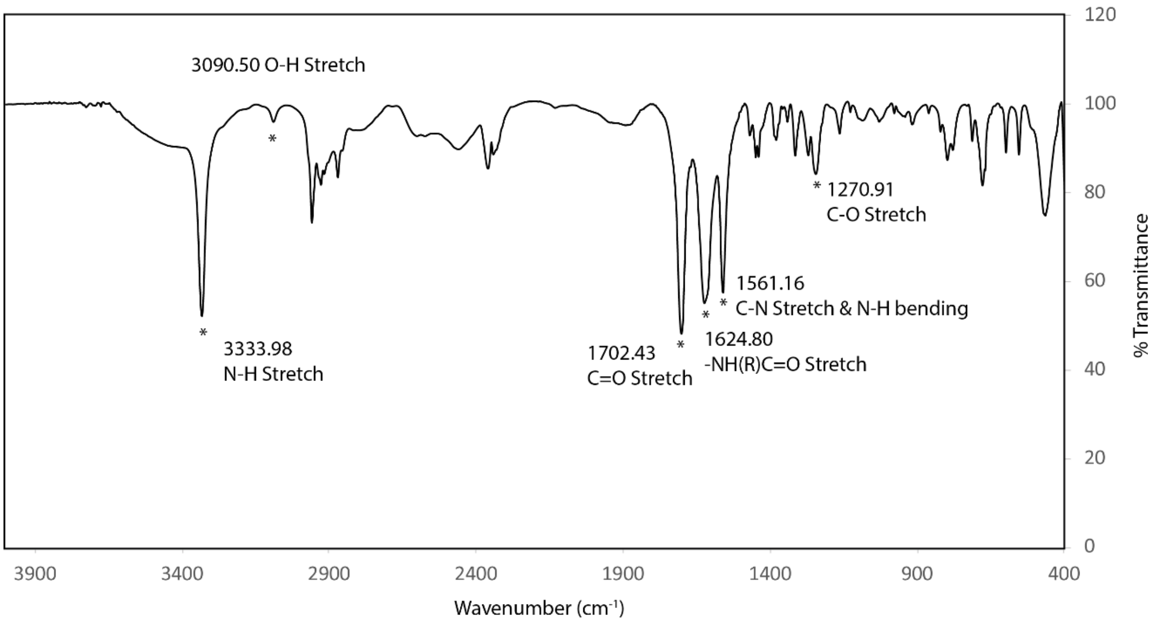

Figure A3. Experimental Infrared (IR) spectrum of N-acetyl-Leucine. The assignments are based on IR-tables. IR spectrum was collected using the dry solid potassium bromide method.

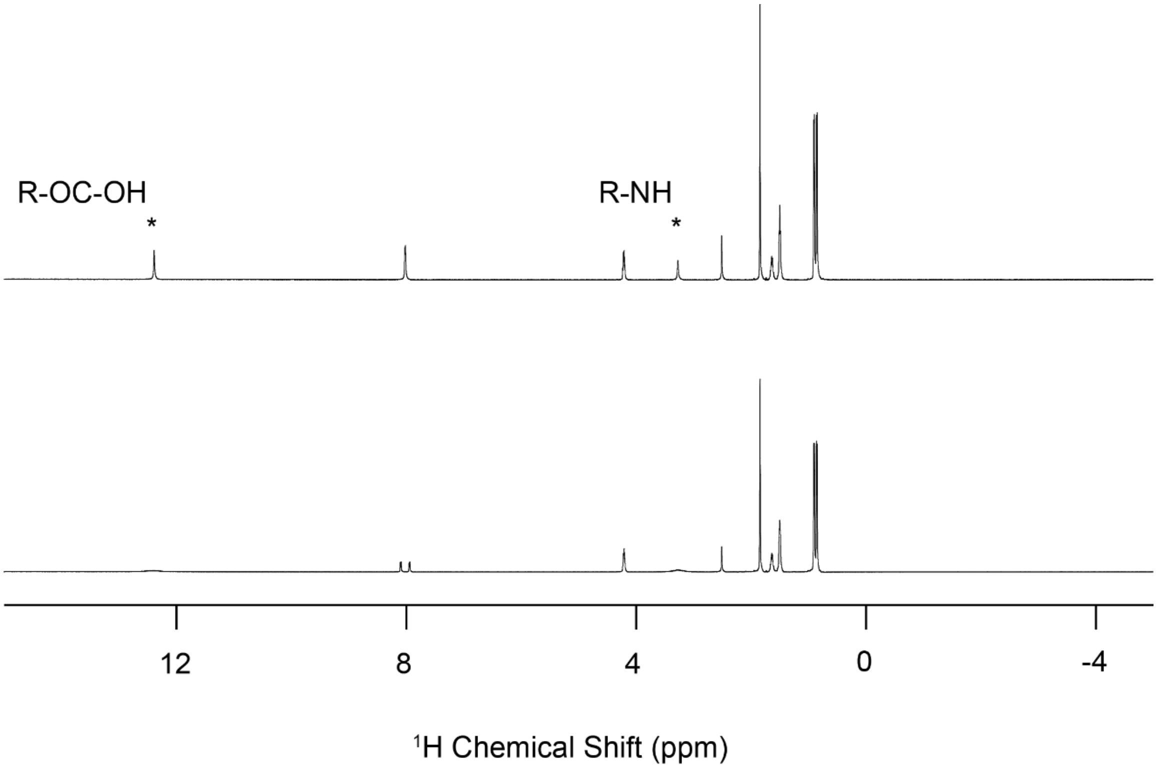

Figure A4. ^{1}H spectra of NAL lyophilized in H_2O (top) or D_2O (bottom) dissolved in DMSO-d6 solvent. The two resonances with the asterisk are assigned to the carboxyl ^{1}H and the amide ^{1}H in the NAL.

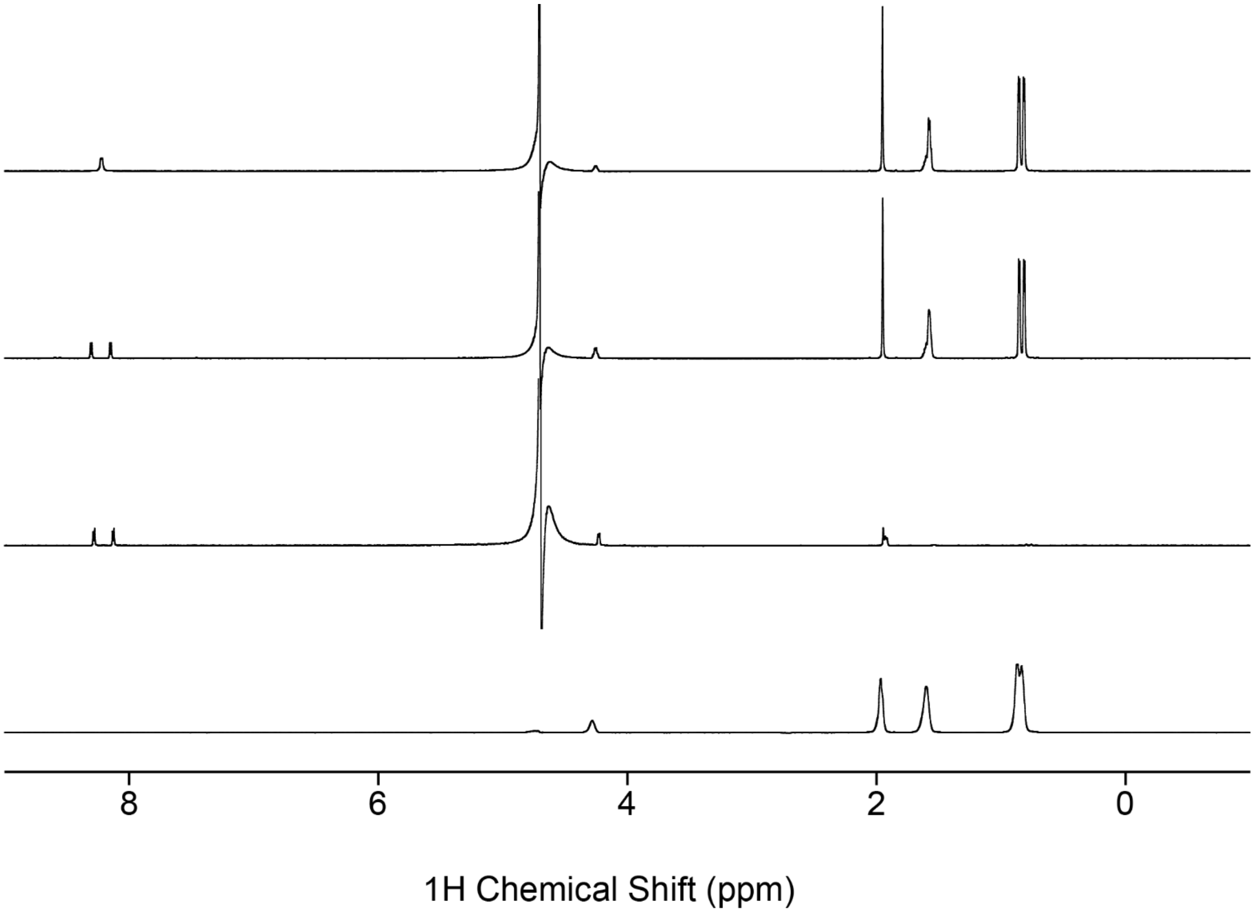

Figure A5. Solvent suppressed ^{1}H spectra of N-acetyl-leucine in solution. Top to bottom: natural abundance NAL, ^{15}N enriched NAL, perdeuteratd-^{15}N enriched NAL with amide ^{1}H in H_2O, ^{15}N enriched NAL in D_2O.

APPENDIX. B Building of Two Probes for NMR Experiments

Two probes were built for the need of NMR experiments, they were built as experimental prototypes. The triple resonance probes have been used for NMR experiments to observe ^{2}H and ^{31}P of deuterated lipids. In Figure B2 and Figure B3, basic ^{31}P parameter optimization was shown for aligned lipid samples using the triple resonance probe.

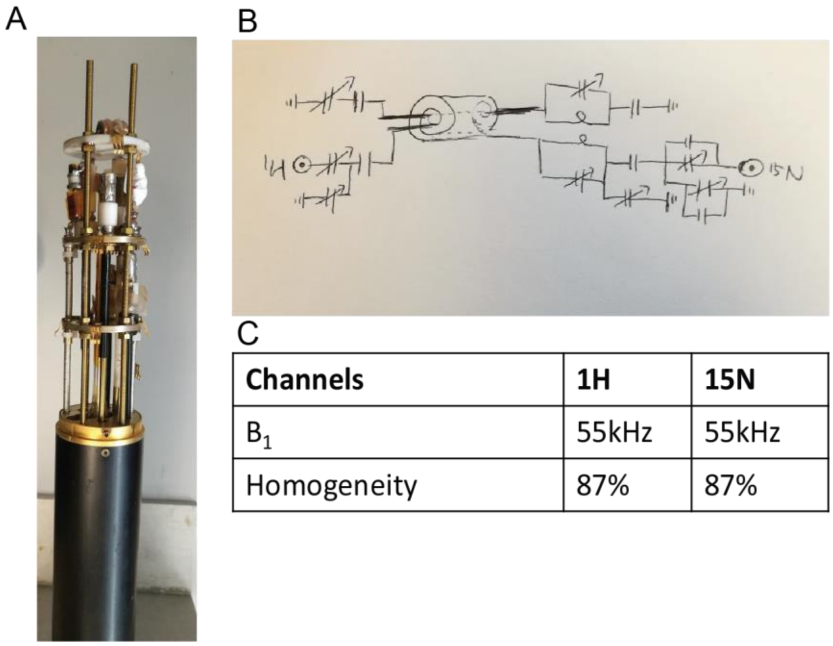

Channels	1H	15N
B_1	55kHz	55kHz
Homogeneity	87%	87%

Figure B1. (A) Picture of the 4-legged scroll coil probe built. The probe contain a 3.8 mm ID coil which is fixated with silicone glue. The four legged probe circuit diagram was shown in (B). (C) lists the maximum B_1 for double resonance experiments achievable with the probe. Also the homogeneity was measured to be 87%. The isolation S_{12} and S_{21} was measured to in between -35dB and -54dB.

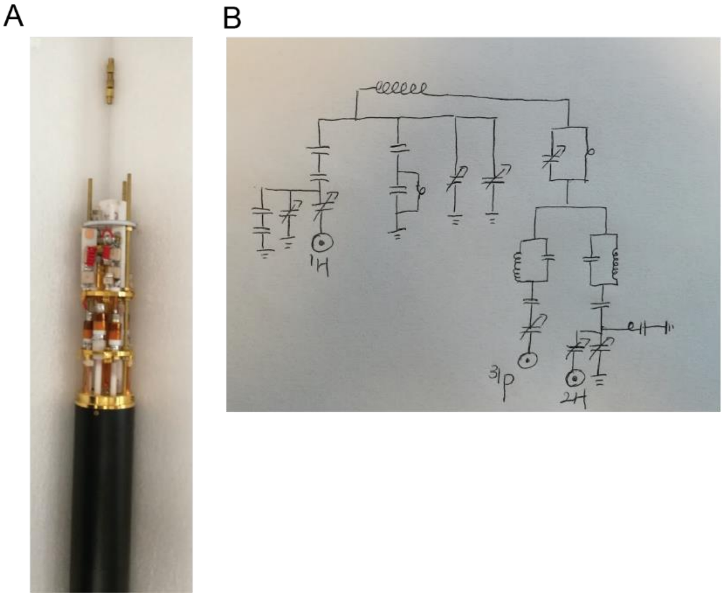

C

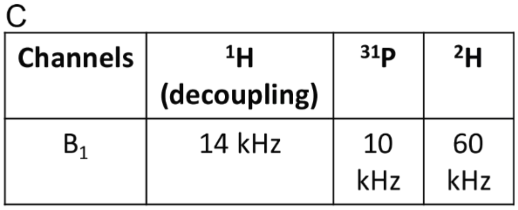

Channels	^1H (decoupling)	^{31}P	^2H
B_1	14 kHz	10 kHz	60 kHz

Figure B2. (A) Picture of the ^1H,^2H,^{31}P Triple Resonance Probe built. The probe contain a 5 mm ID coil which is fixated with a plastic housing. The four legged probe circuit diagram was shown in (B). (C) lists the maximum B_1 for double resonance experiments achievable with the probe for routine experiments. The isolation of the channels are measured as follows: S12: -15dB, S13: -19dB, S21: -28dB, S23: -39dB, S31: -31dB, S32: -29dB.

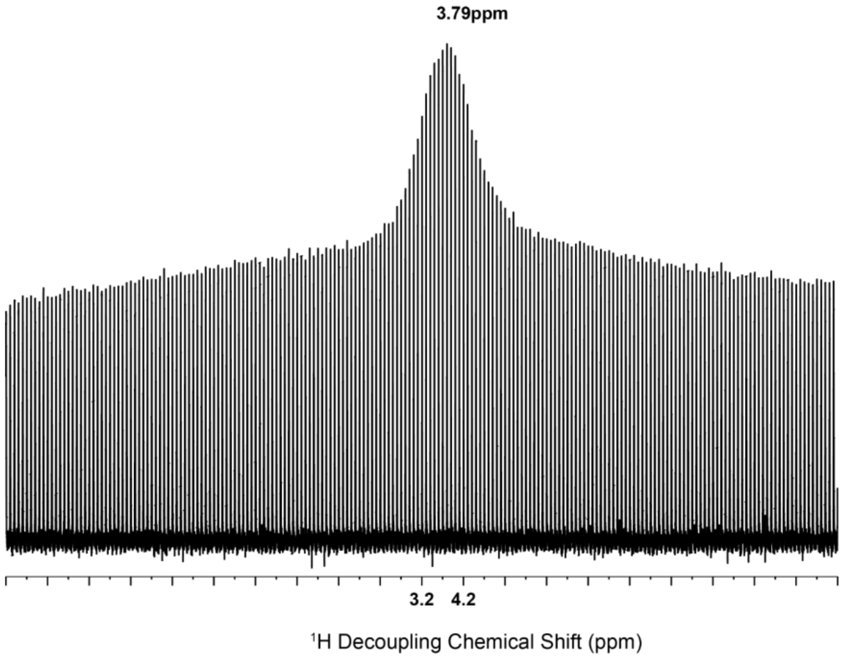

Figure B3. ^1H resonance decoupling frequency search for the aligned DMPC lipid with bilayer normal perpendicular to the external magnetic field B_0 found the frequency to be at 3.79 ppm.

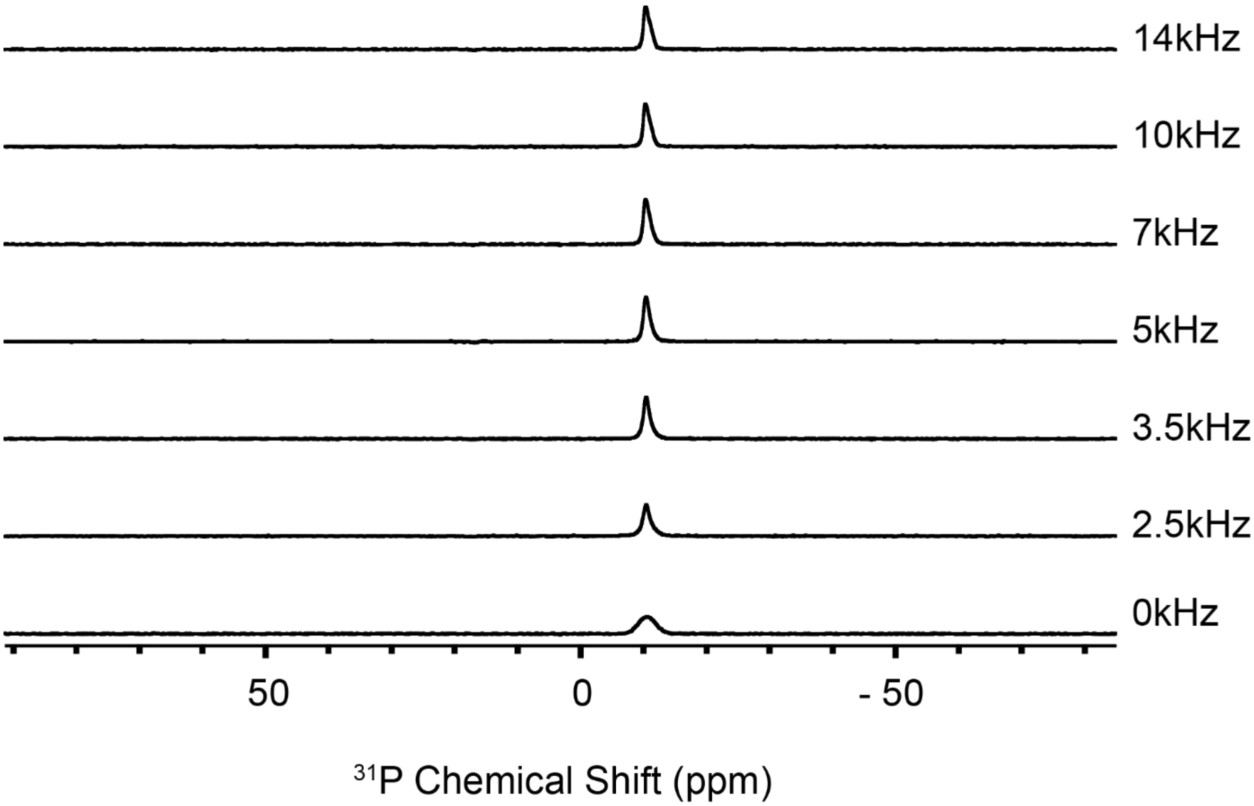

Figure B4. Different decoupling power used for on-resonance ^{1}H decoupling of the ^{31}P signals. These data shows that 3.5-5 kHz radiofrequency power was enough for the decoupling of aligned phospholipid head group ^{31}P resonance.

APPENDIX. C Fluorinated Surfactant as Additives for Styrene Maleic Acid Polymer to Make Aligned Lipid for the Studies of Integral Membrane Proteins

Fluorinated surfactants are known to have mild detergency effects. FOS-C_8F_{13} was previously found to have lyophobic behaviors [1,2] and thus the possibility of using it as an additive in SMALPs macrodisc samples [3] were explored. As can be seen from Figure C1 A that the surfactant alone does not initiate lipid alignments, but from C1 B, it is obvious that lipid alignment of the SMALPs can be induced with smaller amount of styrene maleic acid (SMA) polymer. Also the ^{31}P linewidths of the aligned lipid is as sharp as 0.22 ppm similar to that of the isotropic linewidth.

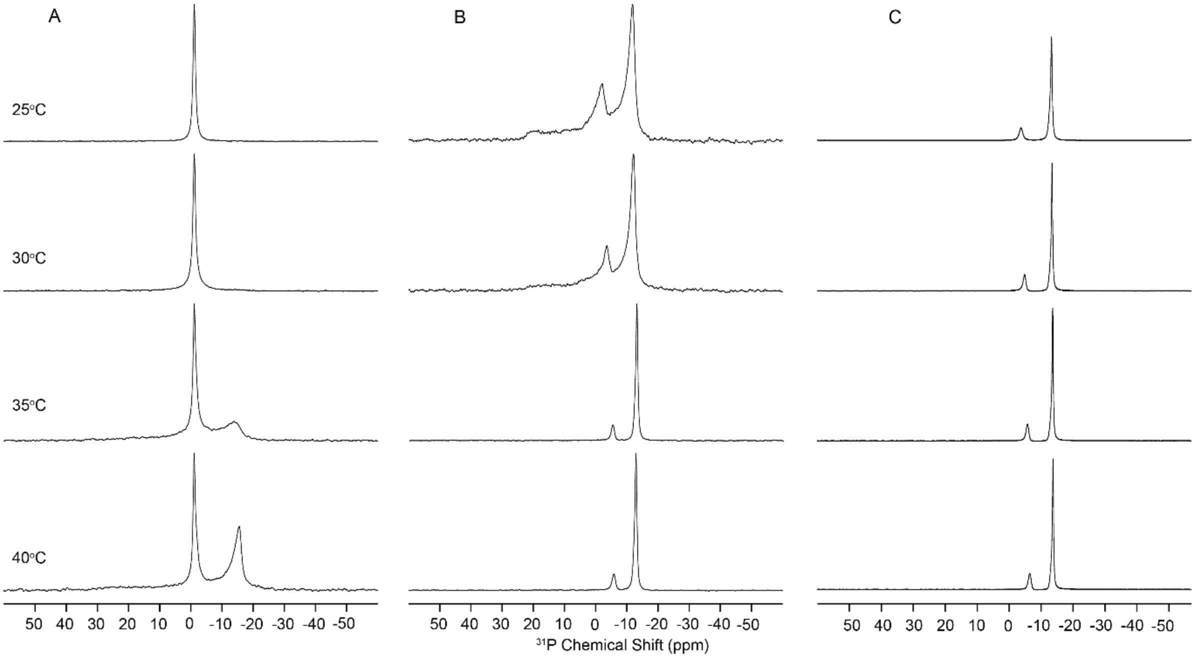

Figure C1. ^{31}P Spectra of aligned lipids observed with NMR spectroscopy. Spectra at various temperatures were collected. (A) Mixture of fluorinated surfactant FOS-C8F13 and DMPC lipids. Sample contain 10% lipid with a DMPC/surfactant ratio of q=3.2. (B) Mixture of fluorinated surfactant FOS-C8F13, SMA 2:1 and DMPC lipids. Sample contain 10% lipid and 0.5% SMA 2:1 with a DMPC/surfactant ratio of q=3.2. (C) Mixture of fluorinated surfactant FOS-C8F13, SMA 2:1 and DMPC lipids. Sample contain 40% lipid and 2% SMA 2:1 with a DMPC/surfactant ratio of q=3.2.

The FOS-C_8F_{13} surfactant / SMA/ DMPC mixture allows more concentrated samples to be made seen in Figure C1 C where as high as 40% lipid concentration was successfully made. MerFt protein is a two transmembrane helix protein which was studied with aligned bicelle using oriented-sample solid-state NMR techniques [4]. Figure C2 shows a SAMPI4 spectrum of MerFt with a close resemblance to the previous results of the protein in DMPC/DHPC bicelles in reference 4 of this appendix.

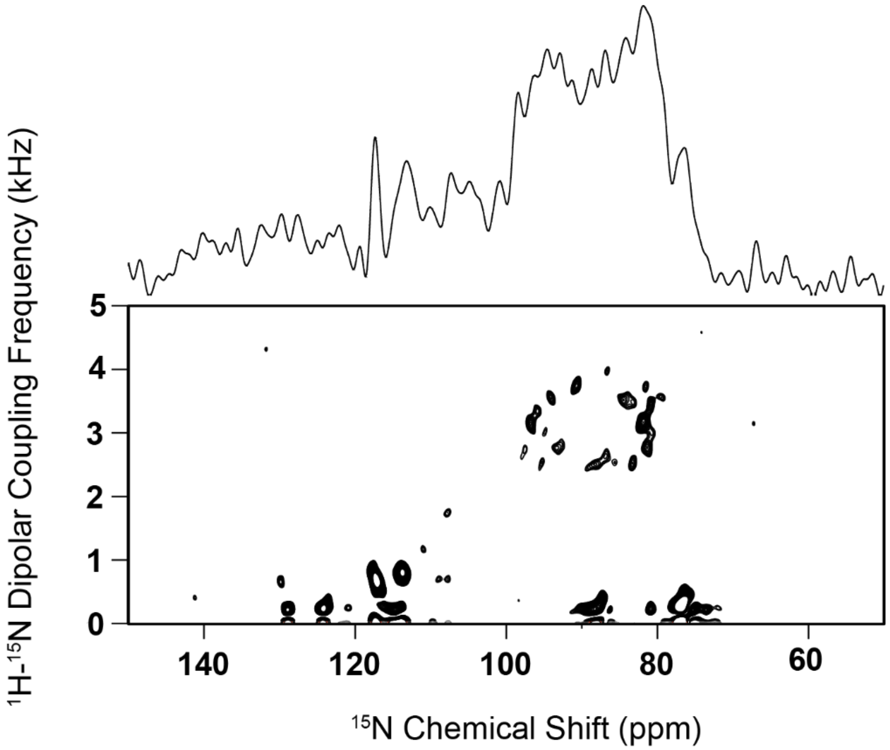

Figure C2. SAMPI4 spectrum of MerFt protein aligned in the magnetic field with the bilayer normal perpendicular to the external magnetic field B_0. The sample contain 40% lipid 2% SMA 2:1 and with a DMPC/ FOS-C_8F_{13} ratio of q=8. The sample contain approximately 1.5 mg of the MerFt protein, and was acquired at 700 MHz ^{1}H frequency using 48 kHz ^{1}H and ^{15}N B_1. The one-dimensional spectrum is shown above the two dimensional SAMPI4 spectrum.

APPENDIX. C Acknowledgements

MerFt protein for NMR sample was kindly provided by Emily (Jiaqian Wu).

APPENDIX. C References

[1] E. Frotscher, B. Danielczak, C. Vargas, A. Meister, G. Durand, S. Keller, A Fluorinated Detergent for Membrane-Protein Applications, Angew Chem Int Edit, 54 (2015) 5069-5073.

[2] C. Vargas, R.C. Arenas, E. Frotscher, S. Keller, Nanoparticle self-assembly in mixtures of phospholipids with styrene/maleic acid copolymers or fluorinated surfactants, Nanoscale, 7 (2015) 20685-20696.

[3] J. Radoicic, S.H. Park, S.J. Opella, Macrodiscs Comprising SMALPs for Oriented Sample Solid-State NMR Spectroscopy of Membrane Proteins, Biophys J, 115 (2018) 22-25.

[4] A.A. De Angelis, S.C. Howell, A.A. Nevzorov, S.J. Opella, Structure determination of a membrane protein with two trans-membrane helices in aligned phospholipid bicelles by solid-state NMR spectroscopy, J Am Chem Soc, 128 (2006) 12256-12267.

APPENDIX. D The Use of the Double Ramp Cross-Polarization and Non-Uniform Sampling Using the ^{1}H-detected PISEMO Experiment

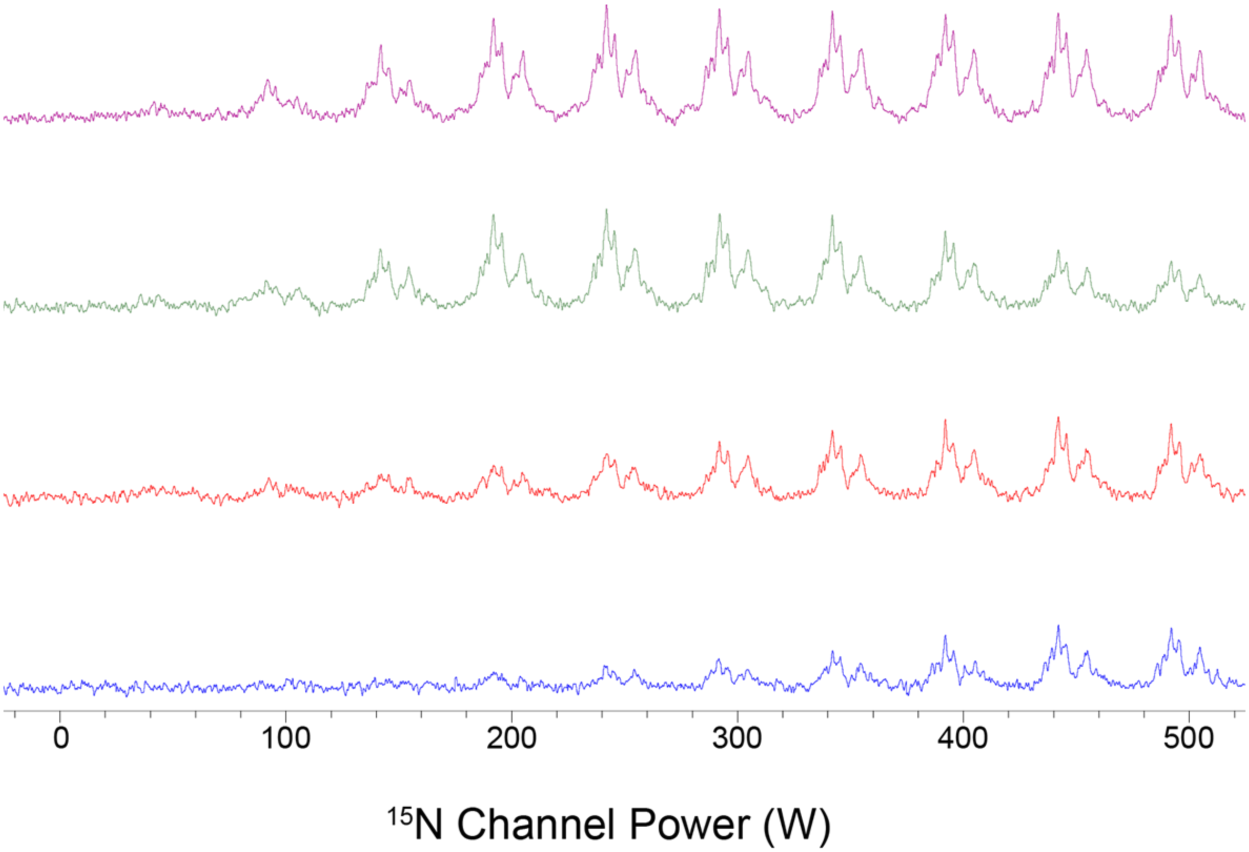

Figure D1. Optimization of the double ramp cross-polarization method. (Top) Double Ramp (100-60% & 60-100%), (second row from top) ^{15}N Ramp (100-60%), (third row from top) MOIST, (Bottom row) CP.

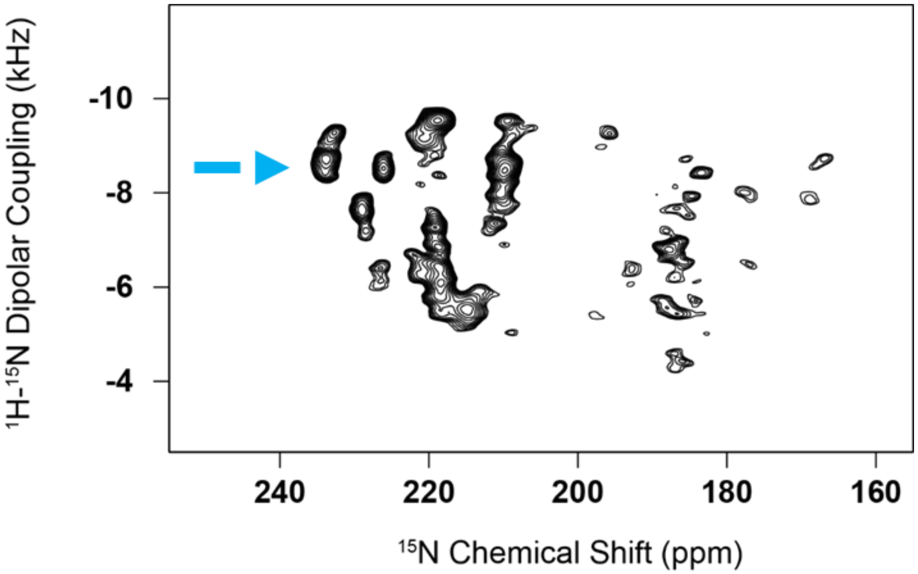

Figure D2. Spectra of the 50% sparse sampled spectrum of the Pf1 phage corresponding to the spectra shown in Figure 3.6B using the ^{1}H detected PISEMO.

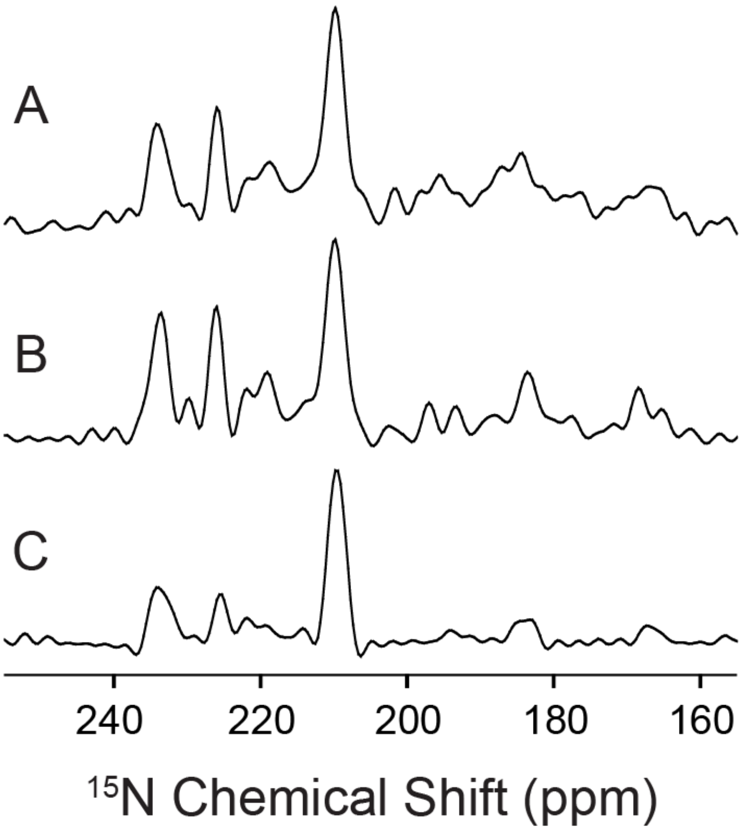

Figure D3. Spectral slice taken at the blue arrow position in Figure D2 for (A) 100% sampling. (B) 50% sampling. (C) 25% sampling.